Deformation studies near hard particles in a Superalloy

Phani Shashanka Karamched

Corpus Christi College

University of Oxford

A thesis submitted for the degree of

Doctor of Philosophy

Trinity Term 2011

Preface

All the work has been carried out by me in the Department of Materials, between October 2007 and July 2011, under the supervision of Dr Angus J Wilkinson and is being submitted for the degree of Doctor of Philosophy at the University of Oxford. No part of this thesis has previously been submitted for a degree at this or any other University. The results presented in this thesis are, to the best of my knowledge, original, except where referenced or acknowledged in this text.

Some of this work has been presented in the following publications and conferences:

Publications:

High resolution electron back-scatter diffraction analysis of thermally and mechanically induced strains near carbide inclusions in a superalloy. *P.S.Karamched and A.J.Wilkinson*. Acta Materialia, (2011), vol. 59, 263-272.

Elastic strain tensor measurement using electron backscatter diffraction in the SEM. *D.J.Dingley, A.J.Wilkinson, G.Meaden and P.S.Karamched*. Journal of Electron Microscopy, (2010), vol. 59, S155-S163.

High-resolution electron backscatter diffraction: an emerging tool for studying local deformation. A.J.*Wilkinson, E.E.Clarke, T.B.Britton, P.Littlewood, and P.S.Karamched,* Journal of Strain Analysis, *(2010)*, vol. 45, 365-376.

Conferences:

Experimental study of local deformation near carbides and grain boundaries in a Superalloy. *P.S.Karamched and A.J.Wilkinson*. talk at RSM EBSD 2010 [Derby, UK].

High resolution EBSD - 3D strain tensors, and geometrically necessary dislocation distributions. *A.J.Wilkinson, P.S.Karamched and T.B.Britton*. talk at 31st Risoe International Symposium on Materials Science Challenges in

materials science and possibilities in 3D and 4D characterisation techniques.(2010)
[Risø National Laboratory for Sustainable Energy, Denmark].

Experimental study of local strains near carbides in a superalloy induced by thermal and mechanical loading. *P.S.Karamched and A.J.Wilkinson*. talk at RSM EBSD 2009
[Swansea, UK].

Experimental Study of local strains near carbides in a superalloy. *P.S.Karamched and A.J.Wilkinson*. talk at fMMT 2009
[Hyderabad, India].

Phani Karamched

Trinity Term, 2011

Acknowledgements

First and foremost I offer my sincerest gratitude to my supervisor, Dr. Angus Wilkinson, who has supported me throughout my thesis with his patience and knowledge, without whom this thesis would not have been completed or written. One simply could not wish for a better or friendlier supervisor.

I would like to thank Prof. Fionn Dunne and his research group at the Department of Engineering Science, for all the help and support with Abaqus simulations and insightful discussions at weekly group meetings. Thanks to all the members of the AJW group, especially Dr. Benjamin Britton who have provided help with Matlab, feedback on this work and all the other friendly assistance.

I would like to thank EPSRC (EP/C509870/1), Rolls Royce and the Department of Materials for financial support, material and experimental facilities. Further thanks to the Electron Microscopy group and the technical support group for training and microscopy support. Thanks to Mr. Laurie Walton and Mr. I R Lloyd for all the help at the workshop and furnaces.

All my family members have provided invaluable support and to them I am very grateful. Finally, special thanks to Madhuri for being very supportive and all my other friends who have made my stay at Oxford very memorable.

Abstract

Title: Deformation studies near hard particles in a Superalloy.

Author: Phani Shashanka Karamched, Corpus Christi College.

Degree: Doctor of Philosophy in Materials.

Term: Trinity Term, 2011.

Superalloys have performed well as blade and disc materials in turbine engines due to their exceptional elevated temperature strength, high resistance to creep, oxidation and corrosion as well as good fracture toughness. This study explores the use of a relatively new technique of strain measurement, high resolution electron backscatter diffraction (HR-EBSD) to measure local deformation fields. The heart of the HR-EBSD technique lies in comparing regions in EBSD patterns from a strained region of a sample to those in a pattern from an unstrained region. This method was applied to study the elastic strain fields and geometrically necessary dislocation density (GND density) distribution near hard carbide particles in a nickel-based superalloy MAR-M-002.

Significant thermal strains were initially induced by thermal treatment, which included a final cooling from the ageing temperature of 870°C. Elastic strains were consistent with a compressive radial strain and tensile hoop strain that was expected as the matrix contracts around the carbide. The mismatch in thermal expansion coefficient of the carbide particles compared to that of the matrix was sufficient to have induced localized plastic deformation in the matrix leading to a GND density of 3×10^{13} m^{-2} in regions around the carbide. These measured elastic strain and GND densities have been used to help develop a crystal plasticity finite element model in another research group and some comparisons under thermal loading have also been examined.

Three-point bending was then used to impose strain levels within the range ±12% across the height of a bend bar sample. GND measurements were then made at both carbide-containing and carbide-free regions at different heights across the bar. The average GND density increases with the magnitude of the imposed strain (both in tension and compression), and is markedly higher near the carbide particles. The higher GND densities near the carbides (order of 10^{14} per m^2) are generated by the large strain gradients produced around the plastically rigid inclusion during monotonic mechanical deformation with some minor contribution from the pre-existing residual deformation from thermal loading. A method was developed of combining the local EBSD measurements with FE modelling to set the average residual strains within the mapped region even when a good strain free reference point was unavailable.

Cyclic loading was then performed under four point loading to impose strain levels of about ±8% across the height of bend bar samples. Similar measurements as in the case of monotonic deformation were made at several interruptions to fatigue loading. Observations from the cyclic loading such as slip features, carbide cracking, GND density accumulation have been explored around carbide particles, at regions away from them and near a grain boundary.

Nomenclature

Acronyms

SEM	Scanning Electron Microscope/Microscopy
EBSD	Electron Backscatter Diffraction
fcc	Face-Centered Cubic
bcc	Body-Centered Cubic
css	Cyclic Stress-Strain
S	Stress
N	No. of cycles of fatigue loading
LCF	Low Cycle Fatigue
HCF	High Cycle Fatigue
GNDs	Geometrically Necessary Dislocations
SSDs	Statistically Stored Dislocations
FE	Finite Element
FEA	Finite Element Analysis
PC	Pattern Center
CBED	Convergent Beam Electron Diffraction
TEM	Transmission Electron Microscope/Microscopy
EBSP	Electron Backscatter Pattern
ROI	Region Of Interest
IPF	Inverse Pole Figure
FEG	Field Emission Gun
EDM	Electric Discharge Machining
CCD	Charge Couple Device
HR-EBSD	High Resolution EBSD (i.e for strains and rotations)
MAE	Mean Angular Error
PH	Peak Height (of the cross-correlation function)
C3D20R	3-dimentional quadratic, 20 reduced-integration elements

Experimental Measures, Conditions and symbols

γ	Gamma phase
γ`	Gamma prime precipitate
wt%	Percentage by weight
θ_B	Bragg angle
λ	Wavelength
d	Interplanar lattice spacing
σ	Stress
ε	Strain
$\Delta\varepsilon_e$	Elastic strain range
$\Delta\varepsilon_p$	Plastic strain range
$\Delta\varepsilon$	Total strain range
N_f	No. of cycles of fatigue failure
σ_a	True stress amplitude
σ_f'	Fatigue strength coefficient
E	Young's modulus
ε_f'	Ductility coefficient in fatigue
σ_m	Mean stress
σ_{UTS}	Monotonic ultimate tensile strength
σ_y	Monotonic yield stress
F	Total deformation gradient
F^e	Elastic deformation gradient
F^P	Plastic deformation gradient
$\dot{F}$	Rate of deformation gradient
L	Velocity gradient
D	Deformation rate
W	Continuum spin tensor
L^P	Plastic velocity gradient
k	Total number of active slip systems
$\dot{\gamma}^\alpha$	Shear rate on the α^{th} slip system

G	Shear modulus
$\overset{\triangledown}{\sigma}$	Jaumann stress state
$\dot{\sigma}$	Material rate of stress
ρ_g, ρ_{GND}	Density of Geometrically necessary dislocations
b	Burgers vector
s	Slip direction
x^s, y^s, z^s	Sample Coordinate axes
x^{screen}, y^{screen}	Coordinate axes on the phosphor screen
Z_{SSD}	Distance from the specimen to the phosphor screen
X_{PC} , Y_{PC}	Screen coordinated of the pattern center
r_i	Three-dimensional vector of a point on the phosphor screen
x_i^* , y_i^*	Coordinates of a point on the phosphor screen
A, β	Displacement gradient tensor
r_i^s	Three-dimensional vector of a point on the phosphor screen in the sample coordinate system
r_i^c	Three-dimensional vector of a point on the phosphor screen in the crystallographic coordinate system
g	Orientation matrix
r, r'	An arbitrary direction within an undeformed (reference) and deformed (test) crystal respectively
Q	Pattern shift, measured in pixels in the phosphor
q	The projection of Q in the direction r
I	Identity matrix
e_{ij} , ε_{ij}	If *i*=*j* then elastic normal strain, if *i*≠*j* then elastic shear strain
w_{ij}	Lattice rotations
u_i	Displacement within a crystal in the i^{th} direction
x_i	Direction within a crystal, in the i^{th} direction (*i*=1 is the ‘x’ direction, *i*=2 is the ‘y’ direction and *i*=3 is the ‘z’ direction)
σ_{ij}	If *i*=*j* then normal stresses, if *i*≠*j* then shear stress
$\emptyset_1, \emptyset, \emptyset_2$	Euler angles in Bunge notation
C_{ijkl}	Single crystal elastic stiffness components in the sample reference frame
α	Nye’s dislocation tensor

b^s	Burgers vector of the s^{th} dislocation type
t^s	Unit line direction of the s^{th} dislocation type
υ	Poisson's ratio
F^t and $F^{t+\Delta t}$	Deformation gradients at the beginning and end of a time increment(t)
s^α	α^{th} slip direction
n^α	Slip plane normal corresponding to the α^{th} slip direction
$\dot{\gamma}^\alpha$	Slip rate corresponding to the α^{th} slip direction
ρ_{SSD}^{m}	mobile statistically stored dislocations
ΔF	Helmholtz free energy barrier
k	Boltzmann constant
T	Absolute temperature
τ^α	Resolved shear stress on the α^{th} slip plane
τ_c	Critical resolved shear stress (CRSS)
ρ_{SSD}^{im}	Density of immobile SSDs
$\Delta\alpha$	difference in the thermal expansion coefficients
n	A lattice plane's normal vector

Table of Contents

1. Introduction

Superalloys are high-temperature materials, which display excellent resistance to mechanical and chemical degradation not only at room temperatures but also at service temperatures close to their melting points (often in excess of 0.7 of the melting temperature). Since they first emerged in the 1950s, these alloys have had a unique impact on the aerospace and power-generation industries. The superalloys are employed in the very hottest section of the turbines, under the heaviest of the loads, with the utmost importance placed on assuring the integrity of the components fabricated from them.

With Nickel as a solvent, but containing in excess of ten different alloying elements, Nickel-based superalloys have emerged as the materials of choice for high-temperature operation when resistance to creep, fatigue and environmental degradation is required [1], [2]. The use of Nickel as a solvent for so many elements is well justified on account of its *fcc* crystal structure, due to the considerable amount of cohesive energy arising from the bonding provided by the outer *d* electrons – a characteristic of transition metals [1].

Furthermore, Nickel is stable in the *fcc* form from room temperature to its melting point (which is high – 1728 K), so that there are no phase transformations to cause expansions and contractions, which might complicate its use for high-temperature components. Other metals in the transition metal series, which display this crystal structure, are denser and/or more expensive than Nickel. Also, diffusion rates for Nickel are low; hence, a considerable amount of microstructural stability is imparted at elevated temperatures. [3].

The microstructure of a typical Nickel based superalloy consists of different phases, drawn from the following list [4]:

The gamma phase, denoted γ. This exhibits the *fcc* structure, and in nearly all cases it forms a continuous, matrix phase in which the other phases reside. It contains significant concentrations of elements such as Cobalt, Chromium, Molybdenum, Ruthenium and Rhenium, where these are present in the alloy.

The gamma prime precipitate, denoted γ`. This forms as a precipitate phase, which is often coherent with the γ-matrix, rich in elements such as Aluminium, Titanium and Tantalum. This phase is chemically *ordered* and is based on the *fcc* or *bcc* crystal structures. In Nickel-Iron superalloys and those rich in Niobium, a related ordered phase, γ``, is preferred instead of γ`.

Carbides. Carbon, often present in concentrations up to 0.2wt%, combines with reactive elements such as Titanium, Tantalum, Tungsten, Chromium, and Molybdenum to form carbides. During heat treatment and service, these carbides begin to decompose and form lower carbides such as MC, $M_{23}C_6$ and M_6C, which tend to form on the grain boundaries. These common carbides all have an *fcc* crystal structure.

Other phases can be found in certain superalloys, particularly in the service-aged condition, for example, the topologically close-packed (TCP) phases μ, σ, Laves, etc.

However, the compositions of the superalloys are chosen to avoid, rather than to promote the formation of these compounds, as they degrade alloy performance.

Superalloys develop high temperature strength through *solid solution strengthening* and by the formation of secondary phase precipitates such as gamma prime and carbides through *precipitation strengthening*. Oxidation and corrosion resistance is provided by the formation of a protective oxide layer, which is formed when the metal is exposed to oxygen and encapsulates the material, and thus protecting the rest of the component.

The failure of components fabricated from the superalloys is a rare occurrence, since the applications demand very conservative designs and significant safety factors. Nevertheless, failures have occurred and undoubtedly there will be further ones in the future. Such failures in crucial aircraft engine components often result in loss of human life. It is thus essential to study crucial superalloy material properties like fatigue life, creep resistance, phase stability, as well as oxidation and corrosion resistance.

This project aims to investigate the development of internal strains, stresses and dislocation densities in a Nickel based superalloy MAR-M-002, in an attempt to better understand the way Nickel superalloys behave. These investigations on the alloy have been made under thermal and mechanical loading (both monotonic and cyclic fatigue). Electron backscatter diffraction (or simply, EBSD) has been used to experimentally determine the local strains and dislocation densities. The technique developed by

Wilkinson et al [5], [6]enables information to be determined about the variation in elastic strains and rotations within a grain, relative to a reference point within the same grain. If the elastic strains are small, the rotation of the lattice can be attributed to geometrically necessary dislocations (GNDs), and the GND density can be calculated using Nye's dislocation tensor analysis [7].

Finally, these experimental measurements have also been used to validate a finite-element polycrystal plasticity modelling approach, currently being developed by Prof. Fionn Dunne's group in the Department of Engineering Science, Oxford University[8].We hope that these direct comparisons between the experiments and simulations of the same grain morphologies and orientations in particular and investigating the development of local strains and dislocation densities, will help in understanding the fundamental reasons of strain accumulation and crack initiation and also allow the development of the finite element polycrystal plasticity model. The development of such models will hopefully reduce the expensive and time-consuming laboratory trials and test methods.

2. Literature Review

2.1. Fatigue

Fatigue is a form of failure that results in the weakening of materials due to dynamic and fluctuating levels of stress. Failure results from the nucleation and growth of fatigue cracks (that form due to this cyclic variation of stress and strain), which eventually can result in sudden fracture. Such failures generally take place under the influence of cyclic loads whose peak values are considerably smaller than the 'safe' loads estimated on the basis of static fracture analysis.

Fatigue failures occur in many different forms. Mere fluctuations in externally applied stresses or strains result in *mechanical fatigue*. Cyclic loads acting in association with high temperatures cause *creep fatigue*; when the temperature of the cyclically loaded component also fluctuates, *thermomechanical fatigue* (i.e. a combination of thermal and mechanical fatigue) is induced. Recurring loads imposed in the presence of a chemically aggressive or embrittling environment give rise to *corrosion fatigue*. The repeated application of loads in conjunction with rolling contact between materials produces *rolling contact fatigue*, while *fretting fatigue* occurs as a result of pulsating stresses along with oscillatory relative motion and frictional sliding between surfaces. The majority of failures in machinery and structural components can be attributed to one of the above fatigue processes [9].

There are several different stages of fatigue damage in an engineering component where defects may nucleate in an initially undamaged section and propagate in a stable manner until catastrophic failure ensues. The progression of fatigue damage can be broadly classified into the following stages [10]:

1. Substructural and microstructural changes which cause nucleation of permanent damage.
2. The creation of microscopic cracks.
3. The growth and coalescence of microscopic flaws to form `dominant' cracks, which may eventually lead to catastrophic failure. (From a practical standpoint, this stage of fatigue generally constitutes the demarcation between crack initiation and propagation)
4. Stable propagation of the dominant macrocrack.
5. Structural instability or complete fracture.

The total fatigue life of a component is defined as the sum of the number of cycles to initiate a fatigue crack and the number of cycles to propagate it subcritically to some final crack size [9]. The conditions for the nucleation of microdefects and the rate of advance of the dominant fatigue crack are strongly influenced by a wide range of mechanical, microstructural and environmental factors.

The uniaxial deformation of engineering alloys subjected to cyclic loads is usually characterised by cyclic stress-strain (css) curve. The transient phenomena typically associated with cyclic deformation are schematically illustrated in Figure 1.

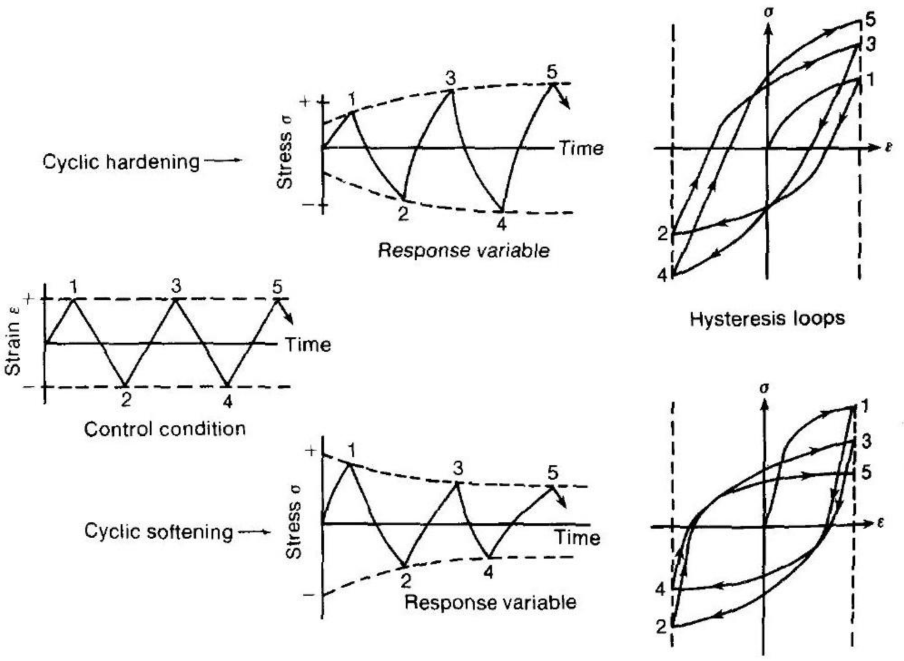

Figure 1. Phenomena associated with transient effects in Fatigue [10]**.**

In the initial few cycles, certain materials show a rapid increase in flow stress (*cyclic hardening*) with increasing number of cycles. This is essentially due to dislocation multiplication occurring within the crystal. Work-hardened materials undergo strain softening (or *cyclic softening*) in the initial stages of cyclic loading. The rearrangement of prestrain-induced dislocation networks due to fatigue is believed to cause cyclic softening [10]. In alloys containing small coherent precipitates, repeated shearing loads often result in local softening around the precipitate. With continued cyclic straining, the rate of hardening/softening progressively diminishes and a quasi-steady state of deformation, known as ‘saturation’, is reached. During the initial fatigue ‘shakedown’, there is a continual change in dislocation substructure until a stable configuration representative of the saturated state is reached. Once saturation occurs, further cycling does not alter the variation of the resolved shear stress with the resolved shear strain and the stress-strain hysteresis loop develops a stable configuration. Beyond this point, the hysteresis loop remains essentially the same cycle after cycle over the life of the test specimen [10].The parameters used to describe the salient features of cyclic hysteresis loops are defined in Figure 2(a). The locus of the tips of the stable hysteresis loops provides the cyclic stress-strain curve, Figure 2(b).

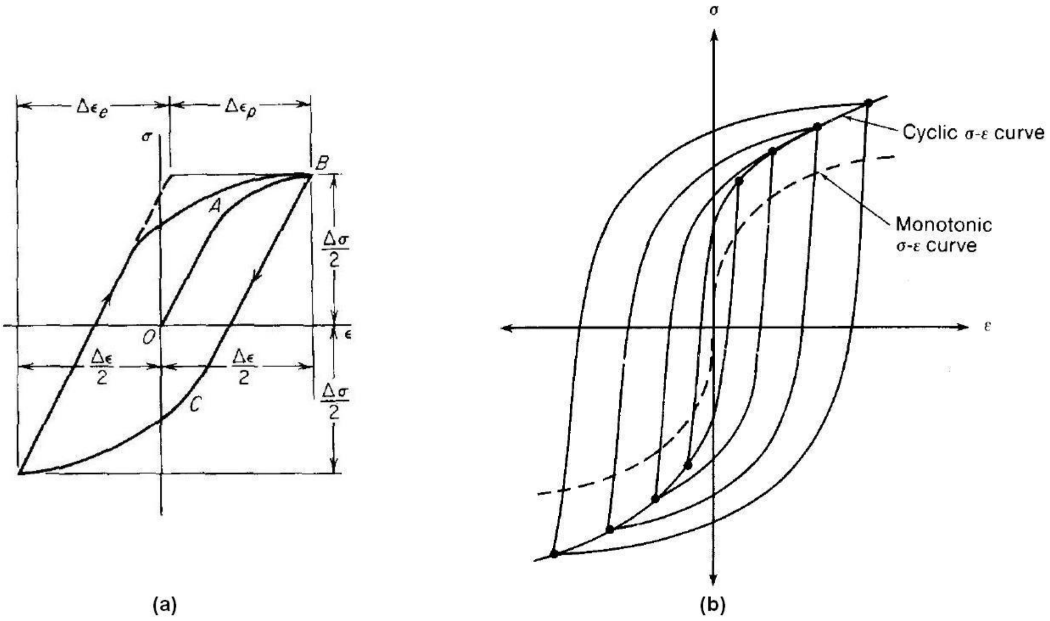

Figure 2. (a)A schematic representation of a stable hysteresis loop and the associated nomenclature. $\Delta\varepsilon_e$, $\Delta\varepsilon_p$, $\Delta\varepsilon$ denote the elastic, plastic and total strain range respectively. (b) Comparison of monotonic and cyclic stress-strain curves for a material that cyclic hardens. Points on the cyclic stress-strain curve represent tips of stable hysteresis loops [10]**.**

A time-honoured approach of treating the cyclic fatigue data has been the stress-life approach. It is largely useful when the stress and strains are mostly elastic. The main drawback of this approach has been the inability to distinguish between the initiation and propagation phases of fatigue life. More recent approaches include the strain-life approach, useful when there is a significant amount of plastic strain. The fatigue life is typically quite short under these conditions.

As already stated, the traditional way of representing fatigue life has been in the form of S-N curves (Figure 3).

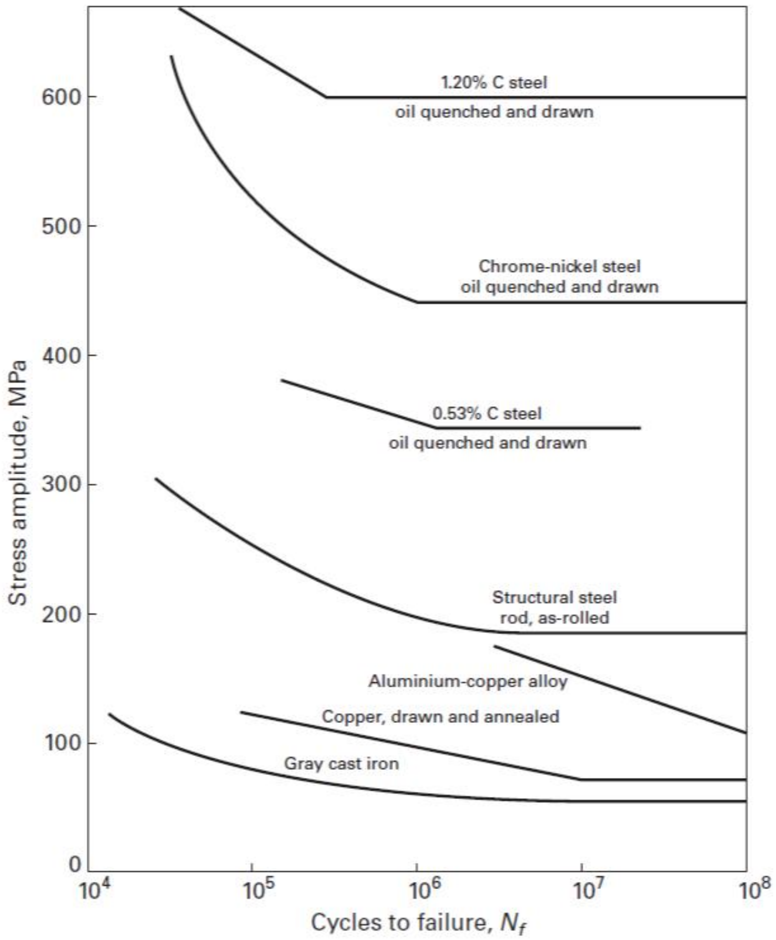

Figure 3. S-N curves for typical metals [11]**.**

With regard to this measure, *fatigue strength* refers to the capacity of the material to resist conditions of cyclic loading. However, in the presence of measurable plastic deformation, materials respond differently to strain cycling than to stress cycling. The elastic component can be readily described by means of a relation between the stress amplitude and the number of reversals to failure (i.e. twice the number of cycles), by Basquin's relation [12], expressed as:

$$\sigma_a = \sigma_f'(2N_f)^b \tag{1}$$

Since the deformation is elastic, we can write:

$$\sigma_a = \frac{\Delta\sigma}{2} = \frac{\Delta\varepsilon_e E}{2} \tag{2}$$

Thus:

$$\frac{\Delta\varepsilon_e}{2} = \frac{\sigma_a}{E} = \frac{\sigma_f'}{E}(2N_f)^b \tag{3}$$

where $\Delta\varepsilon_e/2$ is the elastic strain amplitude, σ_a is the true stress amplitude, σ_f' is the fatigue strength coefficient (equal to the stress intercept at $2N_f$=1), N_f is the number of cycles to failure, and b is the fatigue strength exponent. This relationship is an empirical representation of the S-N curve about the fatigue limit (fatigue limit is the end of the sloping portion of a curve). On a log-log plot, it gives a straight line of slope b. Thus it can be seen in elastic deformation that σ_a/E is equal to the elastic strain amplitude $\Delta\varepsilon_e/2$.

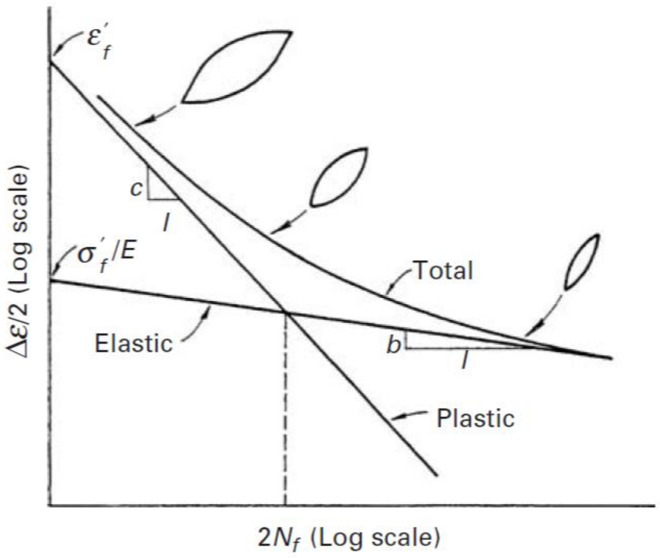

Figure 4. Superposition of elastic and plastic curves gives the fatigue life in terms of total strain [11]**.**

The plastic strain component is better described by the Manson-Coffin relationship [13],

$$\frac{\Delta\varepsilon_p}{2} = \varepsilon'_f\left(2N_f\right)^c \tag{4}$$

where $\Delta\varepsilon_p/2$ is the plastic strain amplitude, ε'_f is the ductility coefficient in fatigue (equal to the strain intercept at $2N_f$=1), N_f is the number of cycles to failure, and c is the fatigue strength exponent. It has been observed that a smaller value of c results in a longer fatigue life. In the regime of high-strain, log-cycle fatigue, the Manson-Coffin relation assumes great importance. Experimentally, it is frequently more convenient to control the total strain. For a material subjected to a total strain range of $\Delta\varepsilon_t$ (elastic and plastic strain), we can determine the fatigue strength by a superposition of the elastic and plastic components, i.e.,

$$\frac{\Delta\varepsilon_t}{2} = \frac{\Delta\varepsilon_e}{2} + \frac{\Delta\varepsilon_p}{2} = \frac{\sigma_f'}{E}\left(2N_f\right)^b + \varepsilon_f'\left(2N_f\right)^c \qquad (5)$$

Thus we expect that the curve of fatigue life, in terms of total strain, will tend to the plastic curve at large total-strain amplitudes, whereas it will tend to the elastic curve at low total-strain amplitudes, as shown schematically in Figure 4. The Manson-Coffin regime is knows as *low-cycle fatigue*, in which there is a discrete amount of plastic deformation in each cycle. The Basquin regime is called the *high-cycle fatigue*. The stresses are primarily elastic in this domain. The typical range of values for the exponents b(high-cycle fatigue) and c (low-cycle fatigue) are:

$$b \,:\, 0.125 \,\rightarrow 0.2\ (Basquin\ exponent)$$

$$c \,:\, 0.5 \,\rightarrow 0.6\ (Manson - Coffin\ exponent)$$

The mean stress σ_m can have an important effect on the fatigue strength of a material. A simple way to demonstrate the effect of σ_m would be to present S-N curves of a given material for different values of $\sigma_m$on the same graph. Figure 5 shows such curves schematically. For a given stress amplitude σ_a, as the mean stress increases, the fatigue life decreases.

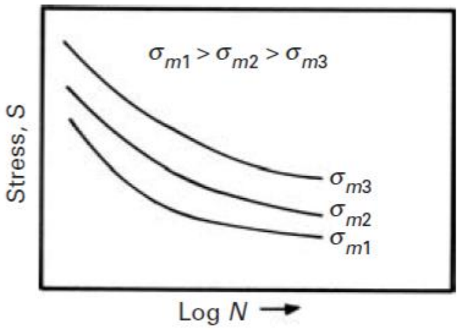

Figure 5. Effect of mean stress on S-N curves. The fatigue life decreases as the mean stress increases [11]**.**

In the real-life behaviour of a material, the damage produced in each cycle by cycle plastic strain is dependent and cumulative. Several empirical expressions have been proposed which take into account the effect of mean stress on fatigue life. These are mostly written so as to give combinations of stress amplitude and mean stress that give the same fatigue life as cyclic loading at zero mean stress and a stress amplitude σ_0. Goodman's relationship [14], which assumes a linear effect of mean stress between $\sigma_m = 0$ and σ_{UTS}:

$$\sigma_a = \sigma_0 \left[1 - \frac{\sigma_m}{\sigma_{UTS}}\right] \tag{6}$$

Gerber's relationship [15], which assumes a parabolic effect of mean stress between $\sigma_m = 0$ and σ_{UTS}:

$$\sigma_a = \sigma_0 \left[1 - \left(\frac{\sigma_m}{\sigma_{UTS}}\right)^2\right] \tag{7}$$

Soderberg's relationship [16], which assumes a linear effect of mean stress between $\sigma_m = 0$ and σ_y:

$$\sigma_a = \sigma_0 \left[1 - \frac{\sigma_m}{\sigma_y}\right] \tag{8}$$

In all these relationships, σ_m is the mean stress, σ_a is the fatigue strength in terms of stress amplitude when $\sigma_m \neq 0$, σ_0 is the fatigue strength in terms of stress amplitude when σ_m=0, σ_{UTS} is the monotonic ultimate tensile strength, and σ_y is the monotonic yield stress.

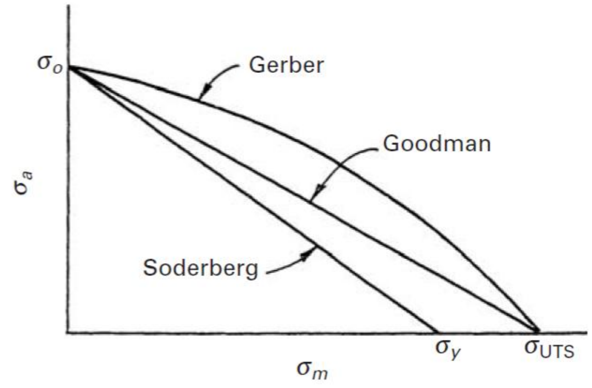

Figure 6. Gerber, Goodman and Soderberg diagrams, showing mean stress effect on fatigue life [11]**.**

Figure 6 shows the three relations schematically. Experimentally, it has been observed that the majority of data for metals falls between the Gerber and Goodman lines [9]. Thus, the Goodman diagram represents a conservative estimate of the means stress effect. These three expressions involve uniaxial stresses. In most real-life situations, materials encounter biaxial and triaxial situations. Such empirical approaches can provide estimates of lifetime, usually only under simple, uniaxial loading conditions. The material parameters involved need to be determined by experiment and for each material vary with microstructure (grain size, precipitate distribution) and with loading conditions (temperature, stress state). They provide no insight in to the micromechanics of the crack initiation and growth processes and how it is influenced by microstructure and so can only be used for extrapolation with great care. A completely novel approach has been developed by Prof. Fionn Dunne's group[8] in the Department of Engineering, Oxford University, wherein, a representative region of the material, containing about grains can be modelled using crystal plasticity and a finite element approach, taking account of the grain morphology and crystallographic orientation. One of the aims of this project is to provide validation data (experimentally measured strain states and lattice rotations) to the crystal-plasticity finite element model so that direct comparisons can be made.

2.2. Crack initiation in Fatigue

Crack initiation commonly occurs at the surface, at stress amplification sites such as inclusion-matrix interfaces [17-21] and surface scratches, in slip bands [17], [19], [22], [23], and at grain boundaries [24]. Surface cracking generally results from the way in which common loading of components leads to the maximum stress occurring at the extremes, these being an outer surface. At the surface there is also a lack of constraint from the surrounding matrix, which allows for easier crack initiation. Points of maximum stress or where the stress is considerably higher than the surrounding matrix are likely to incur crack initiation due to yielding of the material. Grain deformation under cyclic loading is often accommodated through displacement along slip bands resulting in a visible toughening of the material's surface [9]. Also, the surface is exposed to air (or other atmosphere), so that environmental effects are maximised at the surface.

Interrupting the fatigue test to remove the deformed surface by electropolishing can facilitate a study of crack formation in fatigue. There will generally be several slip bands, which are more persistent than the rest and which will remain visible when the other slip lines have been polished away. The ‘valleys’ so generated (Figure 7) act as micronotches with the effect being that stress is intensified at these points promoting additional slip and eventually microcrack initiation [9], [25].

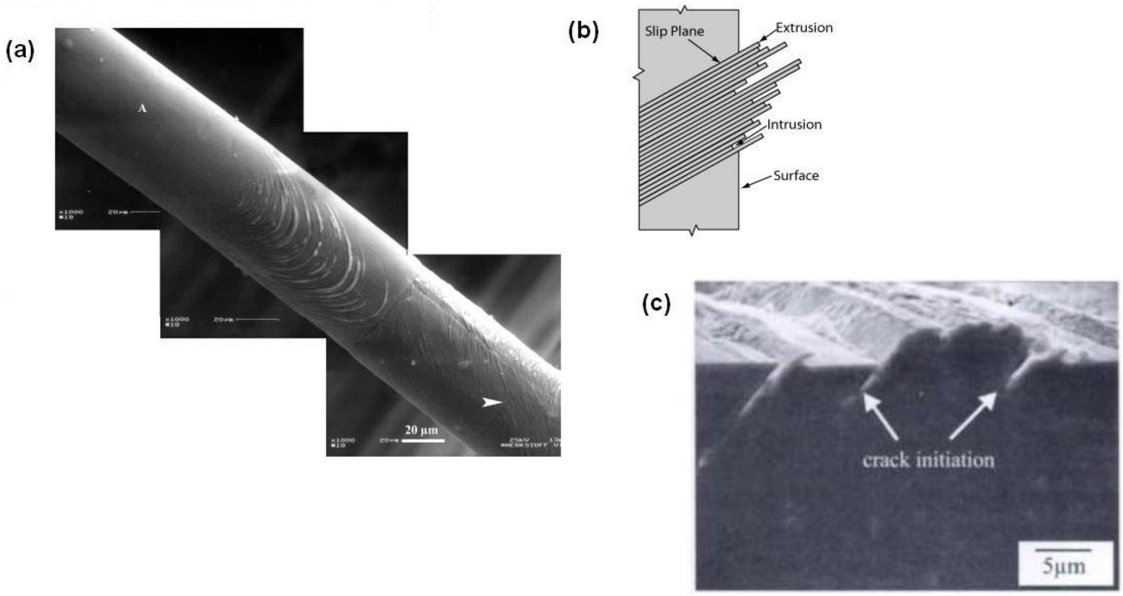

Figure 7. (a) Slip bands formation on the surface of a Copper wire after cyclic loading ($\varepsilon = 2.6 \times 10^{-4}$, number of cycles (N)= 10^{8}) (b) a schematic showing areas that rise above (extrusion) or fall below (intrusion) the surface of a component due to movement of material along slip planes. (c) a crack at the edge of a persistent slip band [9]**.**

Another factor contributing to crack initiation, for materials containing inclusions, is that the fabrication process can often leave the inclusions fractured, so that pre-existing microscopic cracks can be present within these inclusions before the onset of any loading [18], [20], [26]. We can expect higher initial stresses to be present at the boundary between the matrix and the inclusions, encouraging crack initiation and propagation to occur along or near these interfaces [27].

Grain boundary cracking may be the result of the grain boundary's inability to accommodate the cyclic deformations occurring in neighbouring grains, which may be increasingly likely in low cycle fatigue (LCF – a condition when failure occurs at relatively high stress and low number of cycles to failure ~ 10^5 or lower) where the strains are inherently much larger. The resulting severe strain gradients across the interface can provide an additional shearing mechanism that would contribute to the initiation of cracks [28], [29]. The large difference in orientation or mismatch between the two neighbouring grains at a high-angle grain boundary makes it very difficult, if not impossible, for slip to be transferred from one grain to the other. Therefore dislocation build-up is likely to occur leading to microcrack initiation at the grain boundary.

The aim of this project is to improve our basic understanding and attempt to quantify deformation around potential crack initiation sites in single and polycrystalline materials. The following literature presents a finite element polycrystal plasticity model, capable of predicting a wide range of crystal plasticity behaviour that has been employed by collaborators in this project to estimate the lattice strain, rotations and geometrically necessary dislocation (GND) density around potential crack initiation sites. Soon after, an experimental technique for strain and lattice rotation measurement based on electron backscatter diffraction (EBSD) in the scanning electron microscope (SEM) is introduced.

2.3. Crystal Plasticity Finite Element modelling

With increasing developments in recent years, the need to deal with design and manufacturing issues at the micron and sub-micron level has arisen. As a result, there has been an increased interest in modelling plastic deformation at small lengthscales. Clearly some microscopic understanding of plasticity is necessary in order to accurately describe deformation at small length scales. Past and recent experiments have shown that materials display strong length scale effects when the characteristic length scale associated with non-uniform plastic deformation is in the order of a several microns. The most famous one perhaps is the Hall-Petch effect [30], [31] in polycrystals: the overall flow stress increases as the grain size decreases at a given overall strain. As observed by Fleck and Muller et al [32], thin wires ranging in diameter from 12μm to 170μm were stronger under torsion when the diameter of the specimens was smaller. Simultaneously, Stolken and Evans [33] observed that thin beams ranging in thickness from 12.5μm to 50μm were stronger under bending when the thickness of the beams was smaller. These phenomena may not all have the same explanation, but it is clear that all require a length scale for their interpretation. However, the conventional crystal plasticity theories cannot predict these length scale effects of material behaviour at the micron scale because their constitutive models possess no internal length scale.

Crystal plasticity theory first introduced by Taylor [34] incorporated micromechanics into macroscopic analyses of plastic flow. In this theory, the incremental deformation in a crystal is treated as a sum of contributions from two independent atomic mechanisms. On a macroscopic scale, these contributions are (i) an overall 'elastic' distortion of the lattice; (ii) 'plastic' simple shears due to dislocation slip. The shears have specific crystallographic planes and directions, each associated pair of which defines a 'slip system'. At each stage of a loading programme the particular 'potentially active' systems are considered to be uniquely determined by the current applied stress: its shearing component τ must attain a critical value. Schmid [35] postulated this theory that yield would only begin on a slip system when the resolved shear stress on the slip plane and in the slip direction reached a critical value. This statement is now commonly referred to as Schmid's law.

Even though the total macroscopic deformation is small sometimes the local strains can be very large. Hence it is necessary to develop a kinematics for large deformation. The conventional crystal plasticity theory was extended for large deformation by Hill [36] and Rice [37]. Lee [38], Asaro and Rice [39] and Peirce et al [40] have shown that the crystal lattice rotates while it deforms. The total deformation gradient can be given by [38]:

$$F = F^e F^P \tag{9}$$

where F^P, the plastic deformation gradient, is solely due to crystal slip, while F^e, the elastic deformation gradient, is associated with stretching and rotation of the atomic lattice.

Then the velocity gradient L can be given by:

$$L = \dot{F} \cdot F^{-1} \tag{10}$$

and L can be decomposed into the *deformation rate*, D (the symmetric part of L), and the continuum spin tensor, W (the antisymmetric part of L) as

$$L = D + W \tag{11}$$

where $D = sym(L) = \frac{L+L^T}{2}$and $W = asym(L) = \frac{L-L^T}{2}$

Further, D and Wcan be decomposed into plastic and elastic parts as follows:

$$D = D^e + D^P \tag{12}$$

$$W = W^e + W^P \tag{13}$$

The plastic velocity gradient L^P is computed as the sum of shear rates on all active slip systems:

$$L^P = \sum_{\alpha=1}^{k} \dot{\gamma}^\alpha s^\alpha \otimes n^\alpha \tag{14}$$

where k is the total number of active slip systems and $\dot{\gamma}^\alpha$ is the shear rate on the α^{th} slip system, which is often prescribed by a constitute equation which may be phenomenological or physically based. Often a power law is used to introduce the strain rate dependency. Here, a similar law is used as follows [41]:

$$\dot{\gamma}^\alpha = \begin{cases} 0 & when\, \tau^\alpha < \tau_c^\alpha \\ A \sinh\big(B(\tau^\alpha - \tau_c^\alpha)\big) & when\, \tau^\alpha \geq \tau_c^\alpha \end{cases} \tag{15}$$

where A and B are material property constants.

The rate of plastic deformation and plastic spin are then given as

$$D^P = sym(L^P) = \frac{L^P + L^{P^T}}{2} \tag{16}$$

$$W^P = asym(L^P) = \frac{L^P - L^{P^T}}{2} \tag{17}$$

The corresponding elastic terms are obtained by

$$D^e = D - D^P \text{ and } W^e = W - W^P \tag{18}$$

Then the co-rotational stress rate (or the Jaumann stress rate – an objective stress rate that results purely from the constitutive response of the material and not from rigid body rotation) can be described according to isotropic Hooke's law

$$\overset{\triangledown}{\sigma} = 2G(D^e) + \lambda tr(D^e)I \tag{19}$$

where G and λ are the shear modulus and Lame elastic constant respectively, and can be expressed by

$$G = \frac{E}{2(1+\nu)}$$

$$\lambda = \frac{E\nu}{(1+\nu)(1-2\nu)} \tag{20}$$

where E is the Young's modulus, and ν Poisson's ratio.

The orientation of the slip systems is taken to evolve as:

$$\dot{n}^\alpha = W^e n^\alpha \tag{21}$$

$$\dot{s}^{\alpha} = W^{e} s^{\alpha} \tag{22}$$

These equations are often used in the implementation of plasticity models into finite element code, by following the procedure below.

For small deformation problems, when the deformation gradient (F) and its rate $(\dot{F})$ are known, the following steps may be used to determine the stresses.

(1) Determine the velocity gradient (L) – Equation (10)

(2) Determine the rates of deformation and continuum spin $(D$ and $W)$ – Equations (12) and (13)

(3) Defining the rate of plastic deformation by specifying a constitutive equation(D^{P}) – Equations (14), (15) and (16)

(4) Determine the rate of elastic deformation(D^{e}) – Equation (18)

(5) Determine the Jaumann stress rate using the tensor form of Hooke's law $(\overset{\triangledown}{\sigma})$ from the rate of elastic deformation – Equation (19)

(6) Determine the material rate of stress $\dot{\boldsymbol{\sigma}}$ using $\overset{\triangledown}{\sigma}$ and W.

(7) Use a numerical technique to obtain the stresses with respect to the material reference frame by integrating $\dot{\boldsymbol{\sigma}}$.

The plastic rate of deformation D^{P} is specified by a constitutive equation. Often, in finite element implementations, the total rate of deformation D is known such that if D^{P} is specified by a constitutive equation, then D^{e} can be determined using the above specified relation so that the stress rate may be determined using Hooke's law. Once we know the stress rate, we can integrate over time to determine stress.

A natural way to include the lengthscale effects is by introducing them in the constitutive law. Fleck and Muller[32] adopted an approach (that the yield stress doesn't only depend on plastic strain but also on plastic strain gradient) and provided evidence for material hardening due to plastic strain gradients by experiments on tension and torsion responses of thin copper wires. Plastic strain gradients appear either because of the geometry of loading or because the material itself is plastically inhomogeneous.

A phenomenological theory of strain gradient plasticity to represent the relative roles of strain hardening and strain gradient hardening was thus introduced by Fleck et al [32], [42], [43], and followed by several others including Nix and Gao [44], [45], Backes et al [46]. For these models, particular values of material parameters are not always realistic and different problems often require different values. Some more physical approaches were developed by Gao, Huang et al [47]. These models are physically based but involve higher-order stresses and higher-order (or additional) governing equations and extra boundary conditions. Higher-order boundary conditions may not be uniquely defined and/or can be difficult to satisfy. The length scale effects in these models have often been attributed to geometrically necessary dislocations(GNDs), which are associated with non-uniform plastic deformation where a plastic strain gradient exists. This gives a link between the strain gradients and physical process of dislocation accumulation in the material.

2.3.1. *GNDs and SSDs*

Dislocations are generated and stored when a crystal is deformed. In descriptions of dislocations in crystals, dislocation densities can be separated into two different contributions: geometrically necessary dislocations (GNDs) and statistically stored dislocations (SSDs) (strictly speaking, it is not possible to assign a given dislocation as GND or SSD, but for a given region, the density can be split into two parts). GNDs appear in strain gradient fields where they are required for compatible deformation of various parts of crystals, and statistically stored dislocations (SSDs) accumulate by trapping each other randomly [48]. The storage of both GNDs and SSDs causes material to work harden.

Geometrically necessary dislocations represent an extra storage of dislocations required to accommodate the lattice curvature that arises whenever there is a non-uniform plastic deformation. These ‘geometrically necessary’ dislocations do not contribute to plastic strain (although they can contribute to intragranular stress variation) but act as obstacles to the motion of those ‘statistically stored’ dislocations and hence contribute to the work hardening of the material. These dislocations manifest their effects when the characteristic length of deformation becomes sufficiently small. This is the basic idea of geometrically necessary dislocations [49].

Fleck et al [32] have shown how the process of GND accumulation leads to lattice curvature by a schematic sketch. Consider a beam made from three single crystal rectangular cells of side δx_1, $\delta x_2$and aligned with the Cartesian axes (x_1, x_2, x_3), where the normal to the slip plane m is parallel to the x_2 direction and the slip direction s is along the x_1 direction, as shown in Figure 8. The geometrically necessary dislocations with a density of ρ_g

$$\rho_g = \frac{\Delta n}{\delta x_1 \delta x_2} = \frac{1}{b}\frac{\delta y}{\delta x_1} \tag{23}$$

are stored on the system, where n is the number of dipoles in a cell (assumed to be large, although only a small number of dislocations are show in the figure) and b is the Burger's vector.

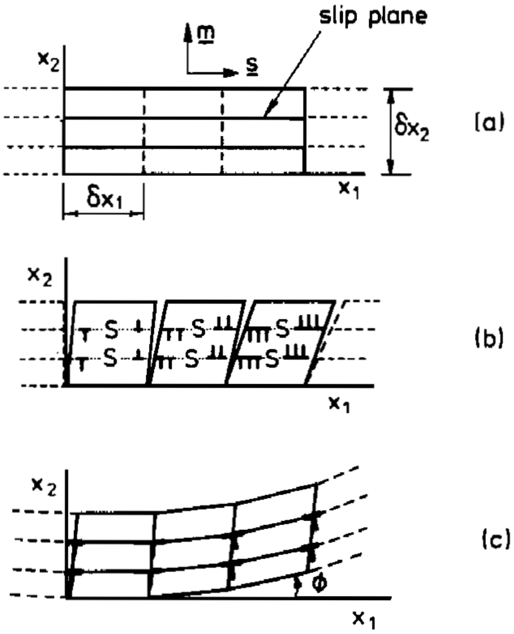

Figure 8. Sketch showing that a gradient of slip in the x_1 direction causes a density $\rho_g$of geometrically necessary dislocations to be stored. Plastic slip is assumed to occur on a single slip system with unit normal m aligned with the x_2 axis, and the slip direction s aligned with the x_1 axis **[32].**

There has been considerable recent interest aimed at developing a predictive theory governing the plastic deformation of crystalline solids at the micron level. Many people modelled size-dependent plasticity based on the framework of geometrically necessary dislocations first introduced by Nye [7] and furthered by Kroner [50], including Fleck et al [32], Nix and Gao [44], [45]. All these models have shown an excellent description of size dependence effects.

In 2007, a 2D lengthscale-dependent, physically based crystal plasticity model was introduced by Dunne et al [8] in which an explicit coupling between density of GNDs and crystallographic slip is incorporated. The effect of strain gradient was brought into the flow rule through the slip rate. The theory preserved the classical structure of incremental boundary value problems and does not require higher-order stresses or additional boundary conditions. This was later extended by Liang et al [51] to full three-dimensional large deformation problems. Several comparisons have already been made between predicted GND distributions with experimentally determined densities in Aluminium bicrystals [52], [53] and near indents in commercially pure Titanium[54]. The model is discussed clearly in §3.5.

The aim of this research is to experimentally measure the strains, lattice rotations and GND densities around several microstructural features in a Nickel based superalloy and compare measurement to predictions from Dunne's crystal plasticity model. For this purpose, we have compared predictions first based on thermal loads (from ordinary heat treatment cycles) and then followed by mechanical deformation. Experimental measurements have been made based on a high resolution electron backscatter diffraction (EBSD) analysis in the scanning electron microscope, described in detail in the following sections §2.5 and §3.4 . Geometrically necessary dislocations have been related to lattice curvature through Nye's tensor [7].

2.4. Electron Backscatter Diffraction (EBSD)

Nickel in a single-crystal form is elastically anisotropic. Hence, the stiffness is dependent upon the crystallographic orientation relative to the loading configuration. The knowledge of crystal orientations is thus very important, in order to understand the specifics of the deformation processes, both elastic and plastic. Electron backscatter diffraction is a technique that can be used to determine crystal orientation in test samples. This technique is a clear choice in this project, due to the ease in sample preparation and high resolution (both lateral and angular).

An EBSD detector is often installed as an additional characterisation technique in a scanning electron microscope (SEM). It enables us to acquire individual grain orientations, local texture, point-to-point mis-orientations, phase identification and distribution.

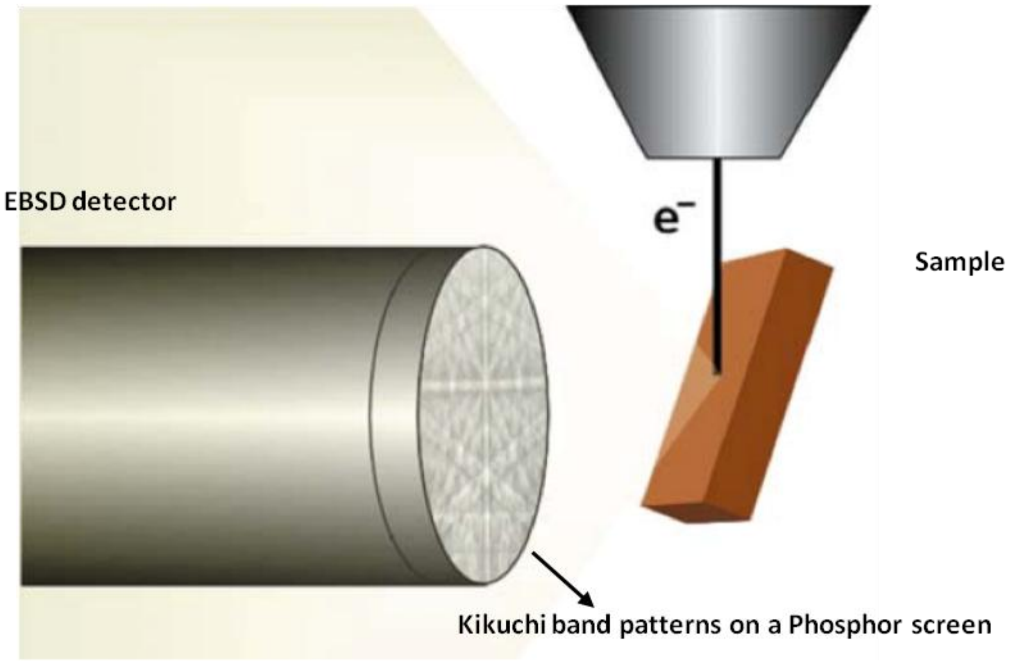

Figure 9. Schematic of typical formation of Kikuchi patterns in EBSD[55]**.**

A detailed presentation of the EBSD technique can be found in Randle and Engler's book on texture analysis [56]. Although the whole EBSD analytical process is automated, it is desirable to have fundamental understanding of the physical principles upon which EBSD is based.

2.4.1. The formation of Kikuchi Band Patterns (or EBSP)

The diffracted electrons from near the sample surface form a characteristic pattern on the screen, known as the *kikuchi diffraction pattern* [57]. When the electron beam strikes the sample, electrons are scattered in all directions. This means that, for each family of lattice planes, there will be electrons arriving at the Bragg diffraction angle θ_B and can diffract as per Bragg's law (Equation (24) and Figure 10):

$$\lambda = 2d \sin \theta \tag{24}$$

where the wavelength, λ, is determined by the energy of the incoming electron beam and d is the inter-planar spacing of a diffracting plane (sometimes referred to as reflecting plane or reflector) plane in the crystal lattice of the sample.

For typical values of interplanar spacing and electron wavelength, the resulting diffracting cones form an apex angle of nearly 180^0, so that when one of the cones strikes the phosphor screen, it appears as a straight line. Since there will be lattice planes to either side of the original electron source, there will be two cones, one from either side. They will strike the screen almost parallel to one another, separated by an angular distance $2\theta_B$, which is inversely proportional to the spacing between the lattice planes. If some sort of recording medium – a phosphor screen interfaced to a camera or a piece of film – is positioned so as to intercept the diffraction cones, a pair of parallel conic sections results, which are so nearly straight that they generally appear to be parallel lines.

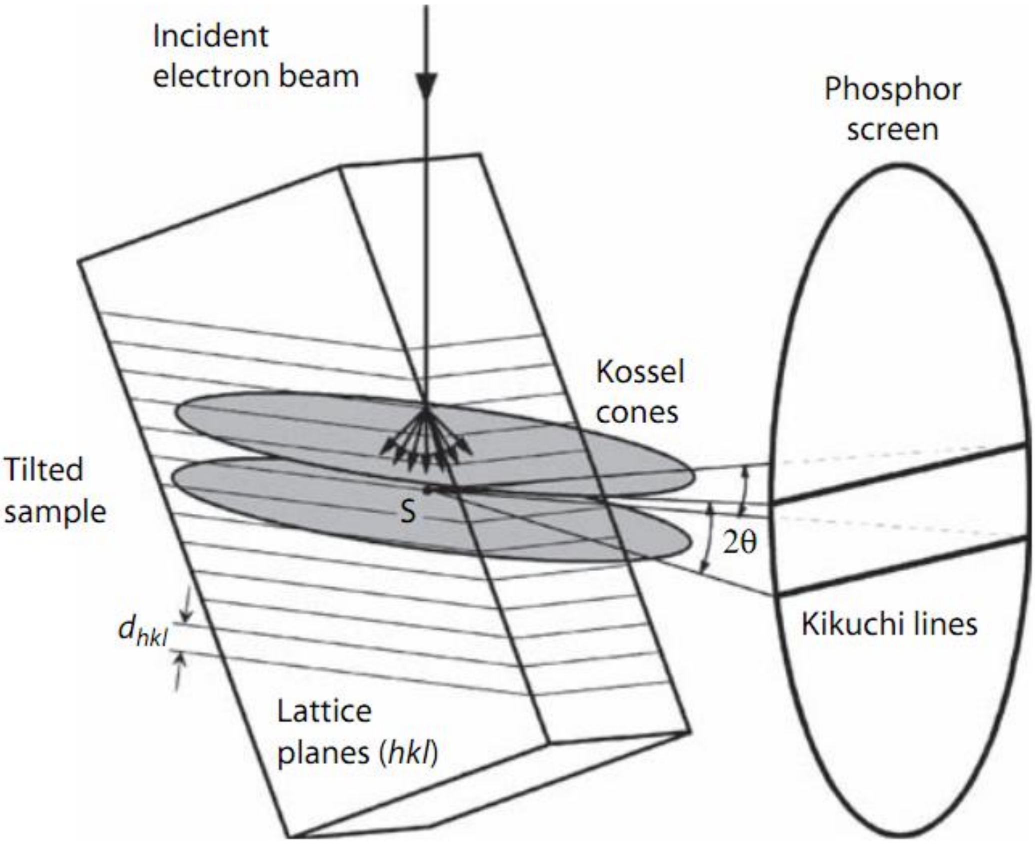

Figure 10. Origin of kikuchi lines from EBSD[56]**.**

These bands were originally observed by inserting a photographic plate inside the SEM[58], and are now observed on a phosphor scintillator inside the microscope. This projection on the phosphor screen is called either an Electron Backscatter Pattern (EBSP) or a Kikuchi (band) pattern, and example from Nickel can be seen in Figure 11.

The sample is highly tilted to ensure that the greatest contrast in the EBSP is found. An angle of 70^0 has been used both for historic reasons (as it is convenient for calibration) and this angle was empirically found to balance high contrast in the resulting EBSP, as diffracted electrons can easily escape and collide with phosphor [59], with limited image distortion and shadowing on the surface due to topography.

Even at this high tilt, the signal produced is low, requiring low light CCD cameras to image the phosphor scintillator and relatively high beam currents to be employed (compared to standard SEM imaging).

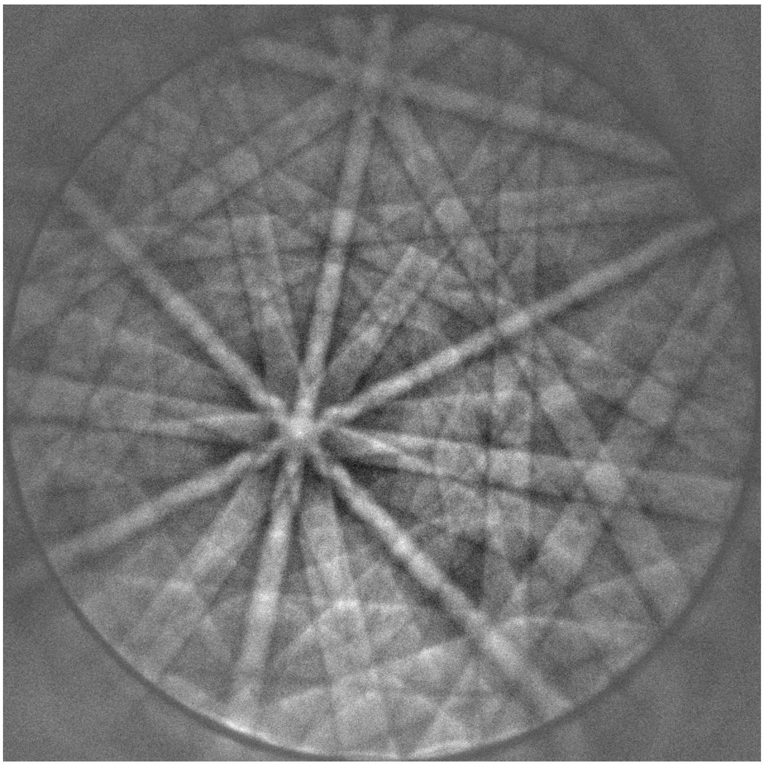

Figure 11. An EBSP from Nickel.

2.4.2. Interpretation and analysis of EBSPs

Once the EBSD patterns are generated on the phosphor screen and recorded in an associated computer, a series of analysis stages will be performed to identify the orientations of the diffracting crystal. Wright [60] reviewed the processes of automated determination of crystallographic orientation from electron backscatter diffraction (EBSD) patterns. First of all, since the acquired EBSD pattern images generally have a very low signal-to-noise ratio, several image-processing techniques can be applied to improve the image quality for subsequent analysis. Firstly, in order to reduce temporal noise from the EBSD pattern image, a number of images can be integrated with the incident beam in a stationary position. Then a background correction is performed to improve the contrast of the kikuchi bands by removing any long-range intensity gradients. An averaged background pattern is collected from all grains in the field of view in the SEM, and is then subtracted or divided from all subsequent EBSD patterns. At the final image processing stage the EBSD pattern image can be compressed to a smaller size if required (by replacing a box of pixels by an averaged single pixel – often termed as ‘binning’). This compression process saves a huge amount of time in subsequent analyses. Additionally, the intensity histogram will be equalised so as to further improve the pattern contrast.

The approach for detecting diffraction bands, commonly used in the current commercial EBSD software, is the modified Hough transform [61], [62]. In this method, an EBSD image is transformed into Hough space; sharp lines in the image space are represented as single points in the Hough space. The central equation of the Hough transform is:

$$\rho = x\cos\theta + y\sin\theta \tag{25}$$

This can be rearranged as:

$$y = -\frac{1}{\tan\theta}x + \frac{\rho}{\sin\theta} \tag{26}$$

where (x, y) denote the pixel coordinate in the EBSD image and the ρ, θ define the axes of the Hough transform in which a given (ρ, θ) corresponds to a line in the original image space. Diffraction lines in an EBSD pattern are now transformed into detecting single points in the Hough space, which are readily detected. The relationship is clearly shown in Figure 12.

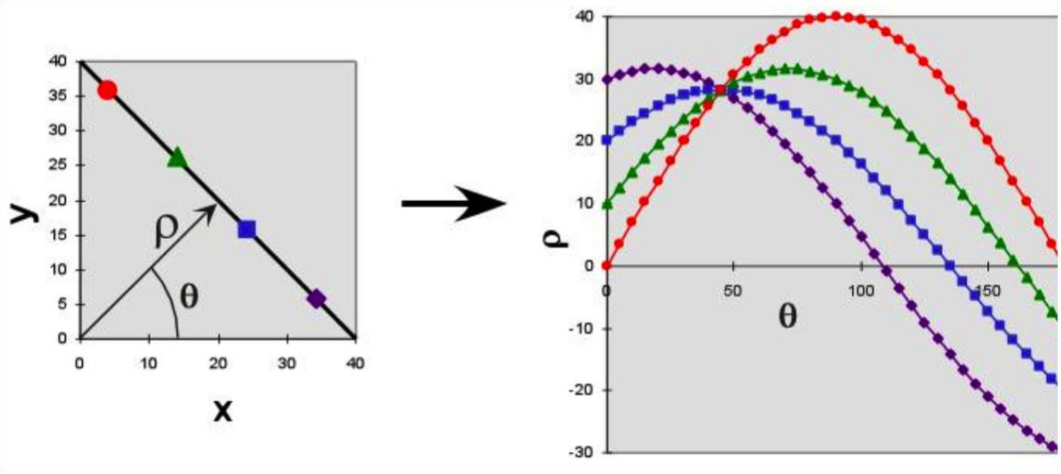

Figure 12. Schematic of Hough transform parameters[61].

With this technique, a point in the pattern can now be converted to a sinusoidal curve representing all the straight lines that could pass through that point. The curves for points on a line will all intersect at one point corresponding to that line, and that point then corresponds to the Kikuchi band in the pattern. Since the EBSD pattern is a grey-scale rather than black and white, it is necessary to give each point a weight corresponding to its intensity in the original pattern; the resulting transform is referred to as a Radon transform. Thus, the problem of finding a band (denoted by a linear set of high intensity pixels) in the diffraction pattern is reduced to finding a point of high intensity in the Hough transform. These high-intensity points are easily detected by pattern recognition software; the location of these bands can then be used to index the pattern using the procedure from the mathematical principles stated above. The calculated angles between the planes corresponding to located Kikuchi bands are compared to the expected angles for the known crystal structure. The best match between measured interplanar angles and those expected for the known crystal type allows the pattern to be indexed and hence the crystal orientation calculated [61].

The first step in determining the orientation is to determine the indices of the bands and/or zone axes in the pattern. In Figure 13, x^s, y^s and z^s are the sample coordinate axes, x^{screen} and y^{screen} are the coordinate axes on the screen, Z_{SSD} is the distance from the specimen to the screen, X_{PC} and Y_{PC} are the screen coordinates of the pattern center, r_i is the three-dimensional vector of a point on the screen, and x_i^*, y_i^* are the coordinates of the same point in the screen coordinate system. Z_{SSD}, X_{PC} and Y_{PC} are parameters of the microscope hardware and not of the specific pattern, so they are determined during calibration and will already be known during pattern indexing.

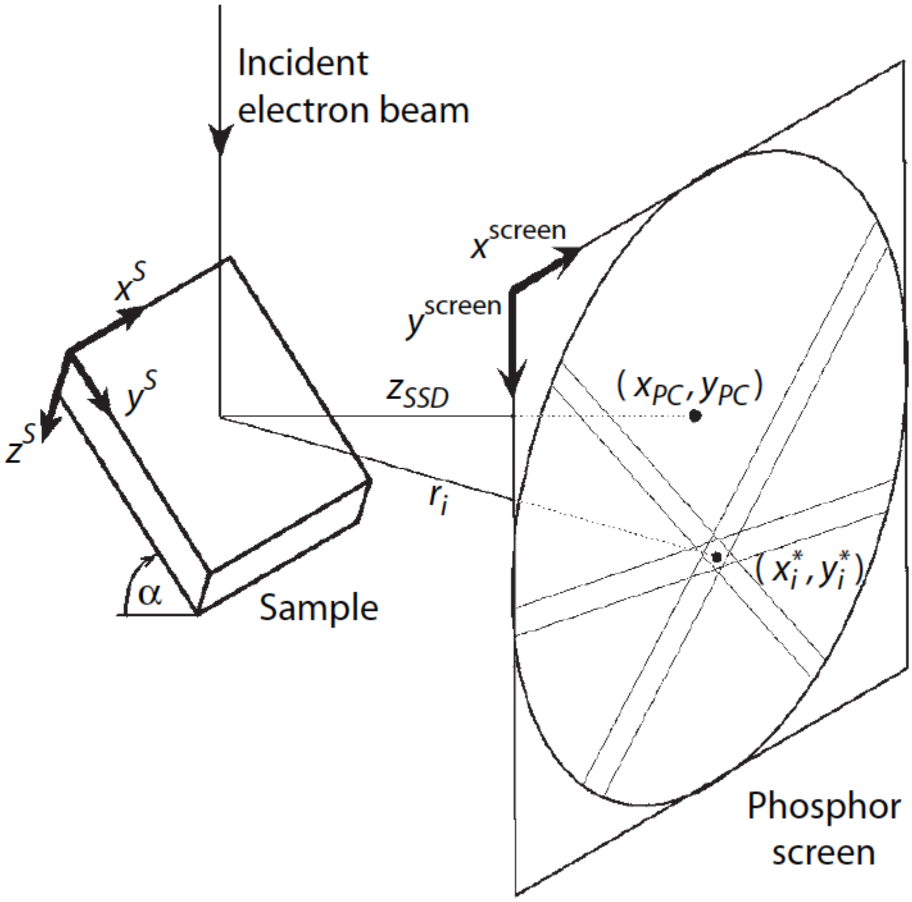

Figure 13. Indexing of Kikuchi pattern [56]**.**

In order to index the pattern, three different zone axes or bands are chosen, and their screen positions x_i^* and y_i^* are converted into their position in the sample coordinate system $\boldsymbol{r_i}$**:**

$$\boldsymbol{r_i} = \begin{pmatrix} x_i^s \\ y_i^s \\ z_i^s \end{pmatrix} = \boldsymbol{A} \cdot \begin{pmatrix} x_i \\ y_i \\ z_i \end{pmatrix} = \boldsymbol{A} \cdot \begin{pmatrix} x_i^* - x_{PC} \\ y_i^* - y_{PC} \\ z_{SSD} \end{pmatrix} \tag{27}$$

where $\boldsymbol{A}$ is the rotation matrix to compensate for the geometrical factors such as the tilt of the sample and possible further tilt of the camera. Once the positions of the bands and axes are determined, the angles between the vectors can be determined using the dot product. These angles are compared to all possible angle combinations for the known crystal structure being examined in order to determine the indices of each band.

Once the pattern has been indexed, the three vectors $\boldsymbol{r_i}$ are known both in the coordinate system of the sample $(\boldsymbol{r_i^s})$ and in the crystallographic coordinate system$(\boldsymbol{r_i^c})$, the next step, therefore, is to determine the relationship between these two coordinate systems. This is done by computing the orientation matrix $\boldsymbol{g}$, which is defined by:

$$\boldsymbol{r_i^c} = \boldsymbol{g}\,\boldsymbol{r_i^s} \tag{28}$$

Since three sets of both $\boldsymbol{r_i^c}$ and $\boldsymbol{r_i^s}$ are known, it follows from this definition that:

$$\begin{pmatrix} x_1^c & x_2^c & x_3^c \\ y_1^c & y_2^c & y_3^c \\ z_1^c & z_2^c & z_3^c \end{pmatrix} = \boldsymbol{g} \cdot \begin{pmatrix} x_1^s & x_2^s & x_3^s \\ y_1^s & y_2^s & y_3^s \\ z_1^s & z_2^s & z_3^s \end{pmatrix} \tag{29}$$

or, rearranging for $\boldsymbol{g}$,

$$\boldsymbol{g} = \begin{pmatrix} x_1^c & x_2^c & x_3^c \\ y_1^c & y_2^c & y_3^c \\ z_1^c & z_2^c & z_3^c \end{pmatrix} \begin{pmatrix} x_1^s & x_2^s & x_3^s \\ y_1^s & y_2^s & y_3^s \\ z_1^s & z_2^s & z_3^s \end{pmatrix}^{-1} \tag{30}$$

The orientation matrix $\boldsymbol{g}$ now contains all the necessary information about the crystallographic orientation. It can also be saved and used to compute the other orientation measurements such as positions on a pole figure, inverse pole figure, or Euler angles [56].

2.4.3. Spatial and Angular resolution

The average spatial resolution of an EBSD system is about 200-500nm (although resolutions as low as 10 nm have been achieved [63]. This is strongly influenced by:

- Material
- Specimen / microscope geometry
- Accelerating voltage
- Probe current
- Pattern Quality

Material: The amount of backscattered signal increases with atomic number; hence often there is more detail and greater clarity in patterns from high atomic number of elements than from those with low atomic numbers. The higher atomic number causes larger elastic scattering and smaller interaction volumes and so a better spatial resolution can be achieved. The greater pattern contrast can lead to improved angular resolution as band detection improves.

Specimen / microscope geometry: The three main parameters, which can be altered in the physical EBSD set-up are the specimen-to-screen distance, the specimen tilt and the specimen height (‘working distance’) in the microscope. For general EBSD data collection the specimen-to-screen distance, i.e. the camera position, remains fixed. With regard to *specimen tilt*, EBSD patterns have a better contrast with increased tilt angle. Higher tilt angles ($> 80^0$) are impracticable and there is a high degree of distortion and shadowing in the uncorrected image. A tilt angle of 70^0offers a good compromise with regard to convenience and pattern contrast and is often used as a standard angle for EBSD [59]. The ability to work at short working distances (where best spatial resolution and minimised focussing distortions are obtained) for EBSD is often limited by microscope hardware. The risk of collision with microscope hardware, particularly the pole piece, increases at small working distances. The optimum specimen position will depend therefore on the geometry of the microscope. It is also convenient, if possible, to choose a working distance, which locates the pattern center (PC) towards the top half of the phosphor screen. Taking all these factors into consideration, optimum working distances are typically 15-25mm [56].

Accelerating Voltage: Figure 14 shows the relationship between accelerating voltage and average lateral spatial resolution in Nickel as determined in a standard tungsten filament SEM [64].

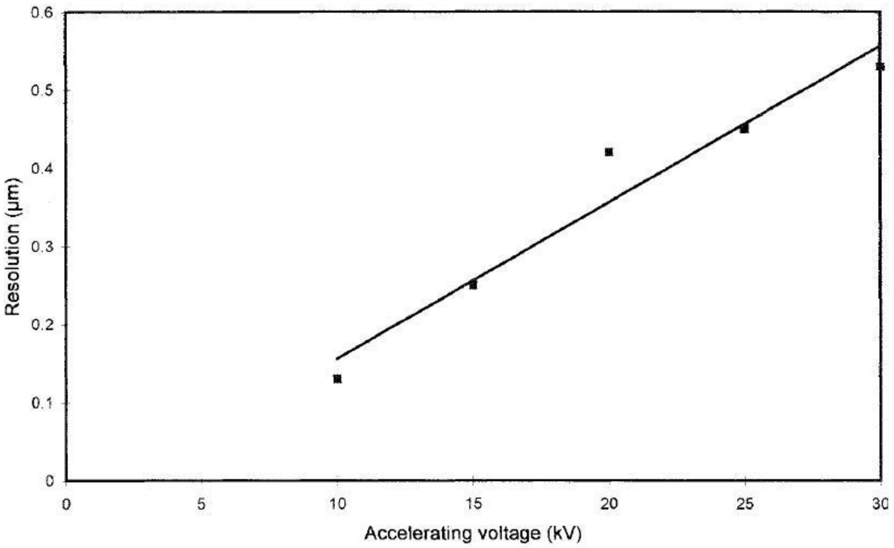

Figure 14. Absolute spatial resolution of EBSD in Nickel as a function of accelerating voltage [64]**.**

The advantages of using a high accelerating voltage, i.e. 30-40kV, are:

- The efficiency of the phosphor screen increases with electron energy (i.e. higher accelerating voltage), which results in a brighter pattern.
- There is less interference from stray electromagnetic fields.

- The electron beam penetrates further, and thus the diffracting pattern originates from a region below the surface such that surface contamination or surface damage effects are minimised.
- The Kikuchi bands are narrow and their center lines are located more precisely leading to better angular resolution.

The disadvantages of using a high acceleration voltage are:

- The beam-specimen interaction volume increases, thus strongly reducing spatial resolution.
- Specimens that are poor conductors or are susceptible to beam damage cannot be examined using a high accelerating voltage, unless the specimen is lightly coated with a conductor.

However, neither the interplanar nor interzonal angles are affected with a change in the acceleration voltage and so the principles of orientation measurement are thus independent of accelerating voltage.

Probe current: The probe current is selected in accordance with the light sensitivity of the camera and the requirement of imaging the specimen surface, and 5nA is a good choice for a modern camera. The best absolute spatial resolution corresponds to the smallest interaction volume, so that small probe currents and small probe diameters are desirable. However for the effective spatial resolution, high signal to noise ratio aids deconvolution of the overlapping patterns making somewhat higher probe currents optimal. Hence, there has to be a compromise between the interaction volume and acceptable pattern clarity.

Pattern quality: Pattern clarity is influenced not only by the quality of the pattern arising from the sampled volume of specimen itself, caused by the presence of lattice defects, but also by 'noise' introduced during pattern capture and processing. Degradation of this type will result when the pattern is averaged over too few frames, or digitised to too few points, or when the back-scattered electron signal is reduced. Use of large probe currents increases significantly the amount of back-scattered signal generated, thus improving the pattern quality.

The '*angular resolution*' of EBSD relates directly to the precision with which the diffraction pattern can be indexed, which in turn is influenced by the calibration of the system, the effectiveness of the software solve routine, the pattern quality and the `magnification' of the diffraction pattern as determined by the camera position. The precision can be usually determined by measuring the misorientation between adjacent sampling points in a well annealed single crystal. The typical angular precision of orientation measurements made by commercial EBSD systems is of the order of 1^0, or 17.5mrad, which is orders of magnitude too large for analysis of elastic strains in most materials systems. A large specimen to screen distance was shown to increase the angular resolution [65] of the EBSD detector, but at the expense of the large capture angle usually employed for orientation measurements. An excellent review of the spatial and angular resolutions that can be achieved in a SEM and the significant improvement of these resolutions in a field emission gun SEM have been well addressed by Humphreys and Brough [66].

2.5. Strain analysis using electron backscatter diffraction

Currently, the major applications of the EBSD technique in academic and industrial use are orientation determination and phase identification. Many researchers in this field have undertaken explorations and developments of this technique. A novel and powerful complimentary application to the EBSD system, in which local elastic strain distribution can be mapped with unique combination of good strain sensitivity and high spatial resolution, has recently been established by Wilkinson [5], [6].

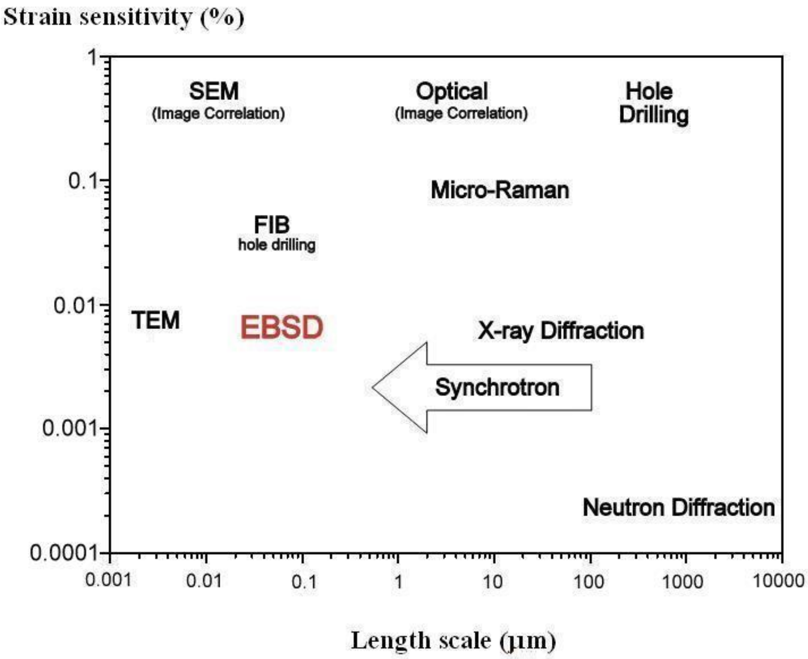

Figure 15. Approximate length scales and strain sensitivities offered by a range of strain analysis techniques. Those towards the bottom left combine superior spatial resolution with superior strain sensitivity [55]**.**

Convergent beam electron diffraction (CBED) based on TEM offers a powerful combination of very high spatial resolution coupled with good strain sensitivity. However, the need for a thin foil is a major limitation that is very difficult to overcome. The stress state in the thin foil is often highly relaxed compared to the original bulk sample and it is at best difficult to undertake *in-situ* loading with any real degree of control. The new cross-correlation technique [5], [6], [67] based on EBSD has shown that strain sensitivities in the order of 2 x 10^{-4} can be achieved without the compromise on wide-angle EBSD patterns (required for Orientation Imaging). Moreover, EBSD does not suffer from the need for a thin foil that limits the CBED method. As Wilkinson observed [5]: strain analysis using image correlation is limited to problems where a ‘before’ and ‘after’ image can be compared, and thus excludes examination of processing routes *etc*. Furthermore, the strain resolution is limited to around 0.05% [68].

As Kikuchi band patterns are generated from a crystal inside the interaction volume, small changes in the crystal will result in changes in the EBSP. If these changes can be characterised and mapped back to the deformation involved, it is possible to obtain high-resolution deformation information about any feature (provided it diffracts) within a material.

Dislocations generated by plastic deformation create a slight but rapidly varying distortions (rotation and tilting) of the crystal within the interaction volume. This results in both: an increase in blurring due to the variation in *d* spacing, within the diffracting volume, which can be identified by a decrease in pattern quality and a slight variation of orientations.

A direct measurement of these EBSD pattern movements/shifts was first made by Wilkinson [65] and Troost [69]. This technique has evolved over the years and the current EBSD pattern image post-process software has been developed to determine the small shifts in these patterns, by comparing obtained EBSD patterns with a strain-free reference using cross-correlation based image analysis [5]. Wilkinson’s approach of applying the cross-correlation functions has provided significantly improved sensitivity in strain tensor and small misorientations (10^{-4} rads) over the conventional EBSD measurements (with sensitivity of ~0.5º, about 0.0087 rads) that cannot be used for elastic deformation studies. The cross-correlation data can be used to examine elastic strains and lattice rotations. The lattice rotations give an indication of plastic deformation and can directly be analysed to evaluate lattice curvature which indicates the presence of geometrically necessary dislocations [6], [7], [70-72].

After a series of patterns is recorded from the sample, including one from the reference region, the shift in the zone axes positions relative to the reference pattern is then found using the following image analysis procedure [6], [55]. The patterns are recorded at the full resolution of the camera. In most instances, good quality patterns obtained using one megapixel camera at full resolution allow a mean angular error of ~10^{-4} radians or less to be obtained. At the heart of the technique is the use of cross correlation analysis to determine pattern shifts, i.e., relative positions of common diffraction contrast features in the test EBSD pattern compared to a reference pattern.

Several sub-regions across the pattern are defined (typically 15-20 of 256x256 pixels) and cross-correlation function is calculated for each of the sub-regions between the reference and the test pattern. The steps are outlined in Figure 16.

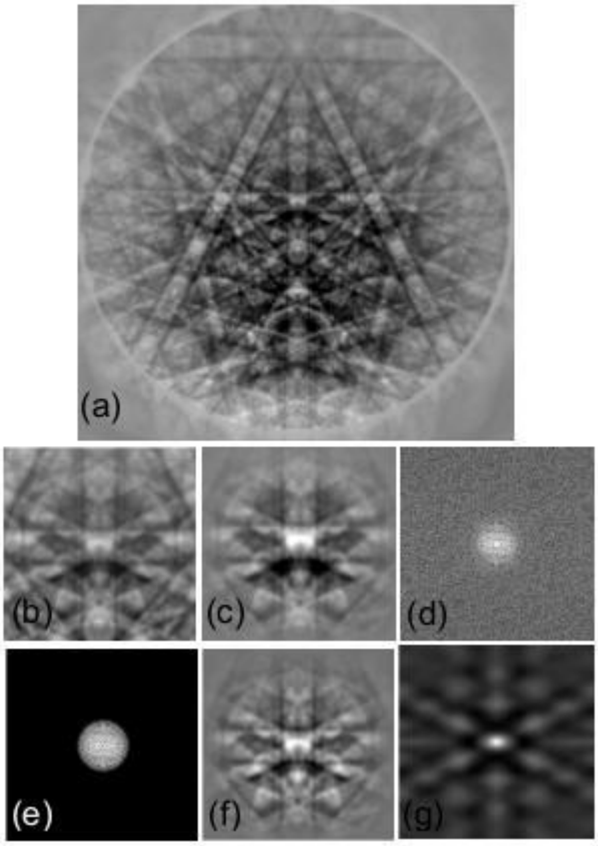

Figure 16. (a) EBSD pattern recorded from GaN (reference pattern) (b) sub-region extracted for analysis (c) intensity and contrast brought smoothly to zero at edges using a weighting function (d) Fourier transform of weighted sub-region (e) application of band pass filter to Fourier transform (f) back transform of filtered Fourier transform (g) cross correlation with test pattern (after similar pre-processing)[55]**.**

In Figure 16(g), the cross correlation function is represented as an intensity distribution in which the ordinates are the pixels. The intensity at a point in the distribution represents the degree of correlation between the reference image and the test image. The magnitude and direction of the displacement is given by the vector defining the point with respect to the centre of the image. The point with maximum intensity is that of maximum correlation between the two images.

The shifts at four or more regions widely spaced across the EBSD patterns determined are sufficient to directly calculate eight of the nine degrees-of-freedom contained in an arbitrary strain and rotation. The remaining degree-of-freedom is the hydrostatic dilation of the lattice to which this method is insensitive.

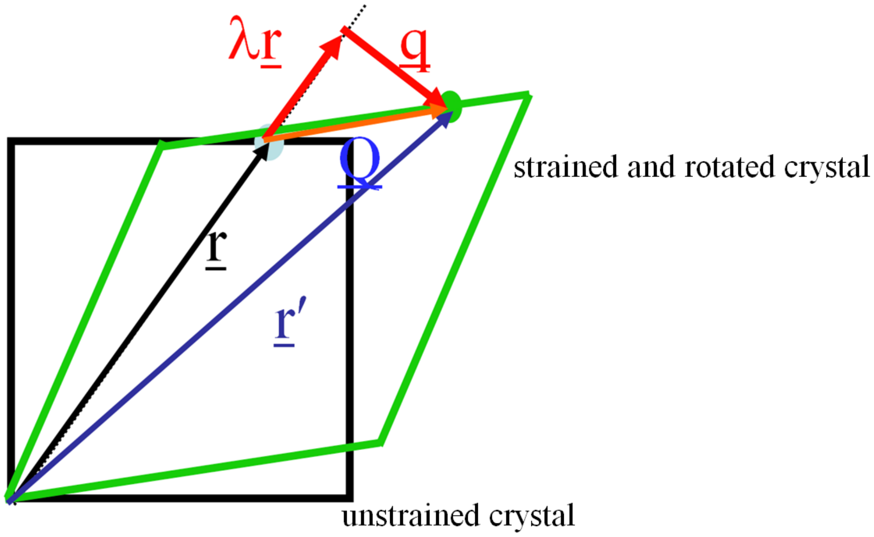

Figure 17. Schematic showing zone axis shift due to strain and rotations (redrawn from [55]***)***

Figure 17 shows the vector relationship of the displacement $\boldsymbol{Q}$ induced by strain and rotation, from $\boldsymbol{r}$ to $\boldsymbol{r}'$, with detected axes shifts $\boldsymbol{q}$, in a strained and rotated crystal with respect to an undistorted reference crystal. The shifts can be used to calculate the deformation tensor, $\boldsymbol{A}$, in the SEM axes

$$\boldsymbol{A}-\boldsymbol{I}=\begin{pmatrix} \frac{\partial u_1}{\partial x_1} & \frac{\partial u_1}{\partial x_2} & \frac{\partial u_1}{\partial x_3} \\ \frac{\partial u_2}{\partial x_1} & \frac{\partial u_2}{\partial x_2} & \frac{\partial u_2}{\partial x_3} \\ \frac{\partial u_3}{\partial x_1} & \frac{\partial u_3}{\partial x_2} & \frac{\partial u_3}{\partial x_3} \end{pmatrix} \tag{31}$$

This is performed by calculating the vector $\boldsymbol{r}$, which describes the location of the ROI (zone axis). Displacements caused by strain and rotations will result in a zone axis shift, as shown in Figure 17, and are related to the deformation tensor, $\boldsymbol{A}$, by:

$$\boldsymbol{Q}=\boldsymbol{r}'-\boldsymbol{r}=(\boldsymbol{A}-\boldsymbol{I})\boldsymbol{r} \tag{32}$$

Since EBSD only can measure shifts in the plane of the phosphor screen, the problem is reduced to a projection of $\boldsymbol{Q}$ perpendicular to the zone axis.

$$\boldsymbol{q}=\boldsymbol{Q}-\boldsymbol{r}=\{\boldsymbol{A}-(\boldsymbol{\lambda}+\boldsymbol{1})\boldsymbol{I}\}\boldsymbol{r} \tag{33}$$

This gives three equations from which λ can be eliminated, resulting in the two equations below with eight unknowns, $\frac{\partial u_i}{\partial x_j}$ (n.b. it is impossible to separate the $\frac{\partial u_i}{\partial x_j}$ components as the final degree of freedom, the hydrostatic dilation or contraction of the lattice does not result in a change in angles between the zone axis and hence no shifts in the EBSP).

$$r_2 r_3 \left[\frac{\partial u_2}{\partial x_2} - \frac{\partial u_3}{\partial x_3}\right] + r_1 r_3 \frac{\partial u_2}{\partial x_1} + r_3^2 \frac{\partial u_2}{\partial x_3} - r_1 r_2 \frac{\partial u_3}{\partial x_1} - r_2^2 \frac{\partial u_3}{\partial x_2} = r_3 q_2 - r_2 q_3 \tag{34}$$

$$r_1 r_3 \left[\frac{\partial u_1}{\partial x_1} - \frac{\partial u_3}{\partial x_3}\right] + r_2 r_3 \frac{\partial u_1}{\partial x_2} + r_3^2 \frac{\partial u_1}{\partial x_3} - r_1^2 \frac{\partial u_3}{\partial x_1} - r_2 r_1 \frac{\partial u_3}{\partial x_2} = r_3 q_1 - r_2 q_3 \tag{35}$$

Provided that there are four or more ROIs used, it is possible to produce a unique solution for the above equation and obtain the distortion tensor, $\boldsymbol{A}$ ($\frac{\partial u_2}{\partial x_2} - \frac{\partial u_3}{\partial x_3}$ and $\frac{\partial u_1}{\partial x_1} - \frac{\partial u_3}{\partial x_3}$) are calculated and cannot be separated), which corresponds to the distorted EBSP. (Measuring at more than four ROI will result in an overdetermined set of equations which can result in a best fit solution being produced, e.g. by using least squares method. The accuracies reported by Wilkinson [5] require at least 20 ROIs of 256x256 pixels to be used).

The displacement tensor can be rotated from the SEM axes systems into the sample axes to produce $\boldsymbol{A}'$. From this distortion matrix, it is possible to directly calculate the elastic shear strains, e_{ij}(symmetric part of the displacement gradient tensor) and the lattice rotations, w_{ij} (anti-symmetric part of the displacement gradient tensor)

$$e_{ij} = \frac{1}{2}\left(\frac{\partial u_i}{\partial x_j} + \frac{\partial u_j}{\partial x_i}\right) \text{ and } w_{ij} = \frac{1}{2}\left(\frac{\partial u_i}{\partial x_j} - \frac{\partial u_j}{\partial x_i}\right) \tag{36}$$

The elastic normal strains and the elastic stress components can be calculated by Hooke's equations [7] assuming that the surface is in plane stress (i.e. $\sigma_{33} = 0$) and by rotating the elastic stiffness constants into the sample frame (by using the Euler angles measured earlier and the known reduced elastic constants).

This analysis can be repeated for all patterns within a map, provided that there is sufficient contrast in the EBSPs to clearly identify the ROI shifts and that the rotation between reference and distorted pattern is less than ~7^0 (as the ROIs will shift outside the search window and result in an inappropriate peak match). Wilkinson et al [5] reported than an accuracy of a ±0.006^0 for rotations and 10^{-4} for strains (as measured on Si/SiGe) can be obtained. This accuracy will vary according to the quality of EBSPs but it is clear that the accuracy is far better than conventional Hough based analysis as a greater amount of information can be obtained from the EBSPs.

At the current stage of the technique, it is possible to examine polycrystals, by choosing individual reference patterns from each grain within a particular area. Recently, Britton et al. [73] have studies dislocations content of macrozones in hot-rolled Ti-6Al-4V. To date, this technique has been used to study functional materials [5], [6], [74], [75], indentations in Si [76], Fe [77] and Ti [54], transformation induced GNDs in steels, GND accumulation during hot rolling and fatigue in polycrystalline Ti-6Al-4V.

3. Experimental Methods

The following section will outline the steps that were necessary in preparing test specimens from the MAR-M-002 nickel-base superalloy barstock supplied by Rolls-Royce. It will go on to describe how the test rigs were designed to carry out monotonic 3-point bend and 4-point bend with fully reversed cyclic loading. The use of EBSD to establish grain orientation and grain morphology will be described. Finally the specific monotonic and cyclic procedures and conditions will be given.

3.1. Material and Heat treatment

The superalloy (Mar-M-002) is a high Tantalum and Niobium containing variant of the well-known Mar-M-200 superalloy. It was supplied by Rolls-Royce as a 13.8mm diameter barstock with the grains directionally solidified along the bar's length. The nominal chemical composition of this alloy, as reported in literature[78], [79] is Cr – 9%, Co – 10%, W – 10%, Al – 5.7%, Ti – 1.5%, Ta – 2.5%, Hf – 1.65%, Ni – bal. and also traces of Mo, Fe, Zr, B, C. This material will allow the test samples to be cut so that a near continuous grain structure is maintained, reducing the experimental problem to one that is pseudo-two dimensional (2-D), in which characterisation of the crystal morphology needs to be performed only on the sample surface.

Ideally tensile loading of the alloy would have been preferred due to the simplicity of the stress and strain state that this would have produced. This was not an option due predominantly to the size limitations of the possible test specimens. The next option seemed to be point loading conducted on simple beam sections cut from the centre of the supplied bar. This seemed to be the convenient option since bending geometry makes it easy to make and mount/remove samples for repeated inspections during interrupted tests.

Simple beam sections (13.5mm × 3mm × 3mm) were then cut out from the centre of the supplied bar using a spark erosion/electro discharge machine. These beams have large columnar grains containing carbide precipitates distributed randomly throughout the matrix. These carbides are elongated along the solidification direction and act as large hard barriers to slip in the metallic matrix.

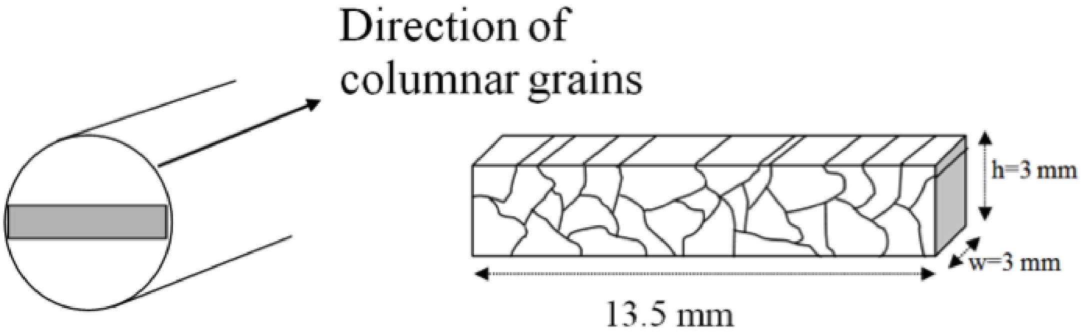

Figure 18. Test specimen from the Mar-M-002 barstock.

As the alloy was supplied by Rolls-Royce in the cast condition, it was necessary to heat-treat the material in order to generate mechanical properties consistent with Rolls-Royce's materials database. This allowed values for Poisson's ratio, Young's modulus and Yield stress to be obtained and linear work hardening to be approximated from the data Rolls-Royce supplied, all of which were needed for finite element (FE) modelling. The heat treatment consisted of two steps, the first being one hour at 1100°C in order to take the material over the γ` transus causing it to dissolve. This was followed by ageing for sixteen hours at 870ºC to precipitate the γ` particles out again, but in a controlled manner. These beam sections were subjected to the above heat treatment in an Argon environment.

In order to prepare some single crystal variants of the same sample, a few of these beam sections were subjected to a repeated heat treatment. The consequence of the double heat treatment was an enlarged grain structure, thus resulting in an almost single crystal beam section.

After the heat treatment, all outer surfaces of these beams have been prepared using the surface preparation methods to avoid any surface scratches that would act as unwanted stress amplification sites. The surface preparation methods first involved grinding the samples by hand using water-cooled silicon carbide paper of successively smaller grit size. The sequence of paper used was PC400, PC800, PC1200 and was conducted on a set of Struers Rotary Grinding Wheels. The next step involved polishing using successively finer grades of diamond abrasive, 3µm and 1µm, following which a final polish of Colloidal Silica was performed. This level of finish usually gives exceptional EBSD results on the surface of the test pieces [61].

Preliminary EBSD done on the heat-treated samples (after a single heat-treatment) revealed a very large grain size (~3mm on an average). The beam samples were mapped on a surface that is normal to the direction of solidification. A grain boundary map is shown in Figure 19.

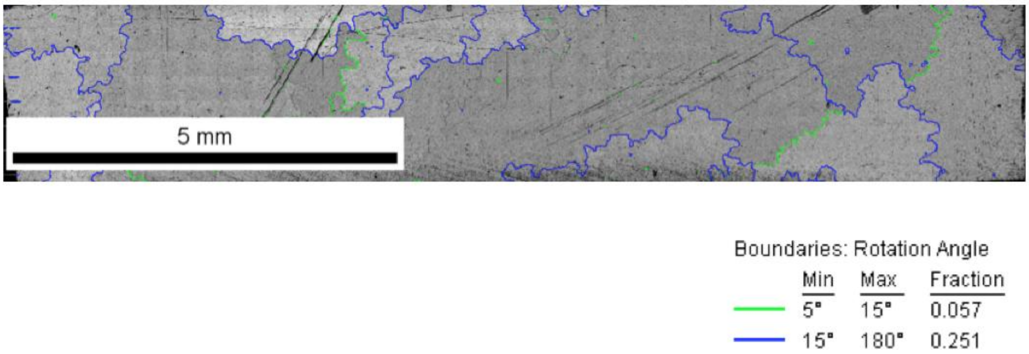

Figure 19. An EBSD map of a beam (after single heat-treatment) showing grains and grain boundaries.

The major phases present in this alloy are austenitic γ matrix, γ' phase and carbides. These carbide particles, as described by Starink et al. [79] and Stephenson at al. [78] are face centred cubic (NaCl structure) MC carbides. These MC carbides are one of the most stable compounds in nature and consequently they form shortly after freezing in MarM002, just as they do in the similar MarM200 alloy [80] and other superalloys [1]. The optical and SEM micrographs reveal that these carbides mostly exist in a Chinese script-like morphology and EDX reveals that the carbides are chemically composed of Ta, Ti, Hf and/or W. One such SEM micrograph is shown in Figure 20(a).

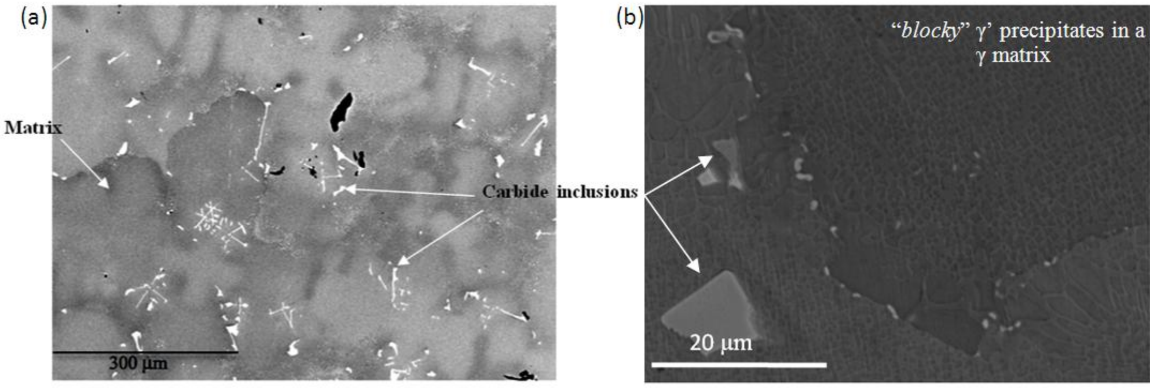

Figure 20. SE images showing (a) carbide particles in the γ-matrix (b) "blocky" γ' precipitates in the γ matrix.

In this context, it must be noted that the reference to these carbides as inclusions/precipitates does not imply that they are defects of any kind. As with most superalloys, these secondary carbide phases/precipitates/inclusions help produce desired strength and ductility characteristics. The features visible on the micrographs in Figure 20 are:

(a) *The ordered intermetallic γ' phase* (basic composition of $Ni_3(Al, Ti)$), which forms in the grains after the solidification is complete. This is the principal high-temperature strengthening phase in most superalloys. The initially formed coarser γ' phase (the size and morphology of which depends on the post solidification cooling rate below 1200ºC) dissolves in the matrix as a result of the heat treatment and then this phase re-precipitates during the ageing step in a cuboidal/blocky form (seen in Figure 20(b)). As a result of these cuboidal structures, more γ' is packed into a given volume. In the as-cast material, several colonies of eutectic γ/γ' (a product of γ-γ' eutectic solidification) have been clearly observed at the end of solidification (1220ºC)[81]. Some of these colonies persist in some areas even after the heat treatment. A few of these colonies can also be observed near the grain boundaries in Figure 20.

(b) *"script" MC carbides (visible in a Chinese script morphology in Figure 20(a)) and "blocky" Hf-rich carbides* - These script MC carbides, (with M=Ti, Ta, W, Hf) *fcc* in structure, usually appear in the melt near the liquidus of this alloy at about 1330ºC and are usually located in the dendritic areas, while the blocky Hf-rich carbides are mainly found in the interdendritic areas[82]. Spilling et al.[81] have observed they do not bear any rotational relationship with the matrix phase, after solidification is complete. During heat treatment (and service), MC carbides usually tend to decompose and generate other carbides, such as $M_{23}C_6$ and/or M_6C. No such lower temperature carbides have been observed in this material after solidification[83], but fine $Cr_{23}C_6$ precipitates are induced in the grain boundaries after the ageing heat treatment[82].

(c) *Serrated grain boundaries* - The heat treatment cycle also assists in precipitation of the finer carbides and coarse primary γ' along the grain-boundary segments, thereby initiating the formation of grain-boundary serration. The slow cooling though the γ' precipitate range aids in the formation of serrated grain boundaries[84-86]. The serrated grain boundaries contribute to strengthening through the retardation of grain-boundary sliding and decrease in stress concentration at grain-boundary triple points[87].

Mechanical strength/hardening. Some hardening results from placing solute atoms in the γ matrix (and γ' phase) of the superalloy (also termed 'solid solution hardening'). These solute atoms affect local atomic arrangement in a grain (and the local modulus), limit diffusion of atoms and change the stacking fault energy (energy associated with one or multiple layer interruption in the stacking sequence of a crystal). Atoms lowering the stacking fault energy (SFE) tend to make it more difficult for dislocations to move in new directions, thereby imparting considerable mechanical strength. Thus, when mobile dislocations (in a lower SFE matrix) in an alloy encounter obstacles, they have more difficulty in moving onto a new plane.

In addition to atoms in solution, both carbide precipitates and the γ’ phase act to impede deformation when they are in a grain (also termed ‘precipitation hardening’). Ordered γ’ precipitates possess an energy (APB or antiphase boundary) representing the extra energy associated with ordered atomic positions versus normal disordered/random positions. APB energy is analogous to SFE mentioned previously. Because of ordering, dislocations in the ordered phase require large amounts of energy to disorder the precipitate as they pass through it. Their role also includes obstructing the movement of grain boundaries, which tend to slide when stressed above about 0.5 of the absolute melting point.

Directionally solidified (DS) versions of cast Nickel superalloys usually have a multiplicity of grains all aligned parallel to each other (usually parallel to the longitudinal or airfoil axis of a turbine blade or vane component), and avoid the formation of transverse grain boundaries. Specific solidification orientations are chosen, depending on the alloy, so as to make it hard for slip to occur along the close packed atomic plane/direction under loading. Sometimes, DS versions may have only one grain (single-crystal directionally solidified) with a specific axis parallel to the airfoil major axis. Such control of grain morphology by directional solidification can alter mechanical and physical properties of the material.

In directional solidification casting, columnar grains (directionally solidified structures) are produced by promoting unidirectional heat flow within the furnace during the solidification cycle. For DS Nickel superalloys, $\langle 100\rangle$ is the preferred natural growth direction. Nickel in single-crystal form is elastically anisotropic. Polycrystalline Nickel displays vales of E and G of 207GPa and 82 GPa [88] respectively, while directionally solidified Nickel displays a stiffness in the growth direction, denoted $E_{\langle 100\rangle}$of 125 GPa, only about 60% of the isotropic value. Thus, at a given stress level, a reduced modulus produces a dramatically lower strain; and hence a DS alloy lasts longer. The single crystal versions of these DS superalloys last even longer, owing partly to the absence of grain boundaries, which do contribute to cracking and failure.

The current alloy (Mar-M-002) has also been solidified in the $\langle 100\rangle$ direction. Preliminary EBSD mapping was performed over the entire surface of the beam in order to establish crystal orientation within each grain. While the doubly heat-treated samples were essentially single crystal (resulting from enormous grain growth due to the repeated heat treatment), polycrystalline samples revealed a strong texture along the cubic orientation. An inverse pole figure (IPF) map of the entire sample area (13.5mm X 3mm) is shown in Figure 21. The IPF key is also shown in the figure, which interprets the colour-coded orientations. Figure 22 depicts the texture on the polycrystalline beam sample.

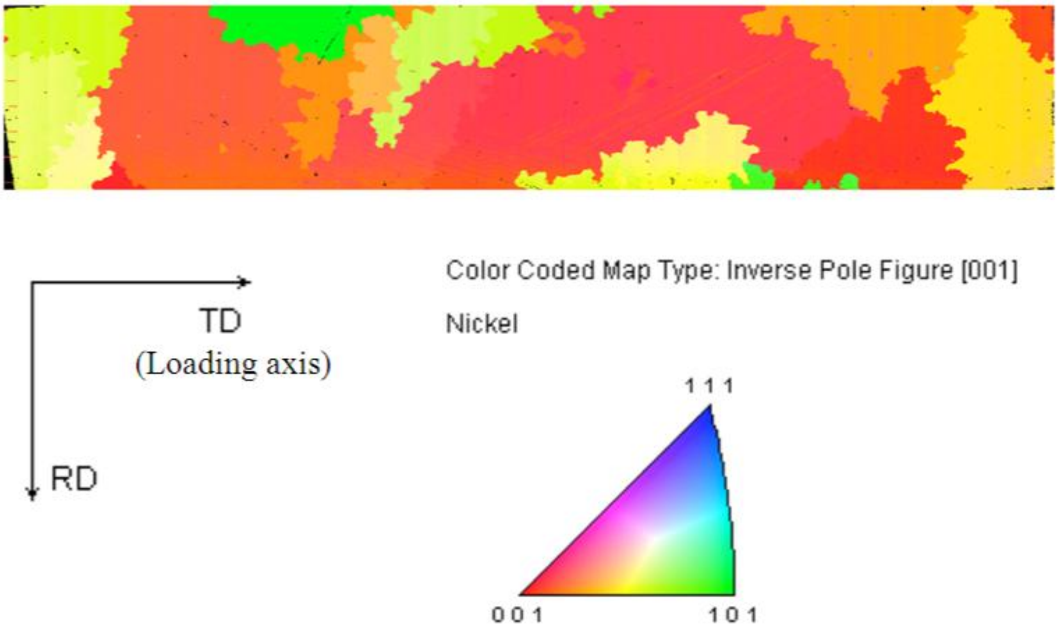

Figure 21. Inverse pole figure map of the polycrystalline sample along the axis of the beam.

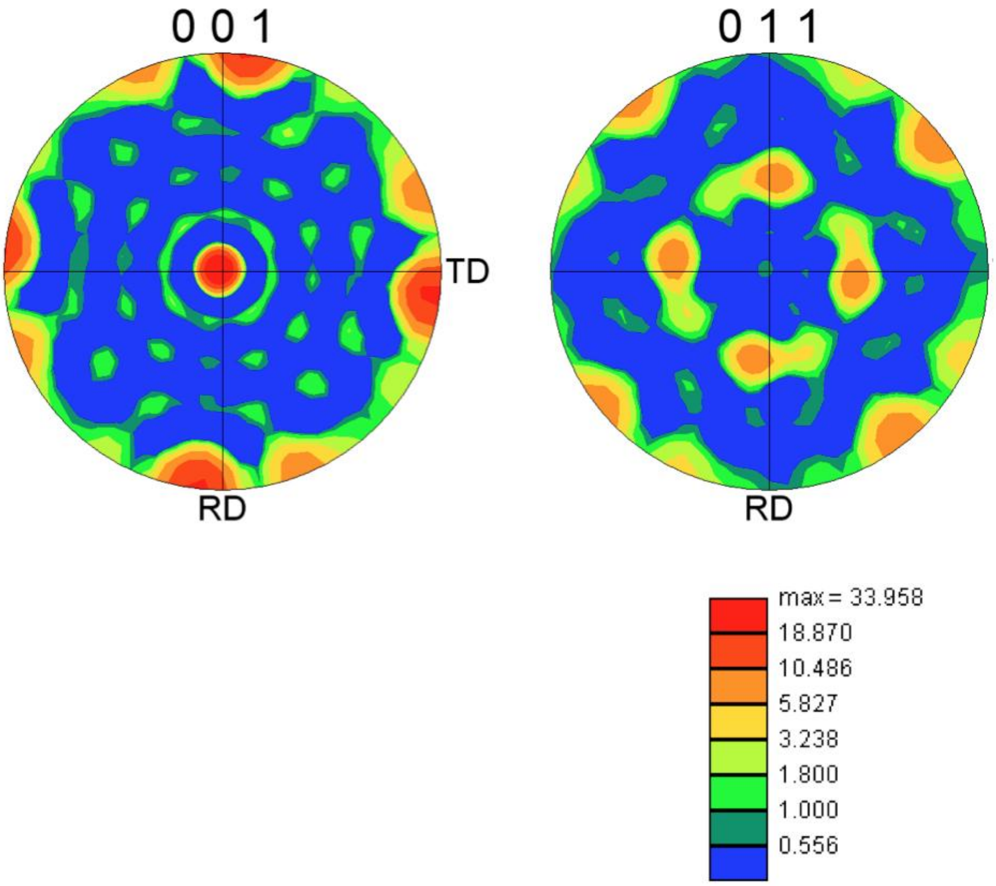

Figure 22. (001) texture in the polycrystalline sample.

After preliminary mapping was performed on the heat-treated samples, several smaller regions were mapped within each sample. Some areas around carbide particles were mapped and several others within the γ-matrix and around grain boundaries. After mechanical deformation, the same areas (those after thermal treatment) were mapped again and the differences studied. More explanation follows in §3.2.

3.2. Mechanical Testing

The polished bend beams prepared from the Mar-M-002 barstock, after initial EBSD mapping, were subjected to mechanical deformation. Initial tests involved bending both single and polycrystalline samples in a three point bend rig. Several areas were picked through the height of the bend beam (including those areas mapped prior to bending) and mapped after monotonic mechanical deformation.

The mechanical loading was performed in two different ways. A few samples (single and polycrystalline) were first subjected to bending under a three-point regime. The loading was conducted on a vertical Denison Mayes test frame, operated by a DMG-Rubicon controller system. The control system was connected to a PC running the DMG-Rubicon software program to allow programmed control and data acquisition.

A schematic of the three- point bend stage used is shown in Figure 23.

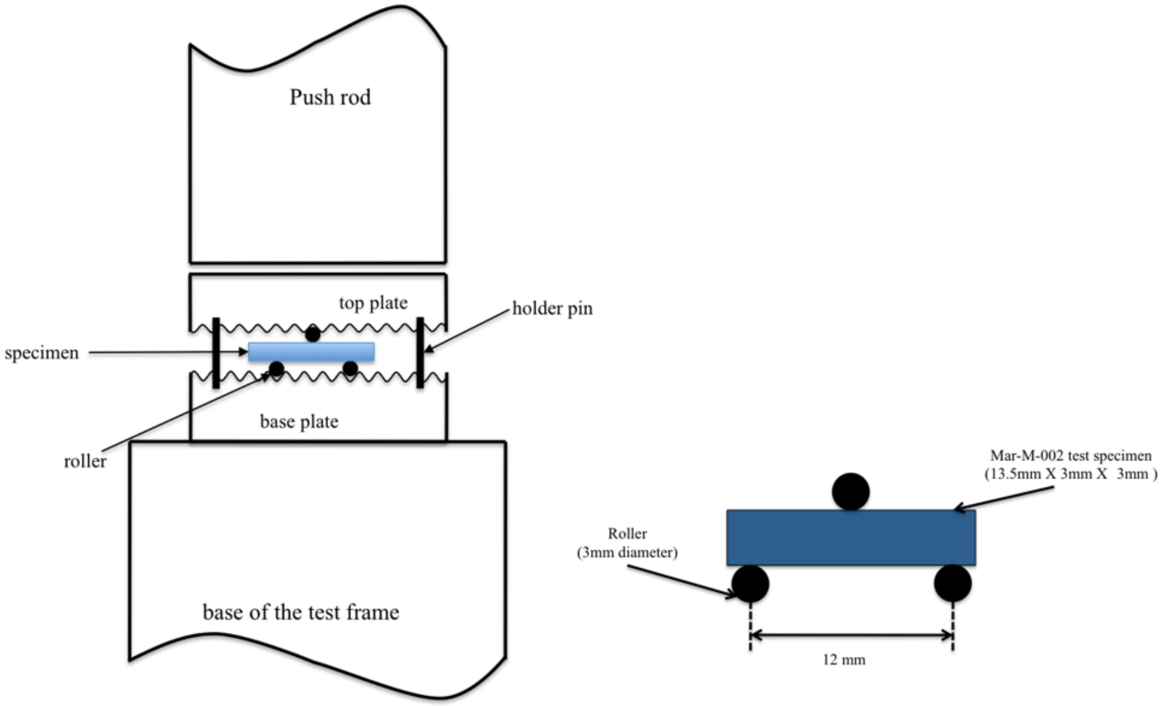

Figure 23.Schematic of the three-point bend stage and test geometry.

Both the plates and the push rod are made from high strength steel, which is harder than the material to be tested. The rollers are steel dowel pins, 3mm in diameter.

A four-point bending geometry was chosen to perform Fatigue testing (cyclic loading). An important point to consider was that since cyclic loading was to be conducted, it would be necessary to be able to reversibly load the test specimens. Load-unload fatigue testing would soon leave the specimens plastically deformed to such an extent that further loading would no longer occur. Four-point loading was chosen because it has the benefit of allowing fully reversed loading of the test specimen without any contact of the specimen within the region of maximum bending stress created between the inner bending points.

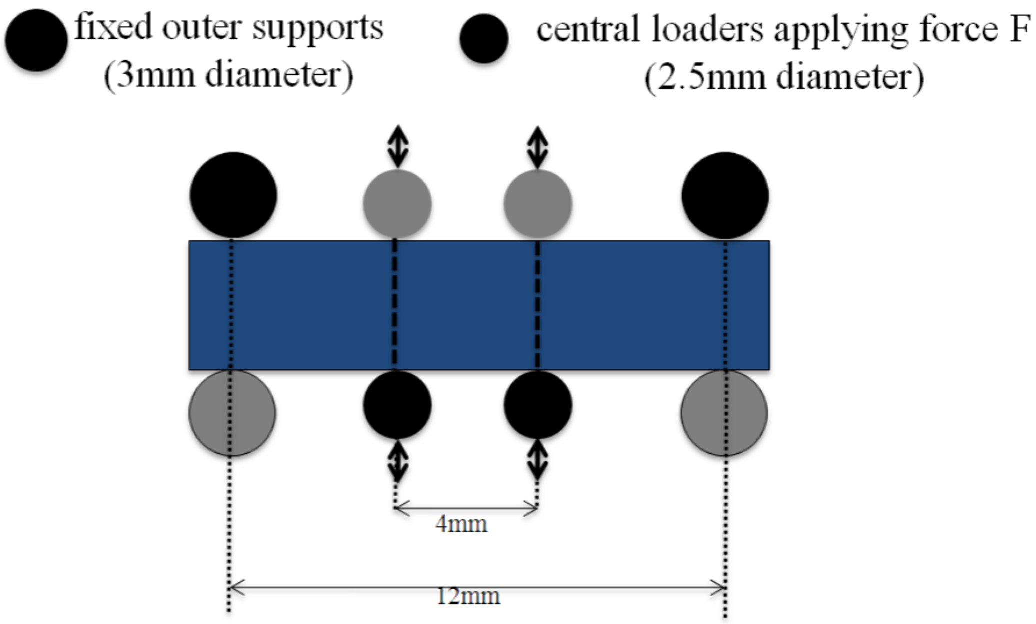

Figure 24.Four-point bend test geometry. Note how the loading supports above and below the test specimen allowing the specimen to be loaded down and pulled back up to achieve reversible loading of the test piece.

The four-point loading was performed on a screw driven Instron load frame, which was controlled by a PC running the Instron Bluehill software package. The four-point loading rig was designed to be able to fit onto the frame and had to be easy to repeatedly setup within the shared loading frame and easy for samples to be installed, accurately aligned and removed at the start and end of a block of loading cycles.

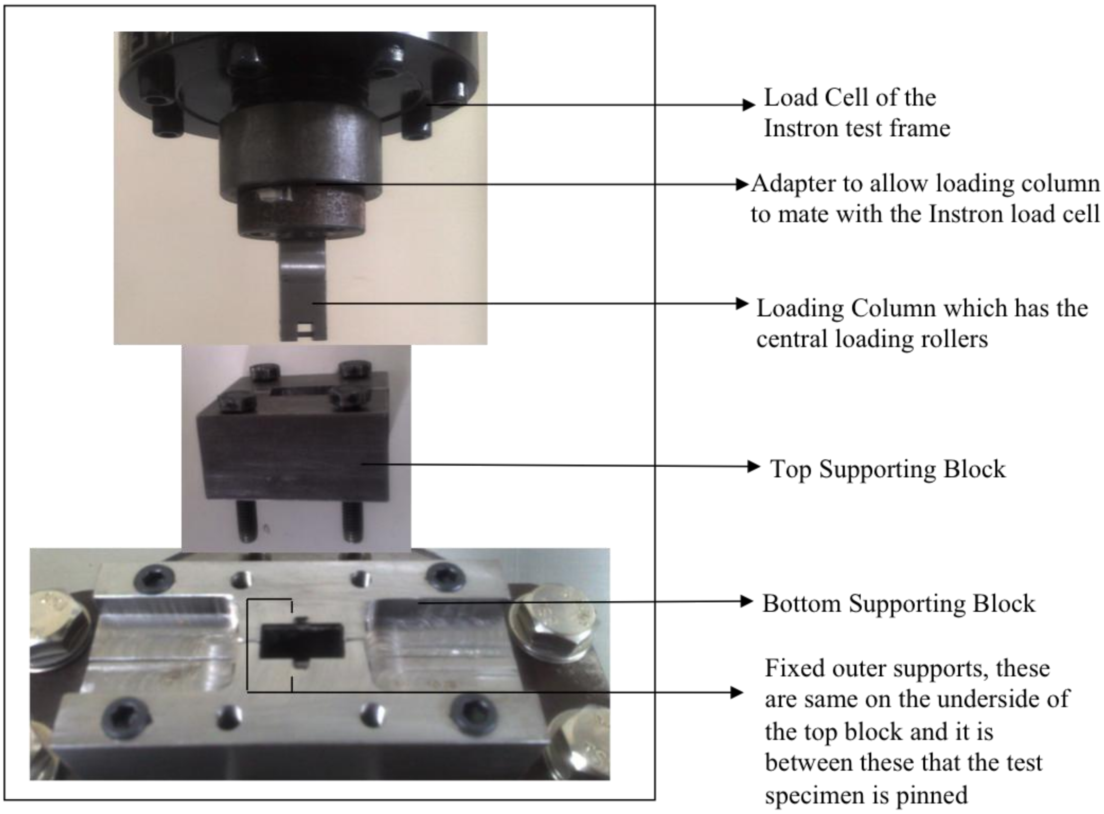

Figure 25. Main parts of the four point loading rig.

Figure 25 shows the three parts of the loading rig, which are brought together to load the test specimen in reversible four point bending. Figure 26 illustrates a cross-sectional view of the setup.

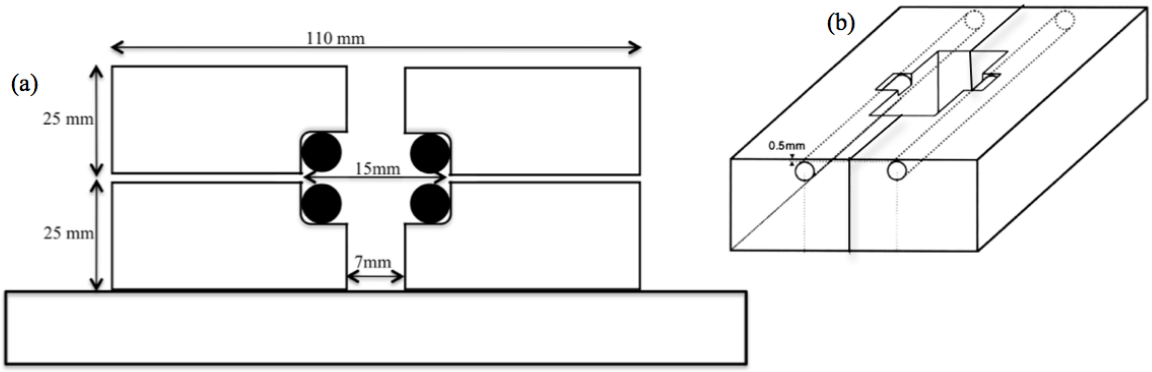

Figure 26. (a)Cross sectional view through the top and bottom block. (b)showing placement of silver steel rods in the bottom supporting block.

3.3. Electron Backscatter Diffraction

Wilkinson's technique[5] relies on offline EBSD pattern analysis using a cross-correlation method. EBSD patterns for offline analysis were recorded using a 1000 X 1000 pixel, peltier cooled charge coupled device (CCD) camera at full resolution on a Schottky emission JEOL-6500 FEG scanning electron microscope (SEM). The scintillator screen was held at its usual position so as to subtend a large capture angle (~70°) at the sample. Typical SEM conditions used were 20 keV beam energy, and a beam current of ~10 nA, for which exposure time was typically a second. Patterns were recorded at full resolution with intensities digitized to 12-bit on hard disk using TSL/EDAX OIM DC 5.3 software for subsequent off-line batch-wise analysis using the strain determination software CrossCourt 3 [89]. All maps were obtained using a 250nm step size, which is well above the spatial resolution of the method. These smaller region maps (around carbide particles and matrix areas) have been phrased henceforth as *high-resolution ebsd maps*.

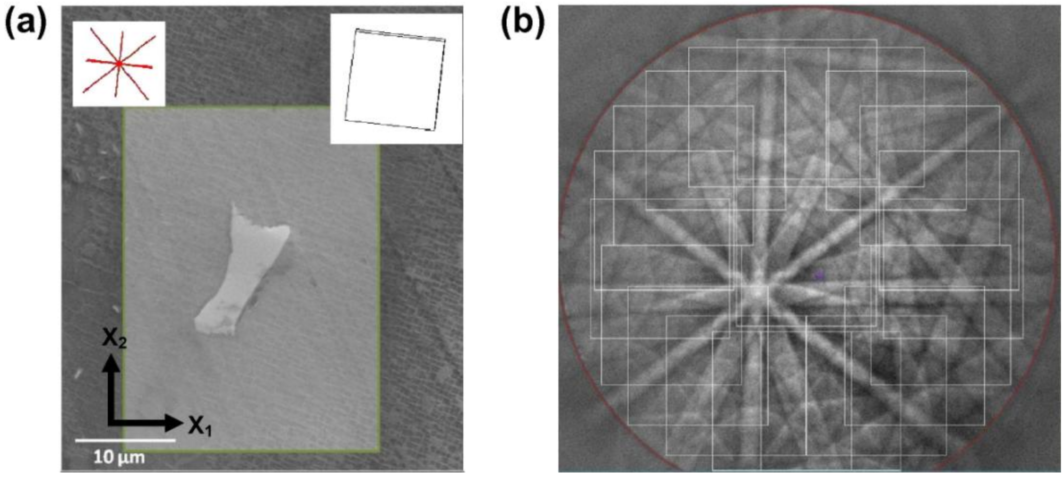

Figure 27. a) Secondary electron image of a carbide particle with insets showing the crystal orientation and the trace of $\langle 110 \rangle$ slip directions in the surface plane of the Ni based matrix. (b) EBSD pattern from the crystal with 20 sub-regions used for cross-correlation analysis marked.

An example of a carbide, the mapped region around it and an example EBSD pattern are shown in Figure 27. This particular carbide is from a single crystal beam sample. The nickel matrix was oriented with its cube axes almost aligned with the axes of the bend beam as is illustrated by the wireframe inset in Figure 27(a), and is described by the Euler angles ϕ_1 = 83.5°, ϕ = 91.5°, ϕ_2 = 0° using Bunge notation[90].

Cooling from high temperatures combined with the difference in thermal expansion coefficients between the matrix and carbides are likely to result in considerable thermal residual strains around the carbides. Several carbides were identified distributed through the height (i.e. position along the x_2 axis) of this beam and high-resolution EBSD maps were obtained around each particle to assess these thermal strains.

Lattice rotations and elastic strain variations within the sample cause small shifts in the positions of zone axes and other features in the EBSD patterns obtained as the electron beam is scanned over the sample. These small pattern shifts are measured using automated image-processing based on cross-correlation analysis and then related to the size and nature of the strains and rotations. The shifts at four or more sub-regions widely dispersed across the EBSD patterns are sufficient to directly calculate eight of the nine degrees of freedom. This last degree of freedom is the hydrostatic dilation or contraction of the lattice and can be recovered by making use of the fact that EBSD measurements come from within a few tens of nanometers of the free surface which must remain traction-free. Setting the stress normal to the free surface to zero ($\sigma_{33} = 0$) allows the three normal strains to be fully separated so that all six terms in the strain tensor and all three terms in the lattice rotation tensor are fully determined.

From the cross-correlation analysis of EBSD patterns, the two remaining terms that come directly are $e_{11} - e_{33}$ and $e_{22} - e_{33}$. With the above mentioned assumption, we have:

$$\sigma_{33} = 0 = C_{33kl}e_{kl} \tag{37}$$

where C_{ijkl} are the single crystal elastic stiffness components in the sample reference frame and the usual summation convention for k and l is implied. The above equation can be re-written as:

$$\sigma_{33} = 0 = C_{3333}e_{33} + C_{3311}e_{11} + C_{3322}e_{22} \tag{38}$$

with C_{3333}= 252 GPa and $C_{3311} = C_{3322}$=158 GPa for Ni. From these sets of equations, the normal strains can now be separated. In this work, the elastic stiffness constants for pure Nickel have been used with the above equation to separate the normal strains terms. The single crystal elastic stiffness components for the current alloy Mar-M-002 have been measured by Kuhn et al.[91] as C_{3333} =258 GPa and $C_{3311} = C_{3322}$=167 GPa. These small variations in the elastic moduli generate only a difference in the measured elastic normal strain values of ~10^{-4} or less, which is almost at the limit of the HR-EBSD technique measurements at this time. Thus, although the elastic constants for pure Nickel have been employed in this study, there will not be any significant differences in the resulting strain maps.

In this work, we have measured the pattern shifts at many more than the minimum four required, and use least squares methods to obtain a "best fit" solution for the displacement gradient tensor. The quality of the pattern shift measurements can be assessed using the height of the peak found in the cross-correlation function. The geometric mean of normalized peak heights for all sub-regions on a given pattern is calculated and used to indicate how well the cross-correlation pattern matching has performed. We then normalize this to unity for an exact match (i.e. auto-correlation) between the test and reference patterns. We also assess the quality of this best fit solution by calculating the mean angular error between the pattern shifts expected from the best fit strain and rotation and the pattern shifts actually measured. The mean angular error gives an assessment of the noise level associated with a given measurement point. Where the measured strains and rotations are larger than the mean angular error there is good confidence in the measurement, but where they are smaller, then they are below the noise limit. An example is shown in Figure 28.

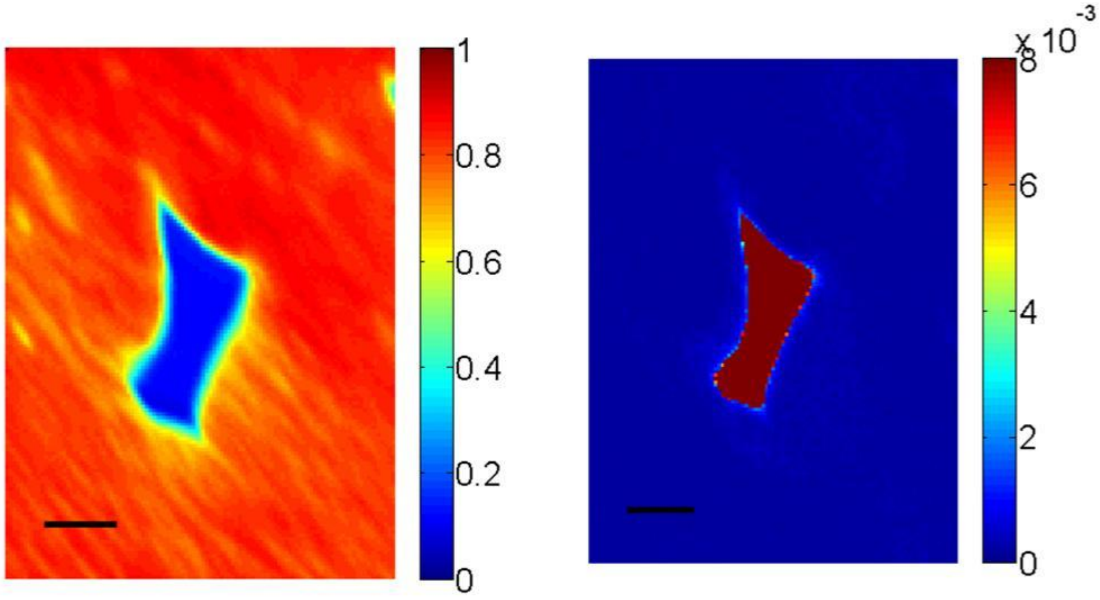

Figure 28.(a) cross-correlation peak height (b) mean angular error (rads) around a carbide particle mapped in Figure 27(a). The scale bars are 5 µm long.

In most of this work, one pattern at a corner of the map from a point farthest away from the carbide particle was selected as the reference pattern and all measurements are made relative to this. Figure 28(a) shows the cross-correlation peak height map indicating a good match (peak height above 0.6) between the test patterns and the reference pattern throughout the Ni matrix, but falling to values of 0.3 and below within the large carbide in the centre of the mapped region. The mean angular error (Figure 28(b)) is seen to be below ~3 × 10^{-4} throughout most of the matrix. Not surprisingly very large values are reported within the carbide regions where the analysis fails due to a completely different EBSD pattern being generated. These maps are used to remove data in which there is low confidence, all pixels for which the peak height is below 0.3 are removed from maps showing the strain and rotation fields.

The assumption of the strain-free reference pattern seems to be reasonable for the case of thermal loading. However, after mechanical deformation that induces plastic deformation through the Ni matrix the reference point will have some unknown strain associated with it, and so absolute strains cannot be determined directly. Absolute strains are obtained by combining the EBSD data with finite element analysis (FEA) simulations. The cross-correlation analysis is run as before using a good quality EBSD pattern as the reference. The average strain within the mapped region is then calculated. A constant strain value is then added to all points within the map so as to bring the average strain to the value given by a FEA of the bent beam.

Lattice curvatures and elastic strain gradients can be determined and used to recover the GND density distribution independently of the FEA simulation (described in §3.4). More discussion about the FEA analysis follows in §3.5.

3.4. GND analysis

Nye [7] gave an elegant geometrical link between lattice curvature and continuous distributions of GNDs described through the dislocation tensor. Nye’s analysis was conducted under the assumption that there is no long-range elastic strain field (i.e. stress field) present in the crystal. Removal of such an assumption introduces elastic strain gradients (i.e. stress gradients) into the formulation in addition to the lattice rotation gradients used by Nye, as has been discussed in detail by Kroner [50].

Several researchers [52], [70], [92-95] have used the lattice curvatures to calculate densities of GNDs within samples, using Hough-based EBSD, which has a lower angular resolution and thus is severely limited for GND analysis. Hough-based EBSD analysis is limited to an angular resolution of ±0.01 to 0.02 rad and results in uncertainty in the axis of misorientation between two points [96] which can be very large when the misorientation angle is small [97]. These uncertainties reduce the accuracy of any lattice curvature measurement and inhibit resolving dislocation structures reliably onto specific slip systems. Wilkinson and Randman [77] measured an uncertainty of δ=8x10^{-3} rads in the orientation measurements around indents in a large grained Fe sample. In their measurements (step size of 200nm), a large uncertainty ($\Delta\rho = \delta/b\lambda$) of ~2x10^{14} m^{-2} was estimated for the GND densities. Thus, the angular noise in Hough-based EBSD puts a lower cap on the GND density measurements at approx. 2×10^{14} GNDs m^{-2}).

Pantleon [70] has shown that five terms in Nye’s dislocation tensor can be established directly from the EBSD measurements, and that the difference between two other terms can also be calculated and used as a further constraint on the GND solution. Pantleon [70] applied his analysis to GND storage within a cold-rolled Al polycrystal and demonstrated that an improved lower bound solution can be obtained when all six constraints are used.

Nye's dislocation tensor $\boldsymbol{\alpha}$ is defined by

$$\boldsymbol{B} = \iint_{\boldsymbol{S}} \boldsymbol{\alpha}\, \boldsymbol{ds} \tag{39}$$

where $\boldsymbol{B}$ is the net Burger's vector of dislocation lines across a closed area.

The dislocation tensor can also be found directly in terms of the elastic distortion field (or the displacement gradient tensor) $\boldsymbol{\beta}$ through

$$\boldsymbol{\alpha} = \boldsymbol{curl}(\boldsymbol{\beta}^{\boldsymbol{e}}) \tag{40}$$

where $\boldsymbol{\beta}^{\boldsymbol{e}}$ is the elastic part of the displacement gradient tensor. It must be noted that $\boldsymbol{\beta}$, $\boldsymbol{\beta}^{\boldsymbol{e}}$ and $\boldsymbol{\beta}^{\boldsymbol{p}}$ are analogous to $\boldsymbol{F}$, $\boldsymbol{F}^{\boldsymbol{e}}$ and $\boldsymbol{F}^{\boldsymbol{p}}$ as described in §2.3, which was given in a different notation that is more common in the mechanics literature.

Writing this explicitly in terms of derivatives of elastic strain and rotation fields gives

$$\boldsymbol{\alpha} = \begin{pmatrix} \dfrac{\partial w_{12}}{\partial x_3} - \dfrac{\partial w_{13}}{\partial x_2} & \dfrac{\partial w_{13}}{\partial x_1} & \dfrac{\partial w_{21}}{\partial x_1} \\ \dfrac{\partial w_{32}}{\partial x_2} & \dfrac{\partial w_{23}}{\partial x_2} - \dfrac{\partial w_{21}}{\partial x_2} & \dfrac{\partial w_{21}}{\partial x_2} \\ \dfrac{\partial w_{32}}{\partial x_3} & \dfrac{\partial w_{13}}{\partial x_3} & \dfrac{\partial w_{31}}{\partial x_2} - \dfrac{\partial w_{32}}{\partial x_1} \end{pmatrix} \tag{41}$$

$$+\begin{pmatrix} \frac{\partial \varepsilon_{12}}{\partial x_3}-\frac{\partial \varepsilon_{13}}{\partial x_2} & \frac{\partial \varepsilon_{13}}{\partial x_1}-\frac{\partial \varepsilon_{11}}{\partial x_3} & \frac{\partial \varepsilon_{11}}{\partial x_2}-\frac{\partial \varepsilon_{12}}{\partial x_1} \\ \frac{\partial \varepsilon_{22}}{\partial x_3}-\frac{\partial \varepsilon_{23}}{\partial x_2} & \frac{\partial \varepsilon_{23}}{\partial x_1}-\frac{\partial \varepsilon_{21}}{\partial x_3} & \frac{\partial \varepsilon_{21}}{\partial x_2}-\frac{\partial \varepsilon_{22}}{\partial x_1} \\ \frac{\partial \varepsilon_{32}}{\partial x_3}-\frac{\partial \varepsilon_{33}}{\partial x_2} & \frac{\partial \varepsilon_{33}}{\partial x_1}-\frac{\partial \varepsilon_{31}}{\partial x_3} & \frac{\partial \varepsilon_{31}}{\partial x_2}-\frac{\partial \varepsilon_{32}}{\partial x_1} \end{pmatrix}$$

Using high angular resolution EBSD, six of the nine lattice curvature components can be calculated from the changes in lattice rotation across the sample surface $\left({\partial w_{ij}}/{\partial x_k}\ with\ K = 1\ or\ 2\right)$; the remaining three $\left({\partial w_{ij}}/{\partial x_3}\right)$ concern variation of the lattice rotations with depth below the surface, which cannot be obtained by a surface technique like EBSD alone.

Since the information along the depth is absent, the terms containing ${\partial}/{\partial x_3}$ are unknown, leaving only three of the nine elements of the dislocation tensor fully determined. In many instances that Wilkinson et. al. [54], [55], [73], [74], [77] have looked at experimentally, the rotation gradients are considerably larger than the elastic strain gradients, in which case we can either neglect the elastic strain gradients entirely or include those terms that are available experimentally and put the other terms to zero $\left({\partial \varepsilon_{ij}}/{\partial x_3} = 0\right)$. In such a case, it would be unlikely that those, which cannot be measured, are sufficiently large as to contribute to the curvatures significantly.

Using these six components it is possible to calculate a lower bound solution to the density of GNDs using Nye's dislocation analysis [7]. The elements in Nye's dislocation tensor are related to the densities ρ_s of different dislocation types through

$$\boldsymbol{\alpha}_{ij} = \sum_{s=1}^{s_{max}} \rho_s \, \boldsymbol{b}_i^s \, \boldsymbol{t}_j^s \tag{42}$$

where $\boldsymbol{b}^s$ is the Burgers vector, and $\boldsymbol{t}^s$ the unit line direction of the s^{th} dislocation type. Nye originally considered a set of nine dislocations with line directions and Burgers vectors constrained to be along the cube axes of the crystal, in what Sun et al.[53] refer to as the simple cubic (sc) deconstruction. In this case, an unambiguous link between the nine elements of $\boldsymbol{\alpha}$ and the densities of the different types of dislocation can be established. In our case, this does not realistically reflect the crystallographic geometry of possible dislocation types in the *fcc* Ni crystal; however, such an approach may provide a lower bound estimate of the overall dislocation density.

To include the crystallography of the *fcc* Ni sample, we can assume that movement and storage of dislocations support the deformation with $\frac{a}{2}\langle 110\rangle$ Burgers vector slipping on $\{111\}$ planes. We further assume that the dislocations are represented by either pure edge or pure screw types. This results in 18 distinct dislocation types (ignoring positive and negative senses) including twelve edge types (with $\langle 211\rangle$ line directions) and six screw types (with $\langle 111\rangle$ line directions). The dislocations and their line properties, in the same order as listed by Arsenlis and Parks [98] are given in Table

1.In this table, $\boldsymbol{s}$ represents the slip direction, $\boldsymbol{n}$ the slip-plane normal direction and $\boldsymbol{t}$ the unit-line direction.

Table 1.The dislocation basis used to describe the dislocation state in fcc crystals

Density	***t***	***s***	***n***
ρ_1	$\frac{1}{\sqrt{6}}[\bar{1}\bar{1}2]$	$\frac{1}{\sqrt{2}}[\bar{1}10]$	$\frac{1}{\sqrt{3}}[111]$
ρ_2	$\frac{1}{\sqrt{6}}[\bar{1}2\bar{1}]$	$\frac{1}{\sqrt{2}}[10\bar{1}]$	$\frac{1}{\sqrt{3}}[111]$
ρ_3	$\frac{1}{\sqrt{6}}[2\bar{1}\bar{1}]$	$\frac{1}{\sqrt{2}}[0\bar{1}1]$	$\frac{1}{\sqrt{3}}[111]$
ρ_4	$\frac{1}{\sqrt{6}}[\bar{1}1\bar{2}]$	$\frac{1}{\sqrt{2}}[\bar{1}\bar{1}0]$	$\frac{1}{\sqrt{3}}[1\bar{1}\bar{1}]$
ρ_5	$\frac{1}{\sqrt{6}}[\bar{1}\bar{2}1]$	$\frac{1}{\sqrt{2}}[101]$	$\frac{1}{\sqrt{3}}[1\bar{1}\bar{1}]$
ρ_6	$\frac{1}{\sqrt{6}}[211]$	$\frac{1}{\sqrt{2}}[01\bar{1}]$	$\frac{1}{\sqrt{3}}[1\bar{1}\bar{1}]$
ρ_7	$\frac{1}{\sqrt{6}}[1\bar{1}\bar{2}]$	$\frac{1}{\sqrt{2}}[110]$	$\frac{1}{\sqrt{3}}[\bar{1}1\bar{1}]$
ρ_8	$\frac{1}{\sqrt{6}}[121]$	$\frac{1}{\sqrt{2}}[\bar{1}01]$	$\frac{1}{\sqrt{3}}[\bar{1}1\bar{1}]$
ρ_9	$\frac{1}{\sqrt{6}}[\bar{2}\bar{1}1]$	$\frac{1}{\sqrt{2}}[0\bar{1}\bar{1}]$	$\frac{1}{\sqrt{3}}[\bar{1}1\bar{1}]$
ρ_{10}	$\frac{1}{\sqrt{6}}[112]$	$\frac{1}{\sqrt{2}}[1\bar{1}0]$	$\frac{1}{\sqrt{3}}[\bar{1}\bar{1}1]$
ρ_{11}	$\frac{1}{\sqrt{6}}[1\bar{2}\bar{1}]$	$\frac{1}{\sqrt{2}}[\bar{1}0\bar{1}]$	$\frac{1}{\sqrt{3}}[\bar{1}\bar{1}1]$
ρ_{12}	$\frac{1}{\sqrt{6}}[\bar{2}1\bar{1}]$	$\frac{1}{\sqrt{2}}[011]$	$\frac{1}{\sqrt{3}}[\bar{1}\bar{1}1]$
ρ_{13}	$\frac{1}{\sqrt{2}}[110]$	$\frac{1}{\sqrt{2}}[110]$	$\frac{1}{\sqrt{3}}[1\bar{1}\bar{1}]$ *or* $\frac{1}{\sqrt{3}}[\bar{1}1\bar{1}]$
ρ_{14}	$\frac{1}{\sqrt{2}}[101]$	$\frac{1}{\sqrt{2}}[101]$	$\frac{1}{\sqrt{3}}[1\bar{1}\bar{1}]$ *or* $\frac{1}{\sqrt{3}}[\bar{1}\bar{1}1]$
ρ_{15}	$\frac{1}{\sqrt{2}}[011]$	$\frac{1}{\sqrt{2}}[011]$	$\frac{1}{\sqrt{3}}[\bar{1}1\bar{1}]$ *or* $\frac{1}{\sqrt{3}}[\bar{1}\bar{1}1]$
ρ_{16}	$\frac{1}{\sqrt{2}}[\bar{1}10]$	$\frac{1}{\sqrt{2}}[\bar{1}10]$	$\frac{1}{\sqrt{3}}[111]$ *or* $\frac{1}{\sqrt{3}}[\bar{1}\bar{1}1]$
ρ_{17}	$\frac{1}{\sqrt{2}}[10\bar{1}]$	$\frac{1}{\sqrt{2}}[10\bar{1}]$	$\frac{1}{\sqrt{3}}[111]$ *or* $\frac{1}{\sqrt{3}}[\bar{1}1\bar{1}]$
ρ_{18}	$\frac{1}{\sqrt{2}}[0\bar{1}1]$	$\frac{1}{\sqrt{2}}[0\bar{1}1]$	$\frac{1}{\sqrt{3}}[111]$ *or* $\frac{1}{\sqrt{3}}[1\bar{1}\bar{1}]$

The lattice curvatures are linked to the GND densities by the equation

$$\boldsymbol{K} = (\boldsymbol{A_1}, \boldsymbol{A_2}, \boldsymbol{A_3} \cdots \boldsymbol{A_s})(\boldsymbol{\rho}) \tag{43}$$

where the column vector $\boldsymbol{K}$ consists of the six curvature components and $\boldsymbol{A}_s$ contains terms from the tensor product of the Burger's vector and line direction of the s^{th} dislocation type.

As this equation is under-determined, with potentially 18 unknown GND densities described by only six curvatures, we have used a standard linear programming algorithm (in MatLab) to find a lower bound solution of the GND densities for each individual slip system, at each point in the EBSD maps. Rather than using a computationally faster L^2 optimisation routine, (which has no real physical argument leading us to expect a solution which minimises the sum of squares of dislocation densities) that some researchers have been using [93], we favour the use of a computationally more intensive L^1 routine, wherein we seek to minimise the total dislocation line energy. The MatLab code used for GND analysis was obtained from previous studies within the group, but modified for the *fcc* crystal system.

All our dislocations have the same magnitude Burgers vector, so the only difference in their energies is generated by the ratio of energies for edge and screw dislocations

$$\frac{E_{edge}}{E_{screw}} = \frac{1}{1-v} \tag{44}$$

This ratio is ~1.5, for a typical metal($\upsilon = 0.3$). In order to produce a stable solution, we 'unfold' the dislocation types to consider positive and negative types separately (by considering oppositely signed Burger's vectors in constructing $\boldsymbol{A}_s$). This results in 18×2 slip systems in total. We can now constrain each GND density to be zero or greater. Finally, we choose a solution, which may not be unique, but does support the lattice curvatures, and also generates the lowest possible total GND line energy. Finally, we can fold each positive and negative pair of dislocation types back together (one will definitely be zero) and then calculate the total GND density by summing up (the absolute values of) all the GND densities for each slip system used. In consequence, the set of GNDs that support the measured lattice curvatures while minimizing the dislocation line energy may not always be unique and there could be many other combinations of GNDs that can generate the same lattice curvatures. We do not consider all the possible sets of GNDs, but confine only to one particular set of solutions.

3.5. Modelling

Modelling has been carried out in two phases. The first set of modelling involves a standard set of functions defined in a commercial finite element package ABAQUS [99], in order to estimate the elastic, plastic and total strain at a point in the mechanically deformed beams as a result of mechanical deformation. As already discussed at the end of §3.2, after mechanical deformation, plastic deformation is induced throughout the Ni matrix. The reference point for cross-correlation based analysis will have some unknown elastic strain associated with it, and so absolute strains cannot be determined directly. Absolute strains have been obtained by combining the EBSD data with finite element analysis (FEA) simulations, which give the average residual elastic strains in the mapped region.

Within the finite element method, the body under consideration is discretized into a finite number of elements and nodes. The elements are interconnected at the exterior nodes, and altogether they cover the entire domain as accurately as possible. The finite element model representing the body therefore contains a finite number of degrees of freedom (defined for the nodes) and the implication is that the requirement for equilibrium cannot be satisfied exactly at every point in the continuum. Instead, within the finite element technique, a weak formulation of equilibrium is used in which global equilibrium for the body as a whole is imposed even though this does not necessarily ensure point-wise equilibrium. Nodes have nodal (vector) displacements or degrees of freedom, which may include translations, rotations, and/or higher order derivatives of displacements (for some special applications). When the nodes displace, they will ‘drag’ the elements along in a certain manner dictated by the element formulation. In other words, displacements of any points in the element are interpolated from the nodal displacements.

The FEA simulation was undertaken using ABAQUS software [99]. A three-dimensional finite element mesh with about 8500 eight-node brick elements (incompatible modes) was used for the discretization of the beam. No constraints were applied to elements making up the beam other than through contact with the rollers, thus all the surfaces of the beam are essentially in plane stress-like conditions. The three rollers (four rollers in case of four point bending simulations) were modelled to stay rigid throughout the simulation. The bottom rollers were fixed in all directions. Loading from the top roller was controlled to give a load–unload cycle, whose maximum displacement was fixed in accordance with the experiment. The contact surfaces between the beam and the rollers were defined to have a friction coefficient of 0.5. The (isotropic) elastic constants used for the beam are as follows: Young's modulus E of 207 GPa and Poisson's ratio ν of 0.28, as supplied by Rolls-Royce plc. Conventional continuum plasticity was used to model the deformation in this case with the yield strength of 810 MPa and a plastic tangent modulus of 75 MPa.

The second set of modelling involves setting up the finite element crystal plasticity model to simulate the GND density distribution. The code was not developed within the group, but within Prof. Dunne's group in the Department of Engineering. All the simulations were carried out within Prof. Dunne's group. The following procedure describes the implementation of a simple single-crystal deformation into ABAQUS finite element code. For an improved understanding of the implementation on a model with multiple slip systems, readers are referred to [51].

A finite element analysis in ABAQUS is defined by an input file, which contain model data such as coordinates, nodes, elements, materials, initial conditions, etc. and history data to define the analysis type, loading, output requests, etc.

A UMAT is a user subroutine in ABAQUS to define the mechanical properties of the material. Variables passed in to the UMAT from ABAQUS include the time increment, and the deformation gradient at the beginning and end of the time increment. In addition, the material Jacobian matrix (or the effective tangent stiffness – a matrix that describes the stiffness response of a system to small changes in configuration) and the solution-dependent state variables need to be updated to their values at the end of the time increment in the UMAT.

The solution-dependent state variable array is setup to contain the slip directions and slip plane normals, resolved shear stresses, angles between the slip direction and the loading axis in all the slip systems and the effective plastic strain. Suppose $\boldsymbol{F}^{\boldsymbol{t}}$ and $\boldsymbol{F}^{\boldsymbol{t}+\boldsymbol{\Delta t}}$ are the deformation gradients provided by ABAQUS at the beginning and end of the time increment, the UMAT subroutine must calculate the Cauchy stress at the end of the time increment. The UMAT has been coded with the equations shown as a flowchart in Figure 29.

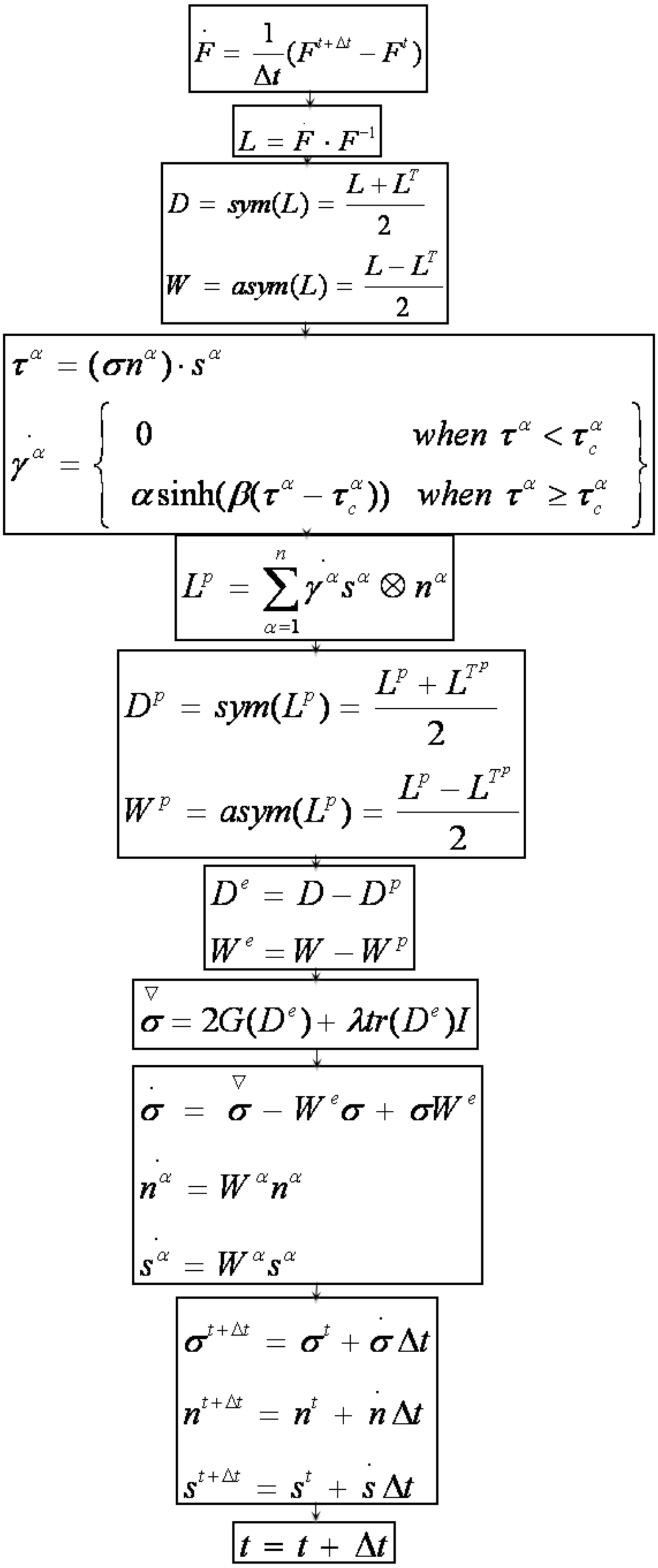

$$\dot{F} = \frac{1}{\Delta t}(F^{t+\Delta t} - F^{t})$$

$$L = \dot{F} \cdot F^{-1}$$

$$D = sym(L) = \frac{L + L^{T}}{2}$$

$$W = asym(L) = \frac{L - L^{T}}{2}$$

$$\tau^{\alpha} = (\sigma n^{\alpha}) \cdot s^{\alpha}$$

$$\dot{\gamma}^{\alpha} = \left\{ \begin{array}{ll} 0 & when\ \tau^{\alpha} < \tau_{c}^{\alpha} \\ \alpha \sinh(\beta(\tau^{\alpha} - \tau_{c}^{\alpha})) & when\ \tau^{\alpha} \geq \tau_{c}^{\alpha} \end{array} \right\}$$

$$L^{p} = \sum_{\alpha=1}^{n} \dot{\gamma}^{\alpha} s^{\alpha} \otimes n^{\alpha}$$

$$D^{p} = sym(L^{p}) = \frac{L^{p} + L^{T^{p}}}{2}$$

$$W^{p} = asym(L^{p}) = \frac{L^{p} - L^{T^{p}}}{2}$$

$$D^{e} = D - D^{p}$$

$$W^{e} = W - W^{p}$$

$$\overset{\triangledown}{\sigma} = 2G(D^{e}) + \lambda tr(D^{e})I$$

$$\dot{\sigma} = \overset{\triangledown}{\sigma} - W^{e}\sigma + \sigma W^{e}$$

$$\dot{n}^{\alpha} = W^{\alpha} n^{\alpha}$$

$$\dot{s}^{\alpha} = W^{\alpha} s^{\alpha}$$

$$\sigma^{t+\Delta t} = \sigma^{t} + \dot{\sigma}\Delta t$$

$$n^{t+\Delta t} = n^{t} + \dot{n}\Delta t$$

$$s^{t+\Delta t} = s^{t} + \dot{s}\Delta t$$

$$t = t + \Delta t$$

Figure 29. Flowchart showing calculation procedure in the UMAT (redrawn from** [51]**)

Liang et al. [51] have developed this technique by defining twenty-node, three dimensional finite elements to obtain essential strain gradient information at all the integration points at the same time. A user defined finite element (UEL) is defined based on which the deformation gradients at integration points can be computed to obtain the geometrically necessary dislocation densities. In the absence of the development of GNDs, the material response is simple elastic-perfectly plastic with no hardening. However, as local plastic strain gradients develop to accommodate slip/lattice rotations, GNDs become necessary to accommodate the gradient. The development of GNDs leads to an increase in the number of pinning sites for mobile SSDs or equivalently, a decrease in the activation volume (or pinning distance). This results in hardening, and accordingly this model shows lengthscale dependency, in the flow stress.

For the calculation of geometrically necessary dislocation densities, the plastic strain gradient is required. However, within ABAQUS only information relating to a single element integration point is available at a given time for a standard element. In order to overcome this difficulty, a non-local approach was developed by defining twenty-node, three-dimensional finite elements to obtain the essential gradients information of all the integration points at the same time. Subsequently, a user defined finite element (UEL) was developed in which the deformation gradients at all integration points are computed and can be used to obtain the geometrically necessary dislocation densities through the deformation gradients. Following that, the residual force, which is needed in the subroutine UEL to be provided to ABAQUS, was given according to the principle of virtual work [51]. A user-defined element (UEL) was developed in order to determine the plastic strain gradients, as described elsewhere by Dunne et al [8] and for a detailed description of the large deformation formulation, the readers are directed to [51]. Only a simple sketch of the model is given below.

We have already seen (from [38]) that the overall plastic velocity gradient is made up of contributions from all active slip systems and is given in terms of the slip directions s^{α} and slip plane normal n^{α} corresponding to the α^{th} slip system by

$$L^P = \sum_{\alpha=1}^{k} \dot{\gamma}^{\alpha} s^{\alpha} \otimes n^{\alpha} \tag{45}$$

and the slip rate $\dot{\gamma}^{\alpha}$ the model follows is given by [8] :

$$\dot{\gamma}^{\alpha} = \rho_{SSD}^{m} b^2 \upsilon \exp\left(\frac{\Delta F}{kT}\right) \sinh\left(\frac{(\tau^{\alpha} - \tau_c)\Delta V}{kT}\right) \tag{46}$$

in which ρ_{SSD}^{m} is the density of mobile statistically stored dislocations, ΔF is the Helmholtz free energy barrier which needs to be exceeded in order for a pinned statistically stored dislocation to be released, b is the magnitude of the Burgers vector, υ is the frequency of dislocation jumps (successful or otherwise), k is the Boltzmann constant, T is the absolute temperature. τ^{α} is the resolved shear stress, τ_c is the critical resolved shear stress (CRSS), and ΔV the activation volume associated with dislocation glide, which is taken to be $\Delta V = \lambda b^2$, where λ is the pinning distance. Here it is assumed that the predominant pinning mechanism is that caused by the development of GNDs and immobile statistically stored dislocations (SSDs). The pinning distance is therefore related to the density of GNDs ρ_{GND} and the density of immobile SSDs ρ_{SSD}^{im} and in the absence of more detailed information, is assumed to be given by:

$$\lambda = \frac{1}{\sqrt{\rho_{SSD}^{im} + \rho_{GND}}} \tag{47}$$

The densities of mobile and immobile SSDs are taken to be the same and initially assigned the value 1×10^{10} m^{-2}. For reasons of simplicity, and retaining a physical basis, Liang et al. [51], [54] have chosen not to evolve the SSD density directly with subsequent deformation, but do allow density to change as a result of the GND evolution based on a geometrically determined relation.

Liang et al. [51] have made quantitative comparisons of their predictions with Sun et. al.'s [53] experiments on deformed Aluminum bicrystals, indents in Iron[77], and with Britton et al.'s indentation in CP-Titanium[54]. We shall use this crystal plasticity modelling data to make direct comparisons with experimentally measured strains, lattice rotations and GND densities after deformation in the Nickel-based superalloy MAR-M-002.

4. Thermally Induced Strain

This chapter will present some high-resolution EBSD maps around some carbide particles on a sample just after heat treatment. As a result of heat treatment (described in §3.1) on these samples and cooling from such high temperatures combined with the difference in thermal expansion co-efficients between the matrix and the carbide results in a considerable thermal residual strain around the carbides. Several carbides were identified through the height of these beams and EBSD maps were obtained around each particle to assess these thermal strains. Later, comparisons have been made with some preliminary results from the Finite element crystal plasticity model as already stated. Each section is followed by a short discussion on the results.

4.1. Experiments and simulations

The heat treatment was repeated for a second time on some samples, so as to achieve an enlarged grain structure. Preliminary EBSD results showed a single crystal matrix, which was not unexpected due to massive grain growth from the double heat treatment. The Nickel matrix was oriented with its cube axis almost aligned with the axis of the bend beam as illustrated by the wireframe inset in Figure 30, and is described by the Euler angles φ_1= 83.5º, Φ = 91.5º and φ_2= 0º in Bunge's notation. This particular example has already been shown previously in §3.3.

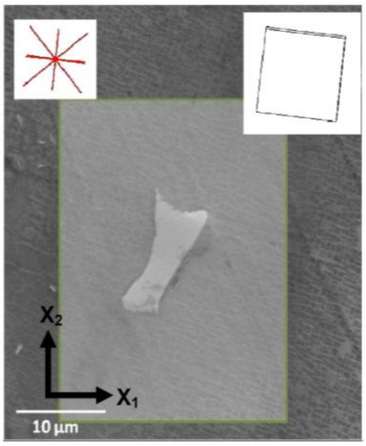

Figure 30. Secondary electron image of a carbide particle with insets showing the crystal orientation and the trace of $\langle 110\rangle$ slip directions in the surface plane of the Ni based matrix

On this single crystal sample (beam sample – ‘S4’), fifteen carbide particles have been identified through the height of beam (along the x_2 axis in Figure 30) and using high-resolution EBSD, these areas have been mapped. Nine areas away from carbides have also been mapped, in order to measure any residual strain within the matrix (from the heat treatment).

After measurements on the single crystal sample, another beam (sample – ‘P1’), which was subjected to only a single cycle of heat treatment was chosen and similar maps made. On this sample, six areas were mapped around carbide particles and three areas away from the particles.

With the help of the EBSD orientation data, the finite element crystal plasticity model has been employed by Prof. Fionn Dunne's group and a simulation of the heat treatment carried out and results have been compared alongside the experimental measurements.

Shown in the following section are some EBSD maps from two of the carbides to illustrate the results obtained (one from sample S4 and another from sample P1). It has already been discussed in §3.3 that Wilkinson's technique requires a strain-free reference pattern for pattern shift measurements. In this work, one pattern at a corner of the map (towards the top left) from a point farthest away from the carbide particle was selected as a reference pattern and all measurements are made relative to this. The assumption of the strain-free reference pattern is very reasonable for the case of thermal loading.

4.2. EBSD results

Figure 31 shows maps of data quality parameters in the area shown in Figure 30. As already specified, the Nickel matrix was oriented with its cube axis almost aligned with the axis of the bend beam as illustrated by the wireframe inset in Figure 30, and is described by the Euler angles φ_1= 83.5º, Φ = 91.5º and φ_2= 0º.

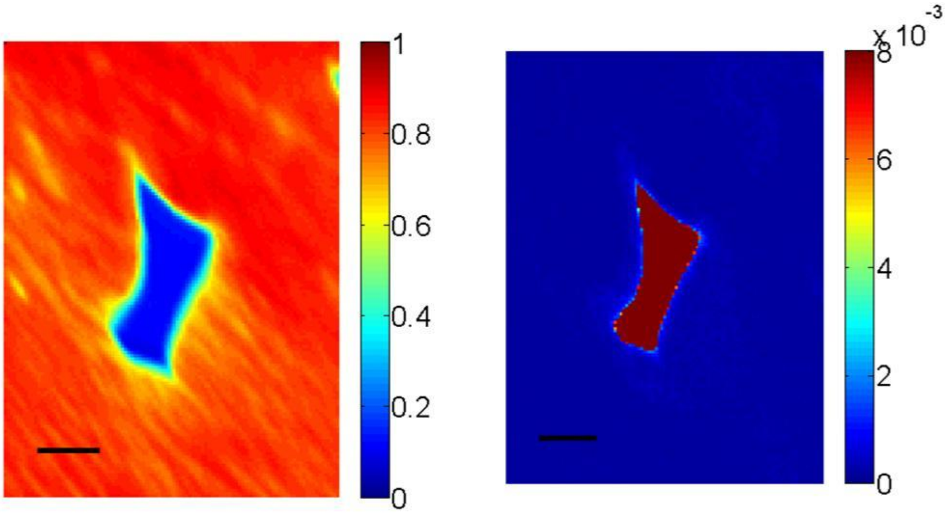

Figure 31. (a) cross-correlation peak height (b) mean angular error (rads) around a carbide particle mapped in Figure 30. The scale bars are 5 µm long and the step size is 0.25 µm per pixel.

Figure 31(a) shows the cross-correlation peak height map indicating a good match (peak height above 0.9) between the test patterns and the reference pattern throughout the Ni matrix, but falling to values of 0.3 and below within the large carbide in the centre of the mapped region. The mean angular error (Figure 31(b)) is seen to be below 3 x 10^{-4} throughout most of the matrix. Not surprisingly very large values are reported within the carbide regions where the analysis fails due to a completely different EBSD pattern being generated. All pixels for which the peak height was below 0.3 were removed from maps showing the strain and rotation fields.

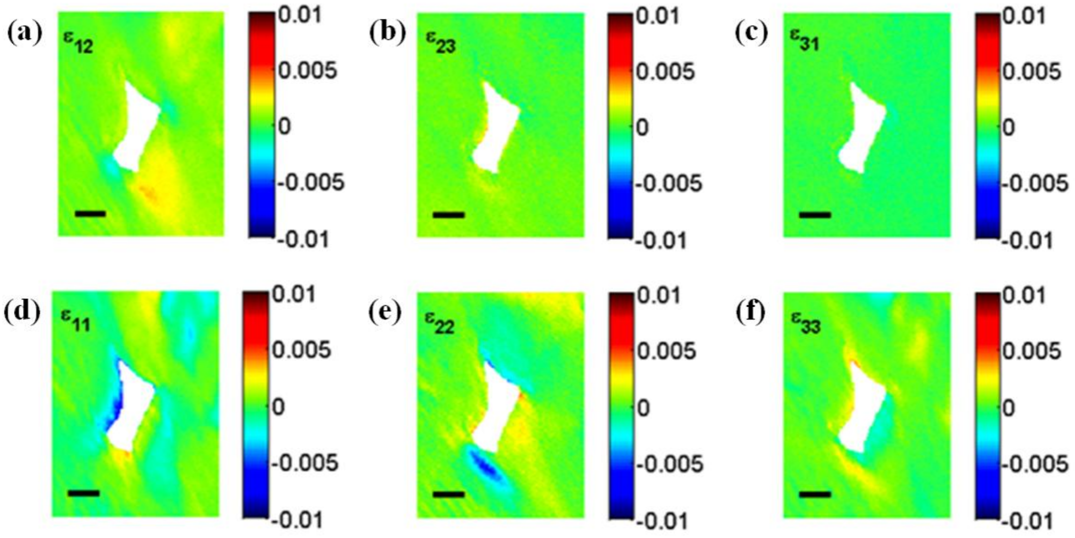

Figure 32. Thermally induced strains near selected carbide. The scale bars are 5 µm long and the step size is 0.25 µm per pixel.

The elastic strain fields are shown in Figure 32(a-f). The normal strain ε_{11} along the horizontal x_1 axis is mostly compressive to the left and right of the carbide and tensile above and below it (Figure 32(d)), while the ε_{22} strain along the vertical x_2 axis shows strains with the opposite sign (Figure 32(e)). This is in agreement with a first order prediction based on tensile hoop and compressive radial strains near a cylindrical particle in a contracting matrix. Due to the complex shape of the carbide, the thermally induced strain fields are not very symmetric. The most significant in-plane shear strains (Figure 32(a)) occur near the bottom right hand corner of the carbide where the rotation fields show least variation, indicating less plastic relaxation of the thermal mismatch. The two out of plane shear strains remain close to zero (Figure 32(b) and (c)). This is not unexpected, since we expect the corresponding stresses σ_{23} and σ_{31} to be zero in fulfillment of the traction-free surface condition. In separating the normal strains, we have made use of the traction-free surface condition but have only constrained the normal stress σ_{33} is forced to zero. No constraint was imposed for the shear stresses (σ_{13} and σ_{23}), so the near zero value of the corresponding shear strains (ε_{13} and ε_{23}) in Figure 32 give confidence that the measured strain tensor is correct.

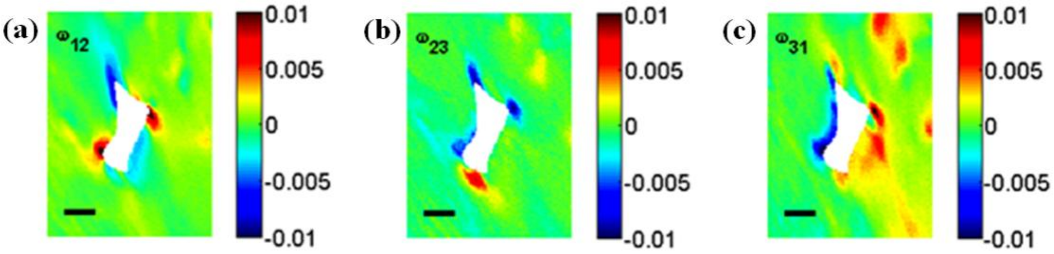

Figure 33. Lattice rotations due to thermally induced strains near the selected carbide. The scale bars are 5 μm long and the step size is 0.25 μm per pixel.

The in-plane lattice rotations ω_{12} about the x_3 are shown in Figure 33(a), which are of a significantly larger magnitude than the elastic strains, but are limited to quite local regions near the carbide–matrix interface. Rotations about the two in-plane axes (x_1 axis in Figure 33(b), and x_2 axis in Figure 33(c)) also exhibit similar magnitudes. The direction of the rotation changes from top to bottom for rotation about the horizontal axis and from left to right for rotation about the vertical axis. These ω_{23} and ω_{31} rotations are possibly due to the relaxation of compressive stress originally along the carbide axis while in the sample interior but brought to zero by sectioning.

In the single crystal sample S4, thermal residual strains were mapped at 15 carbides and results were broadly consistent with those described above. There was considerable variation in the size and shape of the individual carbide particles and this leads to subtle changes in the detailed strain and rotation distributions.

Another map of elastic strains and lattice rotations for the polycrystal sample P1 is shown below. Figure 34 shows an optical image of the carbide particle being referred to and the insets show the crystal wireframe and the trace of $\langle 110 \rangle$ slip directions in the Nickel matrix. The wireframe inset is described by the Euler angles φ_1= 93º, Φ = 90.5º and φ_2= 25º respectively.

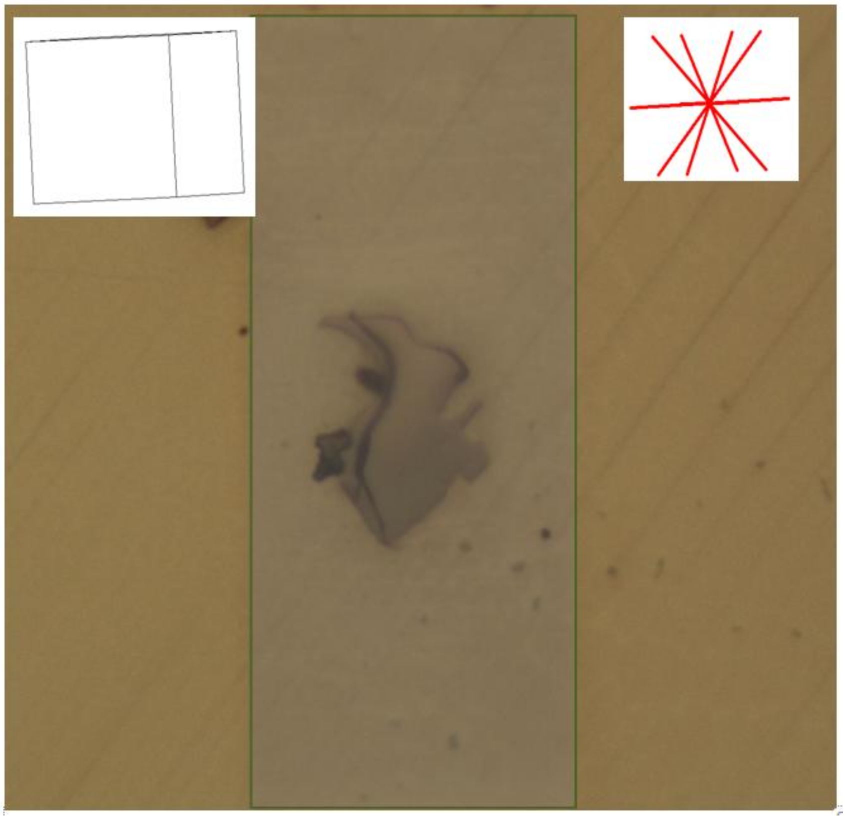

Figure 34. Optical micrograph of a carbide particle (from sample 'P1') with insets showing the crystal orientation and the trace of $\langle 110 \rangle$ slip directions in the surface plane of the Ni based matrix

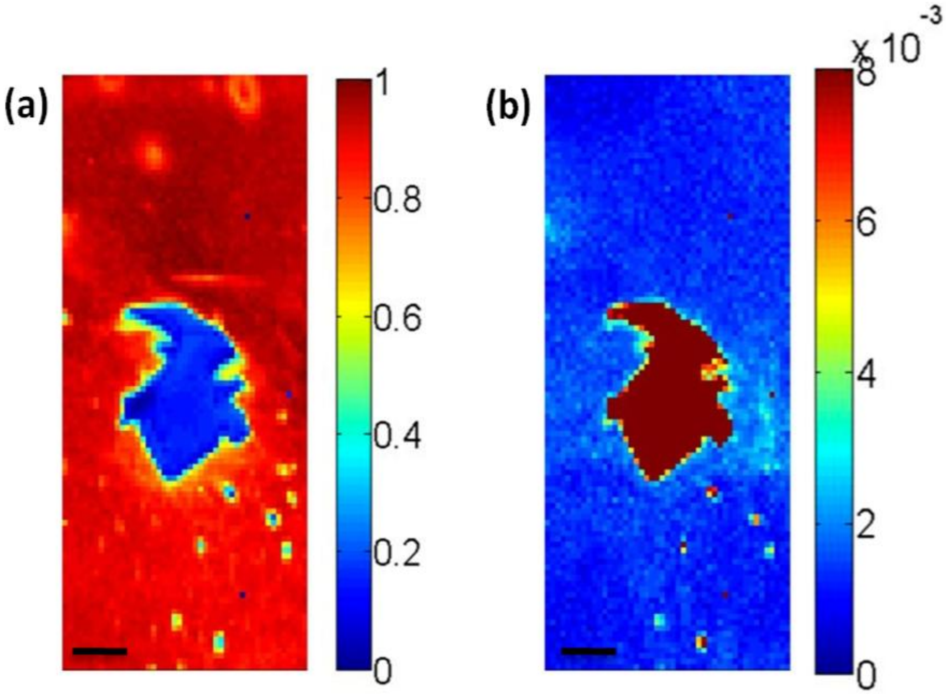

Figure 35. (a) cross-correlation peak height (b) mean angular error (rads) around a carbide particle mapped in Figure 34. The scale bars are 5 µm long and the step size is 0.25 µm per pixel.

Across the nickel-based matrix the peak height remains high (close to one), showing that patterns were successfully matched to the reference pattern. The mean angular error is seen to be below ~4×10^{-4} throughout most of the matrix, while the completely different pattern obtained from within the carbide results is a very poor match to the reference and so the peak height also falls towards zero. In addition to the large (approximately 15 µm) carbide in the centre of the map, other smaller carbides are present mainly in the bottom right-hand corner of the mapped region. All pixels for which the peak height was below 0.4 were removed from maps showing the strain and rotation fields. The elastic strain fields are shown in Figure 36.

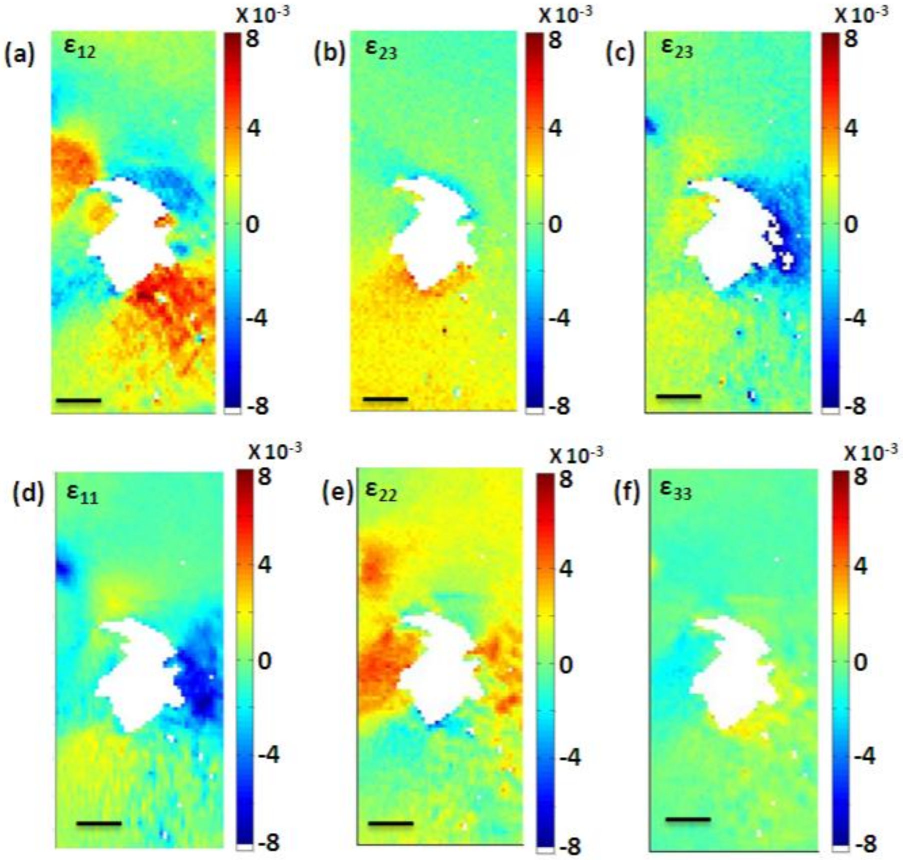

Figure 36. Thermally induced elastic strain variations near the selected carbide from Figure 34. The scale bars are 5 µm long and the step size is 0.25 µm per pixel.

The thermally induced strain field around the large central carbide particle is far from symmetric. This is presumably due to the complex particle shape and the distribution of fines carbides around it both in and below the section plane. The normal strain ε_{11} along the horizontal x_1 axis is compressive to the left and right of the carbide and tensile above and below it (Figure 36(d)), while the ε_{22} strain along the vertical axis shows strains with the opposite sign (Figure 36(e)). This is broadly consistent with the expected radial compressive strain and tensile hoop strain that is expected to develop during cooling as the matrix contracts more strongly than the carbide it surrounds. As stated already, the imposition of the traction free surface condition (σ_{33}=0) and the fact that the two in-plane normal strains are of similar magnitude but opposite sign means that the out-of-plane normal strains ε_{33} are not as large as the two in-plane normal strains (Figure 36(f)). The in-plane shear strain ε_{12} distribution shows maximum positive and negative values at ~+45° and ~-45° around the carbide (Figure 36(a)). These shears can be represented by two perpendicular normal strains of the same magnitude but opposite sign aligned along radial and hoop directions (i.e. at ±45° to the shear) and so are in accord with radial compression and tangential tension. The two out of plane shear strains remain low (Figure 36(b) and (c)). Again, this is an expected (though not imposed) result as the corresponding out of plane shear stresses should be zero to comply with the traction free surface condition, and elastic anisotropy only provides slight coupling of the shear strains to other components of the stress tensor.

The lattice rotation fields are shown in Figure 37 (note this has a different colour scale than for the strains in Figure 36).

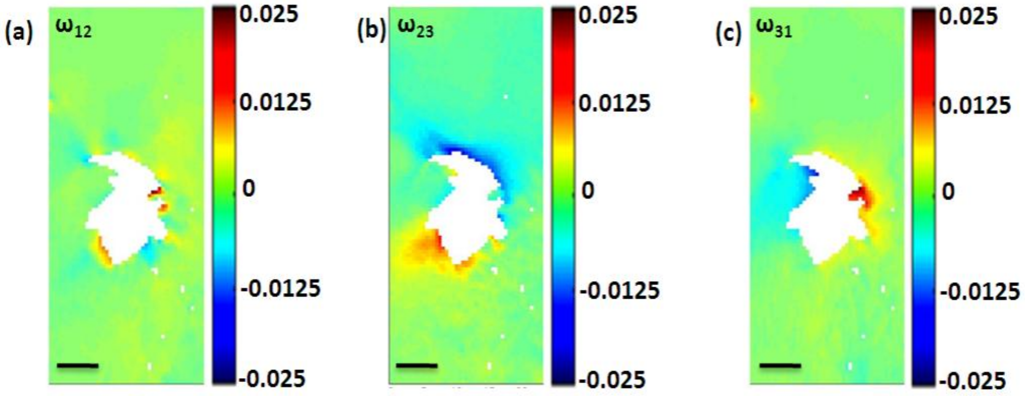

Figure 37. Thermally induced lattice rotations near the selected carbide. The scale bars are 5 µm long and the step size is 0.25 µm per pixel.

The ω_{12} lattice rotations about the x_3 are shown in Figure 37(a), where large magnitude but quite localised peaks are seen at the edge of the carbide. Rotations about the two in-plane axes (x_1 axis in Figure 37(b), and x_2 axis in Figure 37(c)) also exhibit large magnitudes and extend over larger regions than for the in-plane rotation. The sign of the rotation changes from top to bottom for rotation about the horizontal axis and from left to right for rotation about the vertical axis. These ω_{23} and ω_{31} rotations are thought to result from relaxation of the compressive stress originally along the carbide axis in the bulk but brought to zero by sectioning to form a free surface.

Some components of the elastic strain are seen to be relatively large, of order 10^{-3}, and this coupled with the larger but localized in-plane rotations suggests that the thermal loading may have been sufficient to cause some limited plastic flow within the matrix close to the carbide. This is broadly consistent with an effective temperature drop of several hundred degrees and a difference in the thermal expansion coefficients of order 10^{-5} K^{-1} between the metallic matrix and ceramic particle, leading to strains ($\Delta\alpha\Delta T$) of the order of 10^{-3}.

4.2.1. GND density measurement

As already shown, using high angular resolution EBSD, three lattice rotation components can be measured. As an outcome, six of the nine rotation gradients, required to form the Nye’s dislocation tensor [7], [50] can be calculated. The remaining three concern variation of the lattice rotations with depth below the surface and are inaccessible. Using these six components it is possible to calculate a lower bound solution to the density of geometrically necessary dislocation densities (GNDs).

The Nye tensor $\boldsymbol{\alpha}$ involves gradients of the lattice rotation and elastic strain fields. This can be calculated even though the absolute strain values are not known (In this case it is a reasonable assumption that the reference pattern, far away from the carbide corresponds to a region of almost zero strain). From the three measured lattice rotations (ω_{12}, ω_{23} and ω_{31}), we can calculate six of the nine lattice curvatures $\left(\frac{\partial\omega_{12}}{\partial x_1}, \frac{\partial\omega_{12}}{\partial x_2}, \frac{\partial\omega_{23}}{\partial x_1}, \frac{\partial\omega_{23}}{\partial x_2}, \frac{\partial\omega_{31}}{\partial x_1} \text{ and } \frac{\partial\omega_{31}}{\partial x_2}\right)$. The various rotation and strain gradients contributing to the components of the Nye tensor have been shown in this chapter already. It is clear that the dominant term is the rotation gradient. We have found a similar and obvious dominance of the rotation gradients for all the other carbides mapped in these samples. This allows us to neglect the elastic strain gradient terms so that we can calculate five components of $\boldsymbol{\alpha}$ directly and also $\boldsymbol{\alpha}_{11} - \boldsymbol{\alpha}_{22}$. This provides 6 rotation gradients which must be satisfied by the 18 different GND types (in *fcc*).

Had we been forced to include the strain gradients as well, then only 3 components of $\boldsymbol{\alpha}$ could be calculated which leads to much less constraint on the solution for the GND densities and results in considerably lower values for the overall GND density. A similar effect has been reported by Pantleon [70] for analysis of conventional Hough-based EBSD data from a deformed Al polycrystal.

Maps showing the total GND densities in the examples from samples ‘S4’ and ‘P1’ are shown in Figure 38.

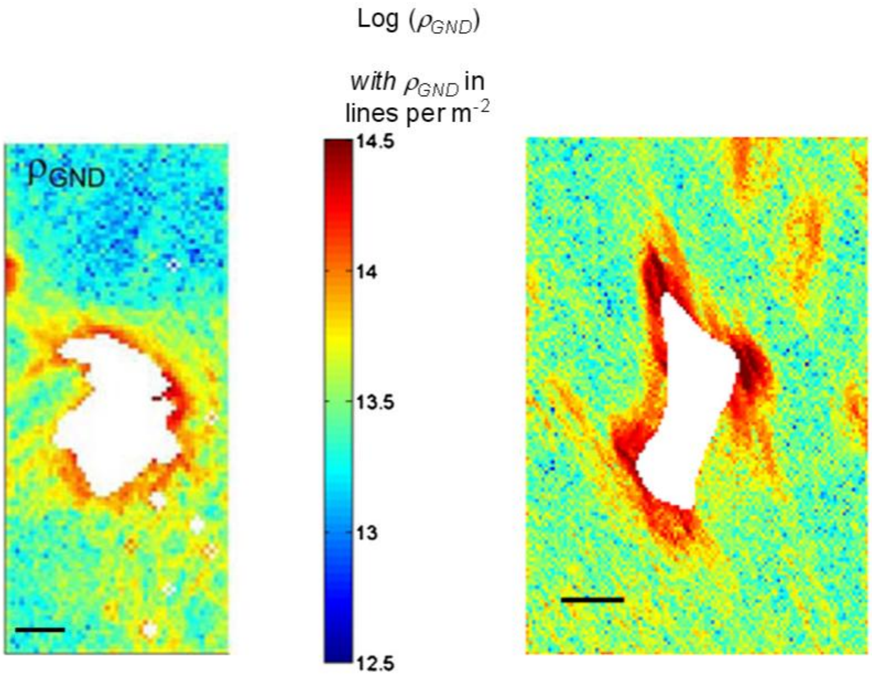

Figure 38. Total density of GNDs as a result of thermally induced strain. (a)around a carbide from the polycrystal sample ‘P1’ (b) around a carbide from the single crystal sample ‘S4’. The scale bars are 5 µm long and the step size is 0.25 µm per pixel.

The GND density within 1 to 2 µm of these carbides is significantly raised in Figure 38 indicating a small thermally induced plastic zone. Within this plastic zone the GND density is ~2×10^{14} m^{-2}.

The cross-correlation-based analysis of EBSD patterns provides a means of probing dislocation arrangements at the mesoscopic and microscopic length scales and thus forms an important bridge between analysis of individual defects in the transmission electron microscopy (TEM) and volume-averaged densities available through X-ray and neutron probes. It is predominantly at these length scales that many important phenomena occur during plastic deformation, as a result of complex interactions between dislocations and microstructural features.

The relatively complex shape of the carbide particles clearly has a significant effect on the detailed distribution of thermally induced elastic strain and hence stress in the matrix, as is evident from the variation from carbide to carbide. However, it is clear that in the matrix close to the carbide some components of the elastic strain are relatively large (of order 10^{-3}). This is broadly consistent with an effective temperature drop of several hundred degrees and a difference in the thermal expansion coefficients of order 10^{-5} K^{-1} between the metallic matrix and ceramic particle, leading to strains ($\Delta\alpha\Delta T$) of the order of 10^{-3}.

The magnitude of the elastic strains together with the larger magnitude but more localized nature of the lattice rotations suggests that the thermal loading may have been sufficient to cause some plastic flow. This is evident in the GND density maps as regions of elevated GND content surrounding the particles. The thermally induced GND densities determined in this work also tend to be increased around the sharper corners of the carbides. The high GND densities found in the Ni-based system examined here presumably result from the high temperature of the ageing treatment and slow diffusional creep rates, which lead to high misfit strains that have to be accommodated.

From the sample ‘S4’, 15 areas have been mapped around these carbide particles of various sizes and GND density estimated. The following plot summarises the average GND density around these particles (within about 2µm of the particle) collectively from this sample.

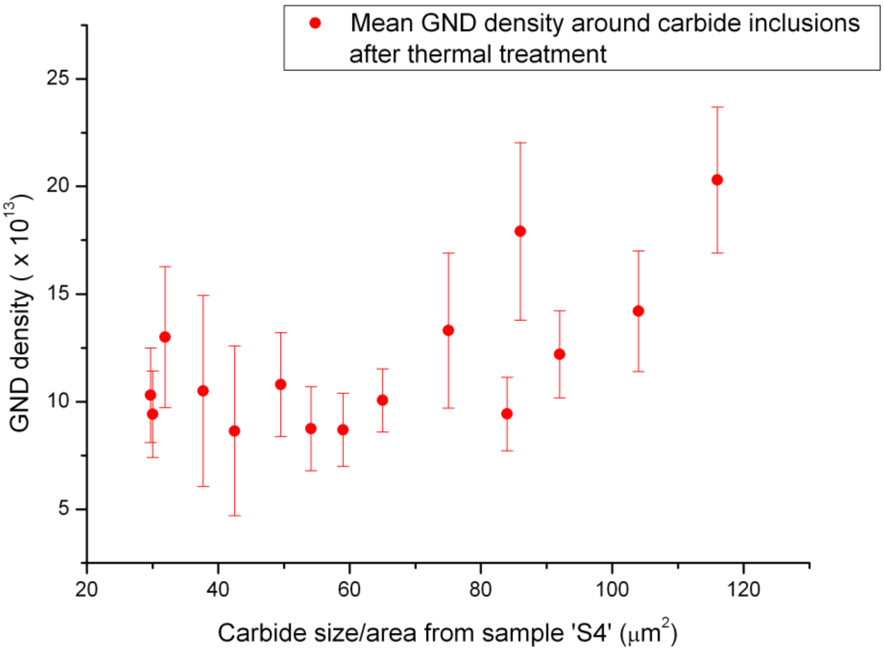

Figure 39. GND density around carbide particles in the sample ‘S4’ after thermal treatment.

In conclusion, the average GND density around the carbide particles varies between ~1×10^{14} to 2×10^{14} m^{-2} after the thermal treatment. The error bars in the graph show one standard deviation from the mean GND density value. It can also be seen that there is clearly a larger GND density around very large carbides structures.

Perhaps a more meaningful interpretation of the GND density measurements may be represented by an estimate of the plastic zone size. Most of the total GND density maps (also shown in the chapter and the next) show a clearly demarked plastic zone around the carbide particle, arising due to the thermal misfit strains. This plastic zone size representation may sometimes provide more significant comparison than the absolute and average GND data values.

To estimate the plastic zone size, we choose a minimum cut off value for GND density and measure the area around the carbide particle where the GND density is at least this value. In most of the maps obtained from the sample 'S4' (including Figure 38(b)), the GND data within this demarked plastic zone is above 10^{14} m^{-2}. We choose such a limiting value based on the abrupt increase in GND density from the surrounding matrix to the regions around the carbide. Thus, by this definition, the plastic zone size is the area around the carbide particle where the GND density increases suddenly to a pretty large value. The outer boundary of this plastic zone is distinguished by a sudden increase in the GND density from that in the surrounding matrix and the inner boundary by the edge of the carbide particle. The following plot shows an approximate measure of the plastic zone size around carbide particles after thermal treatment.

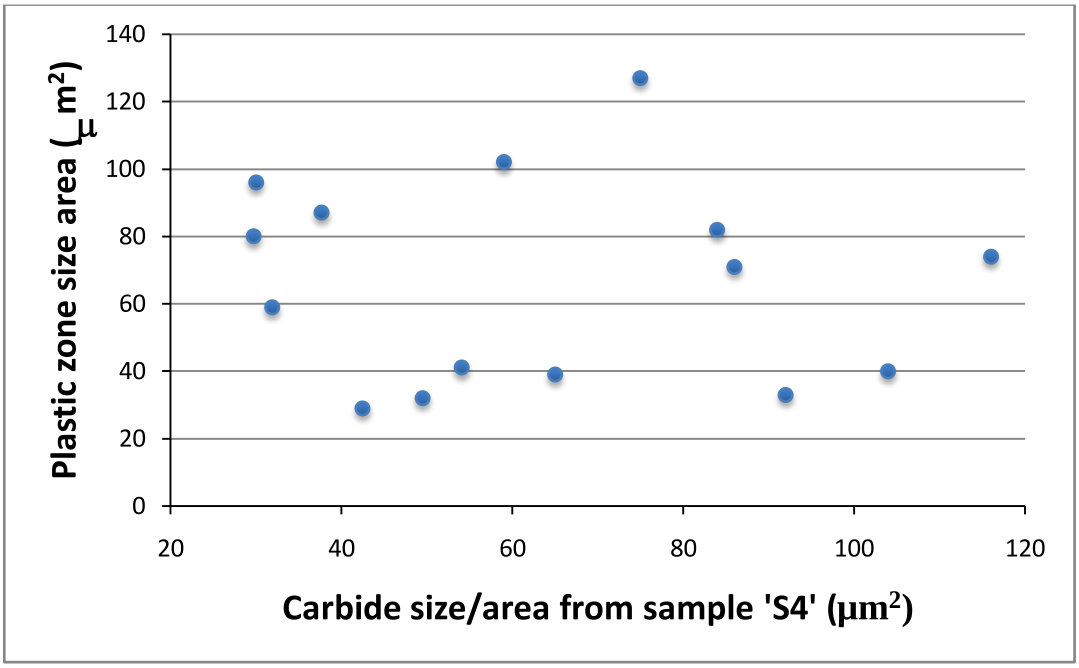

Figure 40. Plastic zone size area around carbide particles from sample 'S4'.

It is interesting to note that some of the smaller sized carbides (where the mean GND density is only about 10^{14} m^{-2}) have a larger plastic zone size. It is also to be noted that in some cases the GND density data and the plastic zone sizes are influenced by the change in shape of carbide particles below the matrix surface or having an axis inclined to the surface normal.

The lattice strains (elastic), rotation and GND density measurements tend to be incredibly useful when describing what goes on during deformation processes. Comparison of these measurements with crystal plasticity finite element simulations is still ongoing. A few initial results have been discussed in the following section.

4.3. Comparison with crystal plasticity Finite Element model

Liang's model (as described in §3.5) has been further extended by Kiwanuka et al. from Prof. Fionn Dunne's group to include thermal deformation as a result of heat treatment. With about 16,200 elements of type C3D20R (3-dimentional quadratic, 20 reduced-integration elements) and an area equal to that from experimental measurement, with a unit element thickness has been subjected to modelling. Current ongoing work involves the same carbide particle from sample 'S4' (as shown in Figure 30), subjected to the similar heat treatment cycle from the experiment.

A newer python implementation developed by Prof. Dunne's group allows plotting a mesh (both 2D and 3D extrusions) by reading crystal orientations from experimental EBSD data (consisting of phase data and Bunge Euler angles). This allows plotting similar areas to those measured experimentally. The following simulations have been performed after plotting areas from experimental EBSD data in combination with Prof. Dunne's crystal plasticity FE code, extended for thermal deformation problems (by Mr. Robert Kiwanuka). Some comparisons have been made below with preliminary simulation results. Shown in Figure 41 below is a plot of the total accumulated plastic strain as a result of the heat treatment within the Nickel matrix. The plot shows a maximum accumulated strain of about 4% and more in some areas in the vicinity of the carbide particle.

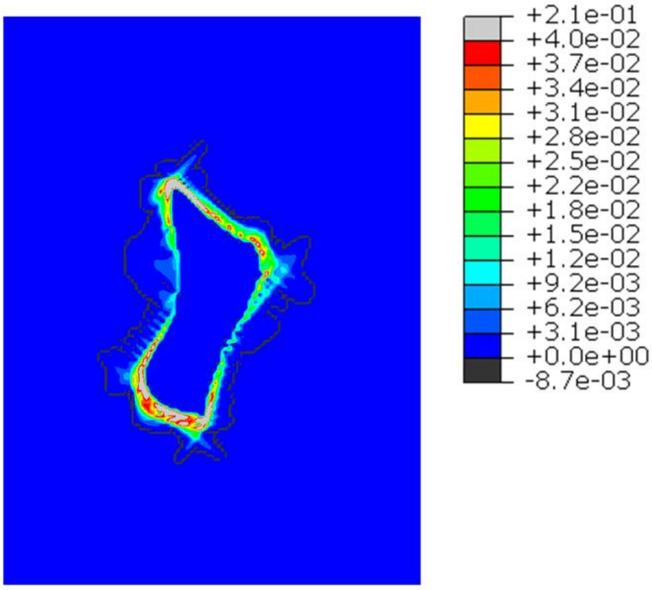

Figure 41. The predicted accumulated plastic strains resulting from the heat treatment which develops within the Ni single crystal matrix.

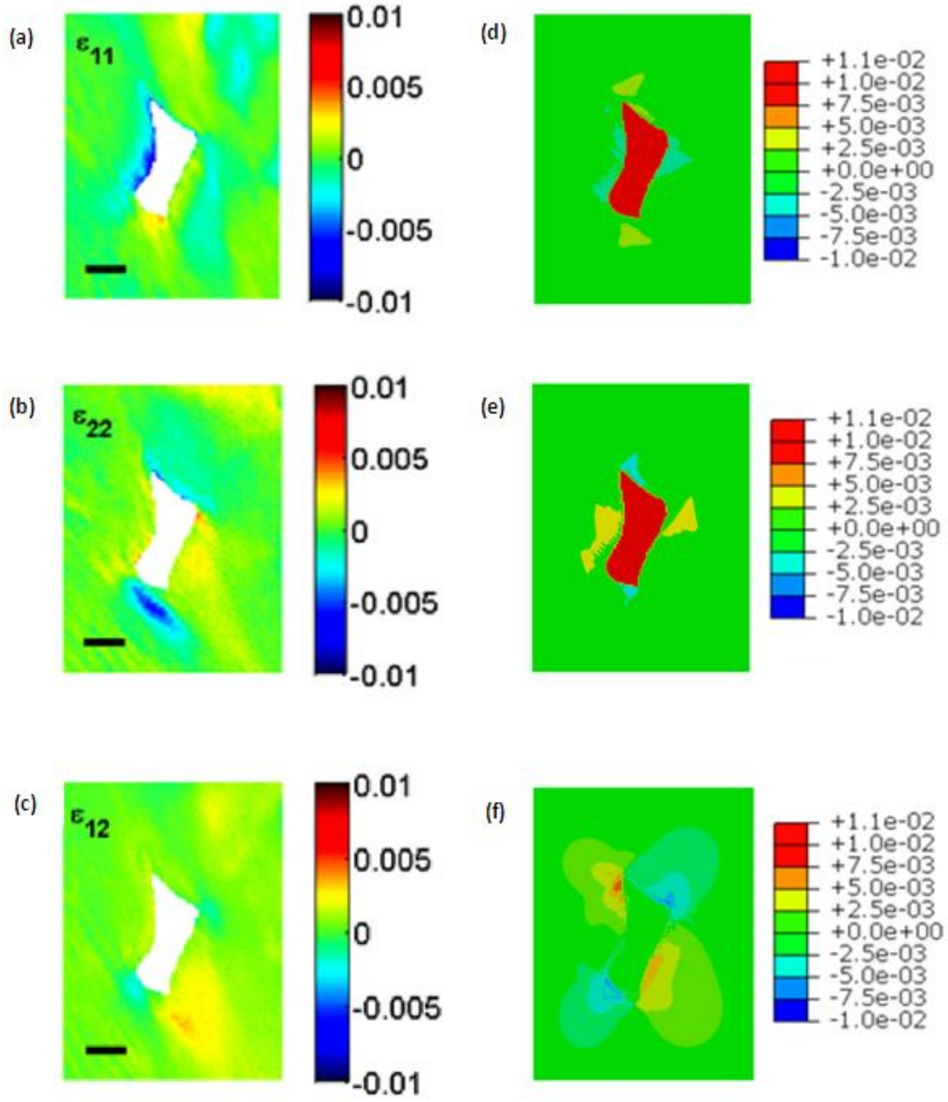

Figure 42. Field plots of components (as indicated) of elastic strains (a) - (c) experimentally determined and (d) - (f) those predicted from the crystal plasticity finite element model. The range is the same for both figures.

The crystal plasticity finite element simulation elastic strain plots from Figure 42 have been plotted by subtracting the thermal and plastic strain components from the total strain calculated. At the current stage of the simulation, the elastic strain components correspond pretty well to the experimentally determined elastic strain components (surely in the compressive/tensile mode of the strain, if not perfectly in magnitude). The in-plane rotation is compared in Figure 43.

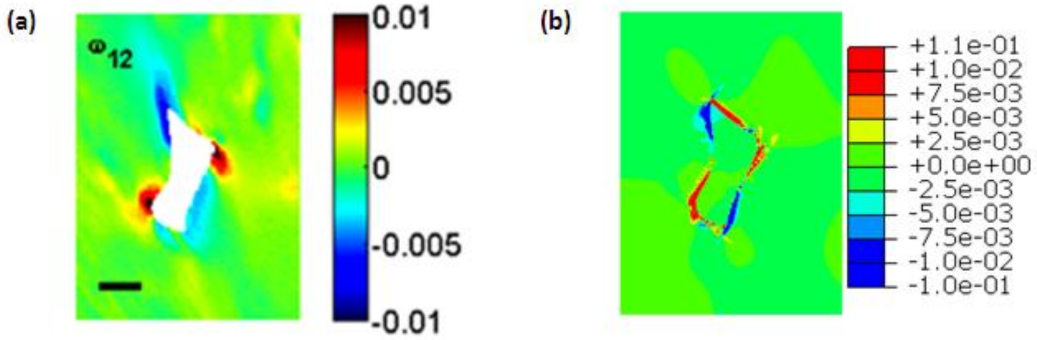

Figure 43. Field plots of in-plane lattice rotation component (a) experimentally determined and (b) predicted from the crystal plasticity finite element model. The range is the same for both figures.

The crystal plasticity finite element simulation downplays the role of the lattice rotation component when compared to the experimental measurements, but predicts correctly the clockwise and anti-clockwise sense of the rotation fields around the carbide particle. Shown below in Figure 44 is a comparison between the estimated geometrically necessary dislocation (GND) density and that measured experimentally by high-resolution EBSD.

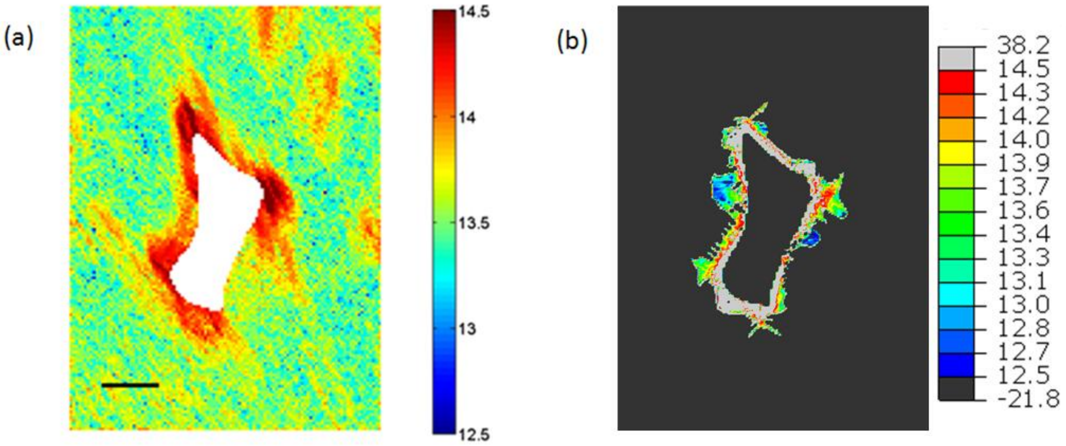

Figure 44. Logarithmic plots of density of geometrically necessary dislocations (GNDs in lines/m^2) (a) experimentally determined and (b) those predicted from the crystal plasticity finite element model. The range is the same for both figures.

The crystal plasticity model manages to predict the GND density around the carbide particle pretty close to that from the experiment measurements. In order for a better comparison, we measure the plastic zone size from the above data. For this, we make a lower cut-off approximation for the GND density data value. In this example, the clearly visible plastic zone around the carbide has a GND density of at least about 10^{14} and so we choose this lower limit to measure the zone size. From the experimental measurement, the plastic zone size estimate is close to 80 μm^2, and the crystal plasticity simulation predictions are about 75μm^2, based on the same assumption (that the clear plastic zone in the area where the GND density is at least about 10^{14} /m^2).

It must be noted that the GND data predictions from the crystal plasticity finite element model are not extracted from the lattice rotations, which is what the experimental technique replies on. Hence, although there is not a good prediction of the lattice rotations in this particular case, the GND density prediction still holds pretty good.

Overall, the crystal plasticity formulation is able to predict a large range of parameters, some of which are lattice strains (both plastic and elastic), rotations and GND densities. The magnitudes of these parameters may be a little uncertain owing to the vague thermal expansion coefficient (and modulus) of the carbide particle. Most of the simulations have been performed with values of thermal expansion coefficient and modulus of the carbide being roughly about ten times that of the surrounding Nickel matrix. Added to this, is also the unfamiliar and undefined nature of creep and to the temperature drop to which it is effective. Thus the $\Delta\alpha\Delta T$ applied to the model may not be accurate in the magnitude.

This however does not really effect the spatial variation of the strain, lattice rotations and GND density distributions. Although the magnitudes might be a bit different, they should look very similar to the plots from these simulations

5. Monotonic Deformation

This chapter will present high-resolution EBSD maps around some carbide particles on a sample after mechanical deformation (three point bending). As a result of heat treatment (described in §1) on these samples and cooling from such high temperatures combined with the difference in thermal expansion co-efficients between the matrix and the carbide results, there is already considerable thermal residual strain around the carbides. Fifteen such carbides were identified through the height of these beams and mapped both before and after mechanical deformation.

After 15 carbides (on the single crystal sample ‘S4’) were mapped using high resolution EBSD, the superalloy bar sample was deformed in a three-point bend rig. In the single crystal ‘S4’ sample, nine areas were mapped across the height of the beam and four such areas in the polycrystal ‘P1’ sample. EBSD maps were then taken in the same regions as before mechanical deformation, without any further polishing. Optical microscopy revealed clear slip steps on the sample surface on multiple slip systems. Similar steps were also observed in the polycrystal sample ‘P1’, in which six areas around the carbides were mapped. In addition to areas around the carbides, several areas away from the carbides were also mapped.

5.1. Experimental measurement of elastic strain and lattice rotations

The mechanical deformation was performed in a three-point bend rig, as described in §3.2 and shown in Figure 23. For the two samples, a displacement of 0.5mm was applied downwards (in the ‘x_2’ direction) on the central loader. The following Figure 45 shows the load vs extension graph plotted from the DMG-Rubicon software program controlling a DMG test frame on the sample ‘P1’. Although the demand on the test frame was set to 0.5mm displacement on the central roller, there is always a deformation on the test rig setup. The graph has been corrected to eliminate the effect from the rig setup.

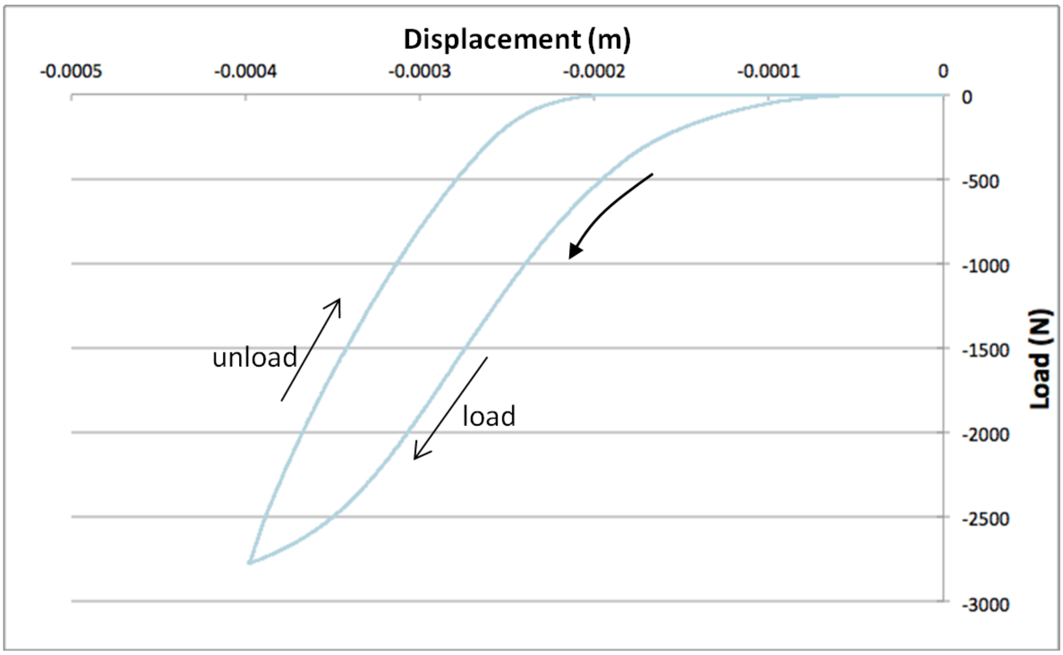

Figure 45. Load vs corrected displacement for the sample ‘P1’.

As seen from the graph above, there is only a central loader displacement of about 0.4mm, although the original demand was 0.5mm imposed on the test frame. From the graph, the beam sample has a bending stiffness of about 3.2E+07 N/m. The approximate load at yield point is about 2.1 kN. After unloading, the maximum deflection at the centre of the beam is about 0.2mm.

Without any further polishing, the sample was mapped using high-resolution EBSD. The figure below shows the slip steps on the sample ‘P1’.

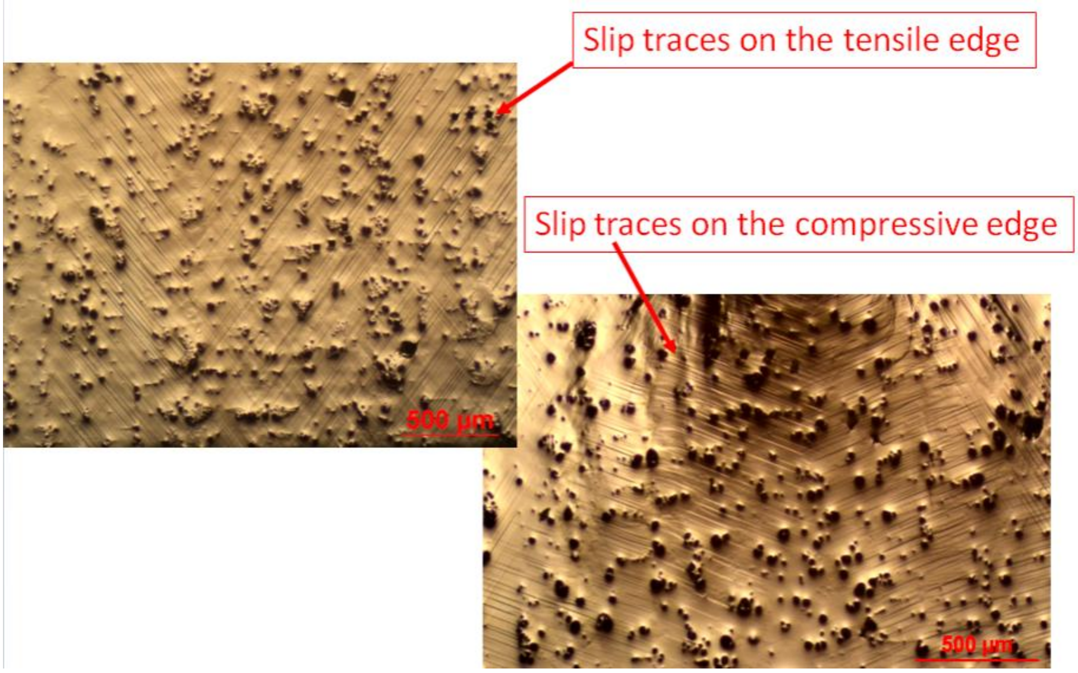

Figure 46. Slip traces on the deformed sample 'P1'.

As already discussed at the end of §3.3, selecting a strain-free reference pattern is problematic after mechanical deformation. The residual stresses vary across the bent sample and mean that the reference point chosen for the analysis of the bent sample will not in general be at zero elastic strain. This is a significant point and means that although the maps obtained from high-resolution EBSD capture the spatial changes well, there is an unknown constant value to be added to all points in the map. Secondly, the pattern of plastic deformation across the bent beam leads to longer range variations in the residual elastic strains. To overcome this issue we combine the EBSD strain mapping with a simple finite element analysis of the beam.

Figure 47 shows a finite element simulation (using the commercial FE code ABAQUS) of the three-point bend test. The top roller was moved downwards to impose a vertical displacement of 0.4 mm (to match with the experiment), and then moved upwards to leave the beam bent but fully unloaded. Figure 47(b) shows the distribution of plastic strain along the beam axes that results for the bending. The contact at the central roller significantly affects the distribution of plastic strain on the compressive side of the beam. The residual elastic strains are also available within the FEA simulation and Figure 47(a) shows the distribution of the elastic strain along the 'x_1' axis of the beam. Absolute strains are obtained by combining the EBSD data with finite element analysis (FEA) simulations, giving the average residual elastic strains in the mapped region. Lattice curvatures and elastic strain gradients can be determined and used to recover the GND density distribution independently of the FEA simulation.

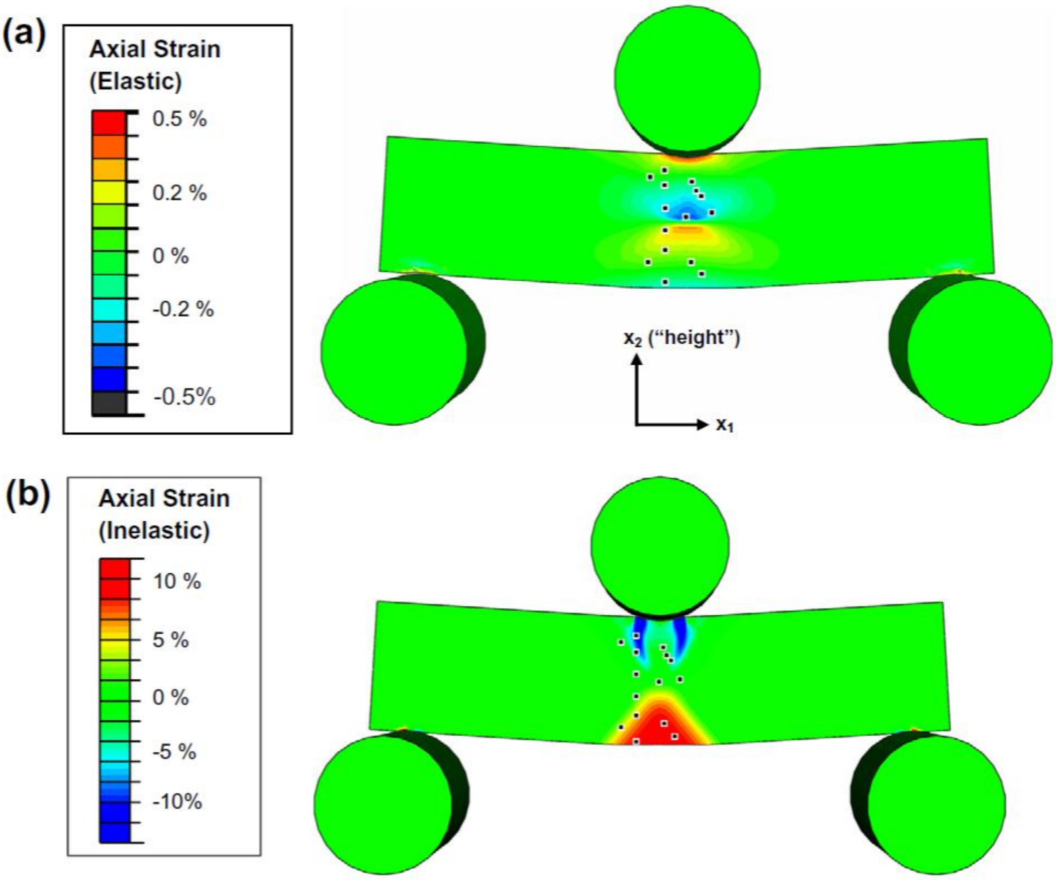

Figure 47. Finite element simulation of the three-point bend test (after unload) and showing carbide particles mapped at various levels of imposed mechanical strain (a) showing elastic strain, and (b) showing inelastic strain.

The FEA simulation was undertaken using ABAQUS software. A three-dimensional finite element mesh with about 8500 eight-node brick elements (incompatible modes) was used for the discretization of the beam. No constraints were applied to elements making up the beam other than through contact with the rollers, thus the surface of the beam is essentially in plane stress-like conditions. The three rollers were modelled to stay rigid throughout the simulation. The bottom rollers were fixed in all directions. Loading from the top roller was controlled to give a load–unload cycle, whose maximum displacement was 0.5 mm. The contact surfaces between the beam and the rollers were defined to have a friction coefficient of 0.5. The (isotropic) elastic constants used for the beam are as follows: Young's modulus E of 207 GPa and Poisson's ratio of 0.28, as supplied by Rolls-Royce plc. Conventional continuum plasticity was used to model the deformation in this case with the yield strength of 810 MPa and a plastic tangent modulus of 75 MPa.

Figure 48 shows the results from EBSD mapping after bending from the same carbide as shown before bending in §4.2, for which the FEA simulation showed that the bending imposed a strain of ~-6% along the 'x_1' axis in the region. A reference point far from the carbide was used in the cross-correlation analysis and a constant term added/subtracted so as to bring the mean values of each elastic strain components to level found in the FEA simulation. In this way we preserve the high spatial resolution information from the EBSD measurements of the elastic strain variation, and use the simple FE model to establish the mean values required to give absolute values to the strains.

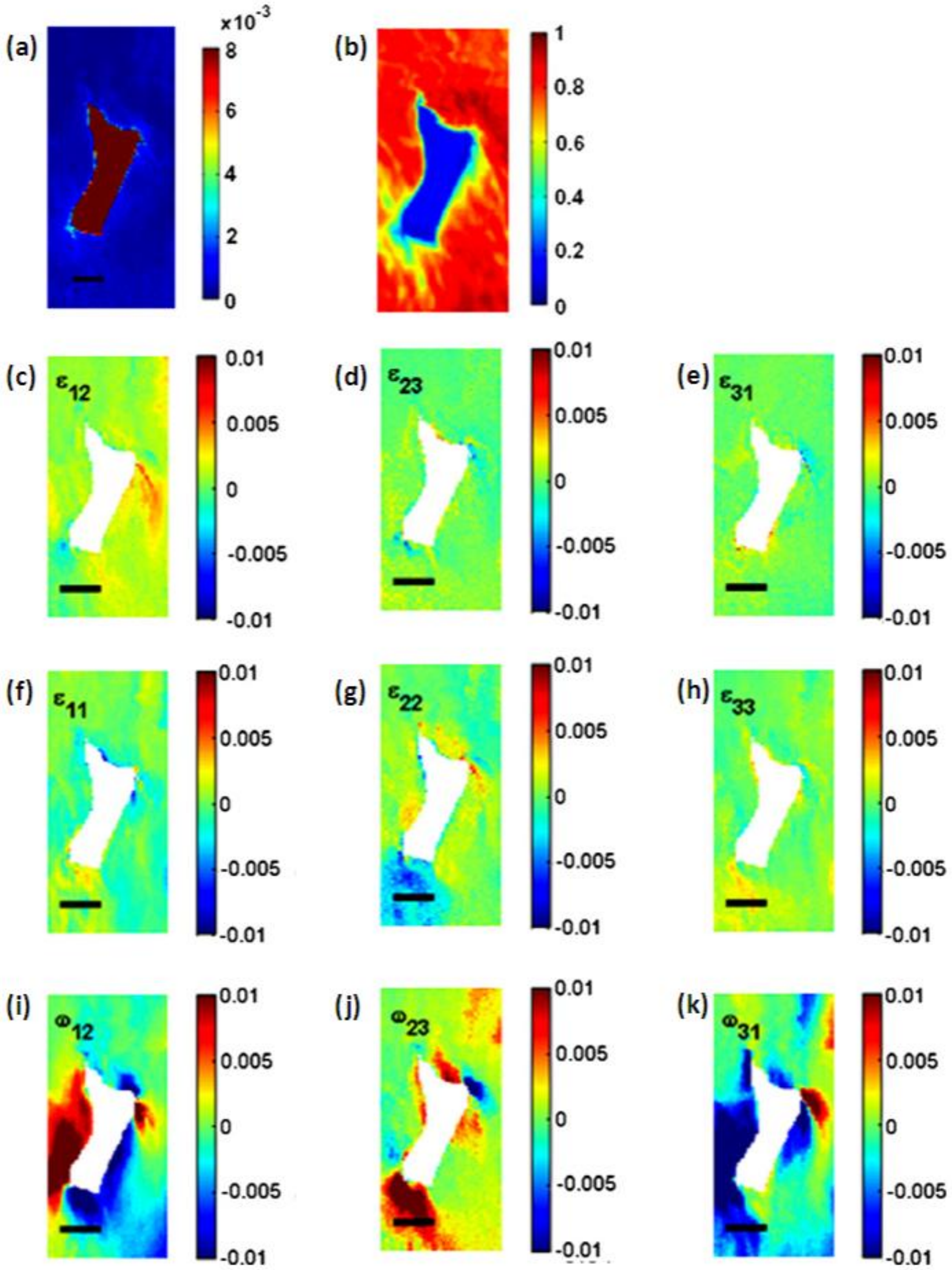

Figure 48. Strains and rotations near selected carbide after mechanical loading to a local strain of ~6% compression: (a) mean angular error, (b) cross-correlation peak height, (c) ε_{12}, (d) ε_{23}, (e) ε_{31}, (f) ε_{11}, (g) ε_{22}, (h) ε_{33}, (i) w_{12}, (j) w_{23}, (k) w_{31} (rotations in radians). The scale bars are 5 μm long and the step size is 0.25 μm per pixel.

Compared to the maps before bending, the peak height has somewhat reduced (Figure 48(a)) and the mean angular error somewhat increased (Figure 48(b)) within the matrix, especially in regions close to the carbide. The plastic deformation has essentially removed the variation in strain along the 'x_1' axis compared to those present from thermal loading. The out of plane shear strains ε_{23} and ε_{31} remain small in accord with the traction-free surface plane. The lattice rotations are much larger than the elastic strain variations. The rotations about the surface normal (Figure 48 (i)) are much larger in magnitude and extend much further from the carbide than was seen for the purely thermal loading case. The rotations about the horizontal and vertical axes (Figure 48(j) and (k)) have also changed substantially as a result of the imposed mechanical load.

On this single crystal sample (beam sample – 'S4'), fifteen carbide particles have been identified through the height of beam (along the x_2 axis in Figure 30) and using high-resolution EBSD in combination with the FEA model, these areas have been mapped after deformation. However, it must be noted that GND density distribution can be calculated independently of the FEA simulation.

Side by side comparisons of one such carbide (before and after bending) is shown below in Figure 50 and Figure 51. Reduction in cross-correlation peak height and an increase in the mean angular error are clearly visible in regions close to the carbide. After mechanical deformation, clear slip features are visible in both the normal and shear strain maps. An optical micrograph showing clear slip features is shown in Figure 49. Lattice strain and rotation maps (prior mechanical deformation and after deformation) follow.

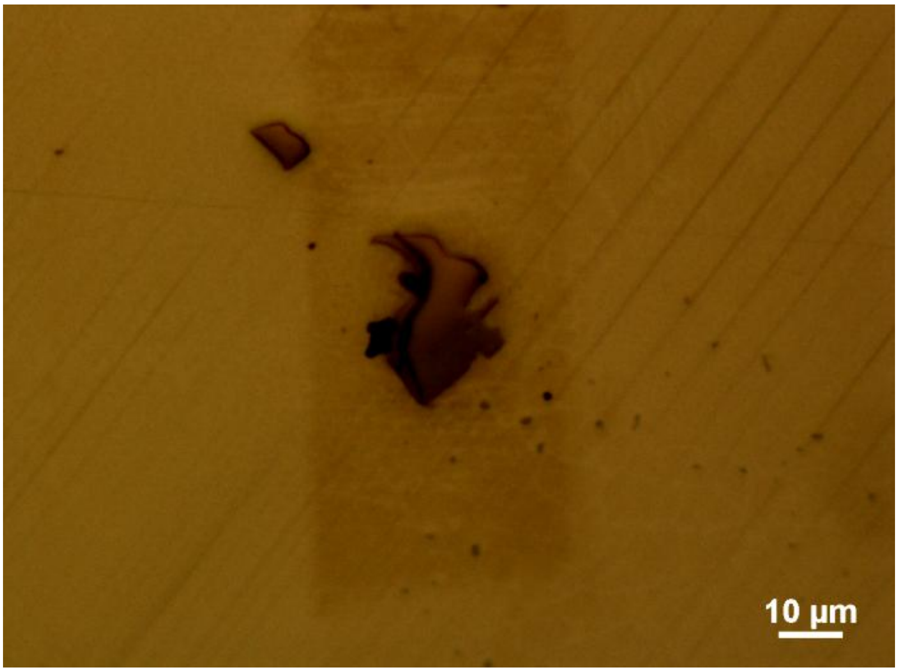

Figure 49. Optical micrograph of the carbide mapped in from sample 'P1' showing slip bands.

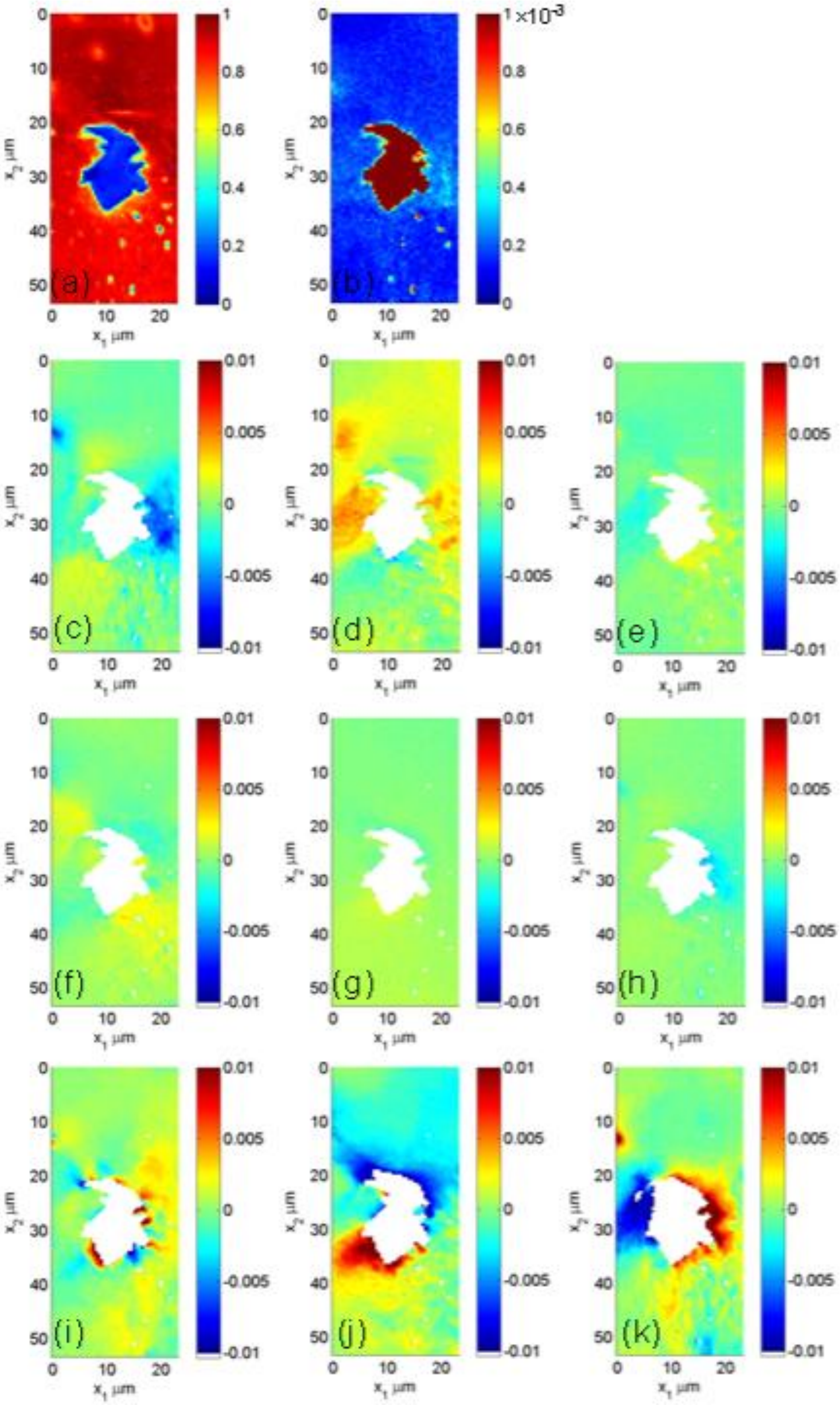

Figure 50. Thermally induced strains and rotations near selected carbide before mechanical loading (a) mean angular error, (b) cross-correlation peak height, (c) ε_{11}, (d) ε_{22}, (e) ε_{33}, (f) ε_{12}, (g) ε_{23}, (h) ε_{31}, (i) w_{12}, (j) w_{23}, (k) w_{31} (rotations in radians).

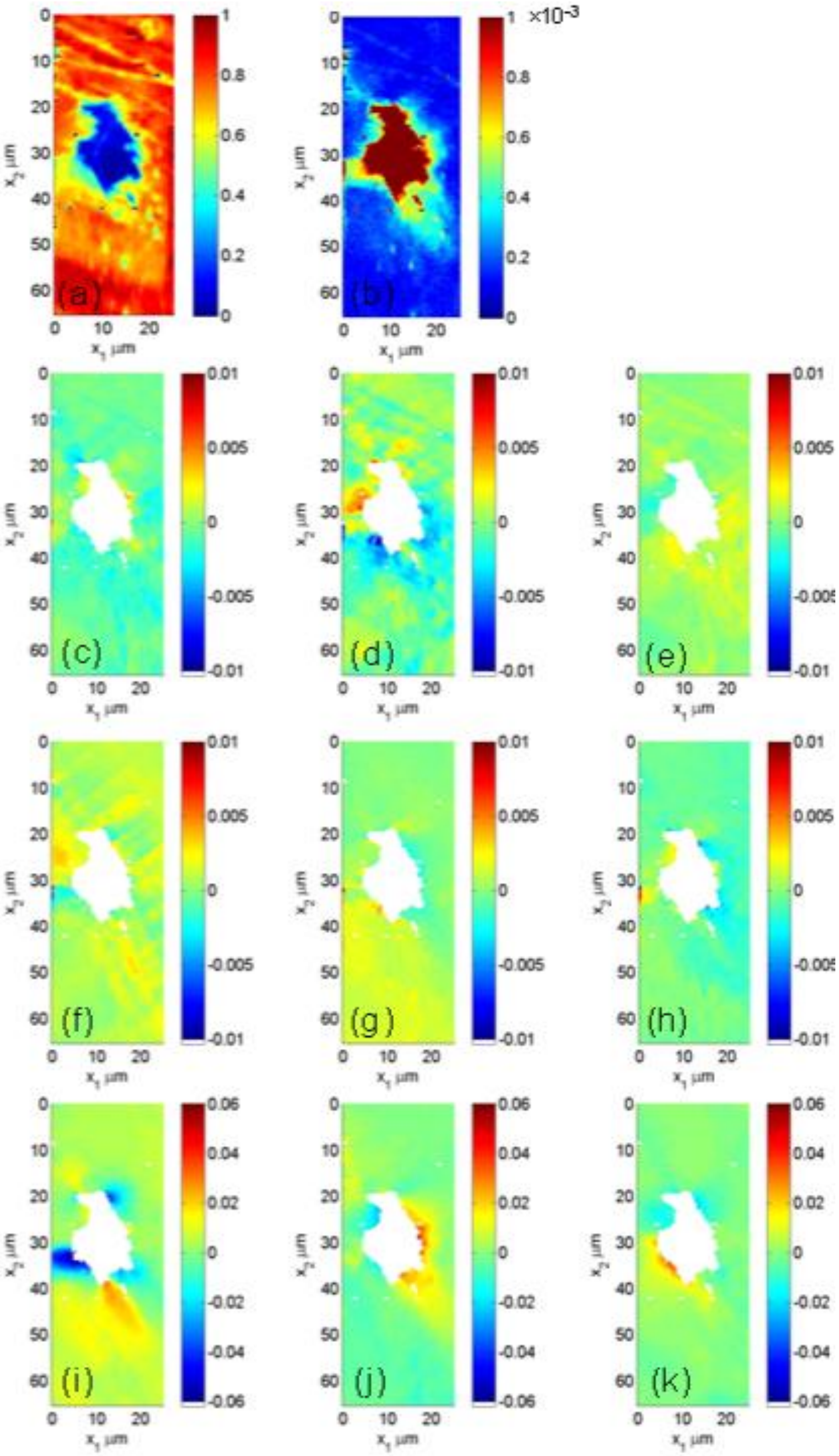

Figure 51. Strains and rotations near selected carbide after mechanical loading to a local strain of ~2% compression: (a) mean angular error, (b) cross-correlation peak height, (c) ε_{11}, (d) ε_{22}, (e) ε_{33}, (f) ε_{12}, (g) ε_{23}, (h) ε_{31}, (i) w_{12}, (j) w_{23}, (k) w_{31} (rotations in radians).

As all components of the elastic strain tensor have been determined and the elastic constants are known it is possible to calculate the stresses. Figure 53 shows the three in-plane stresses around another such carbide (from the single crystal sample ‘S4’) for which the bending imposed a total tensile strain of ~8%. An SE image of the carbide is shown in Figure 52 . The stress levels changing across slip steps are again evident and these stress variations tend to increase in magnitude close to the carbides (there is smaller carbide to the right of the larger central one).

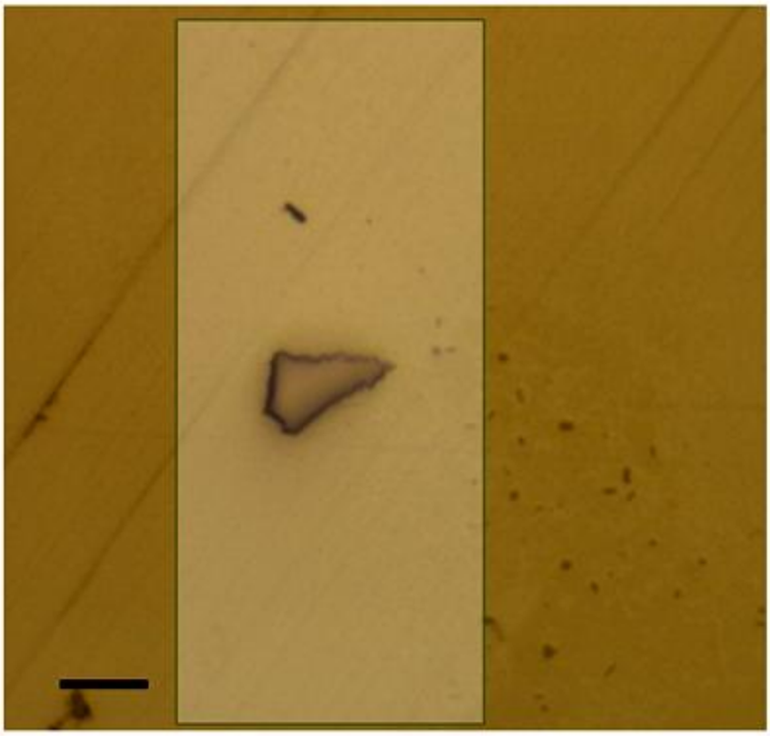

Figure 52. An optical micrograph of the carbide from sample 'S4'. The scale bar is 5 µm long.

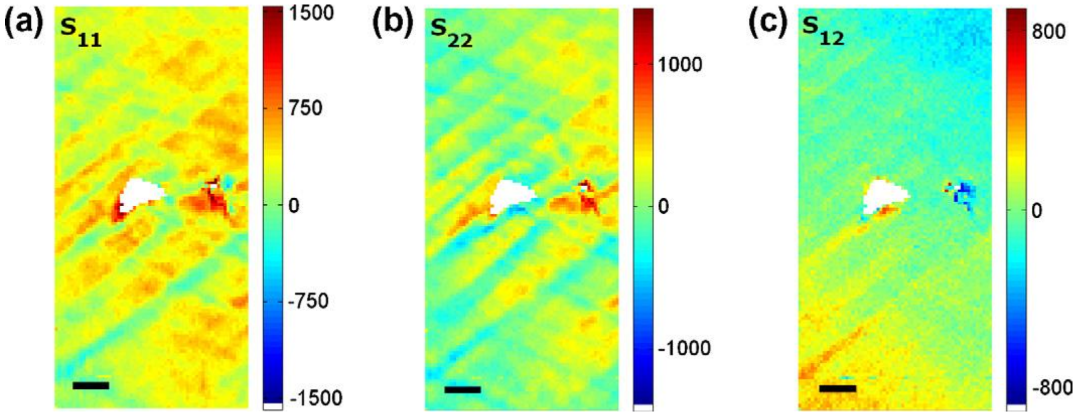

Figure 53. Residual stress distribution in a matrix region containing carbide particles in a region of the bend beam with a local tensile strain of ~8%: (a) σ_{11}, (b) σ_{22}, (c) σ_{12} (stresses in MPa). These stresses have been corrected to mean stress level given by the FE simulation. The scale bars are 5 µm long and the step size is 0.25 µm per pixel.

As already discussed, several areas away from the carbides have also been mapped. These maps show local elastic strain and rotation variations that correspond to slip plane traces within the Nickel matrix alone. One such map is shown below. The FE simulation shows a local tensile strain of 8% within this region. The strains have been corrected to the mean strain level given by the FE simulation. The mean angular error and cross-correlation maps are shown below in Figure 54.

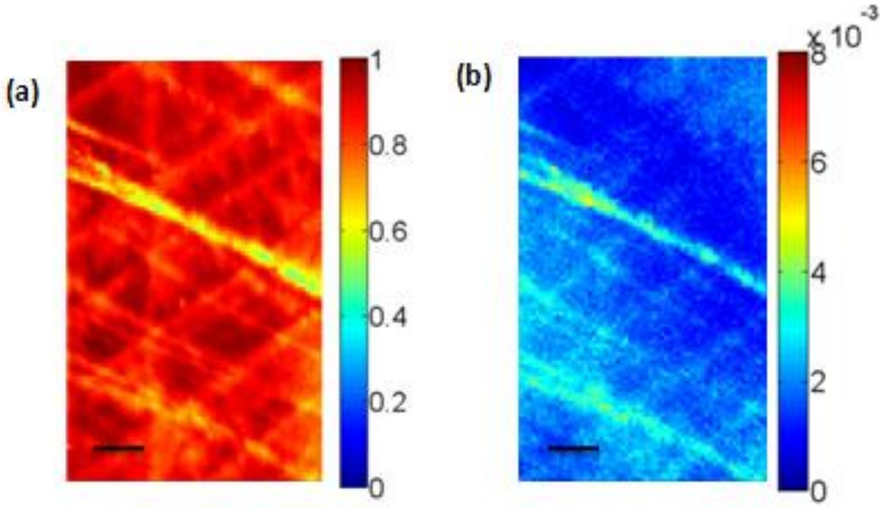

Figure 54. (a) cross-correlation peak height (b) mean angular error (rads) in a region away from carbide particles, with a local tensile strain of ~8%. The scale bars are 5 µm long and the step size is 0.25 µm per pixel.

From both the cross-correlation peak height and mean angular error maps, it is evident that there are clear slip features running from one side to the other and in two different sets. There is pretty good correlation throughout the map area (more than about 0.8) except in areas close to the slip steps. The mean angular error map in Figure 54(b) also shows a low angular error throughout most of the mapped area.

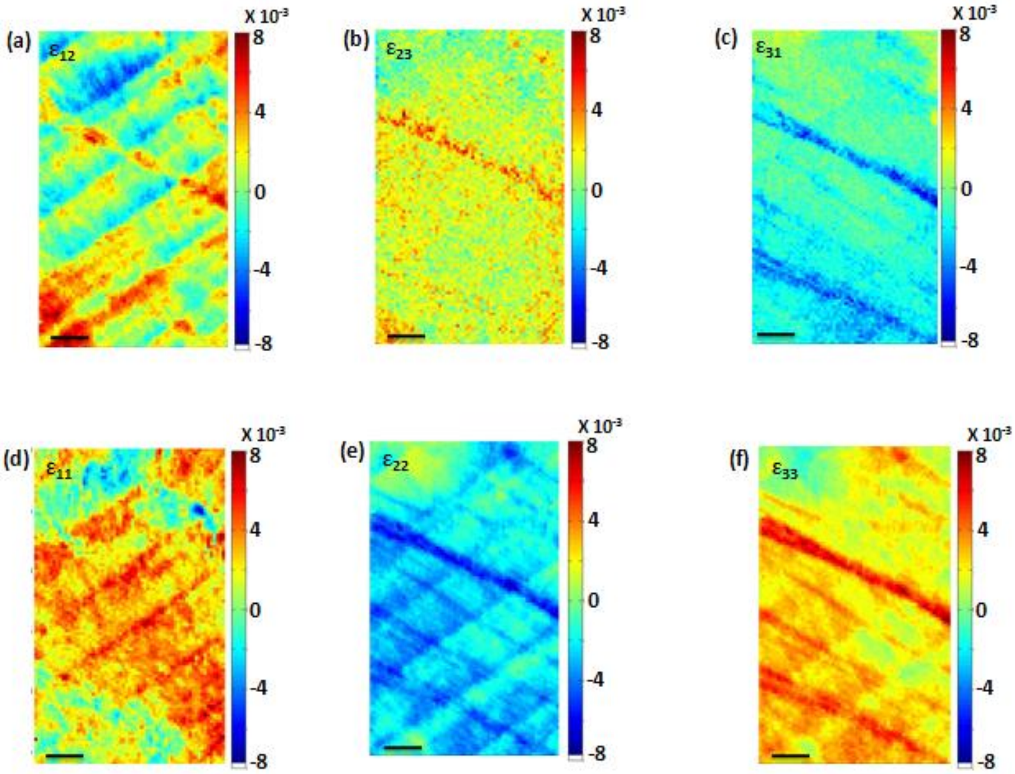

Figure 55. Elastic strains around the areas mapped in Figure 54 after mechanical loading to a local strain of ~8% in tension: , (a) ε_{12}, (b) ε_{23}, (c) ε_{31}, (d) ε_{11}, (e) ε_{22}, (f) ε_{33}. The scale bars are 5 µm long and the step size is 0.25 µm per pixel.

The in-plane elastic shear strain map (Figure 55(a)) shows clearly evident slip steps and larger strain accumulation around the steps. Similar trends are also observed in all the other strain maps. These strains have been corrected from the FEA simulation, corresponding to a region of 8% strain in tension. When compared to the other terms, the two out of plane shear strains remain close to zero (Figure 55 (b) and (c)). As already discussed in the chapter relating to thermal strains, this is not unexpected since the corresponding stresses σ_{23} and σ_{31} are almost zero in order to fulfill the traction-free surface condition. The measured lattice rotations (Figure 56) are clearly pretty large when compared to the elastic strain terms.

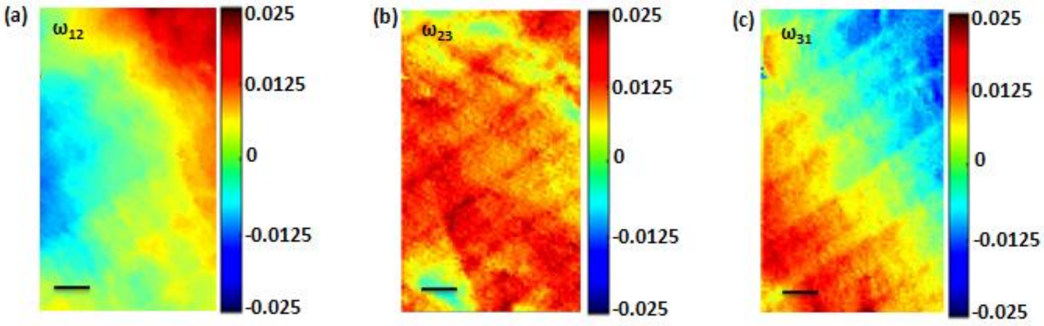

Figure 56. Lattice rotations around the area mapped in Figure 54 after mechanical loading to a local strain of ~8% in tension (a) w$_{12}$, (b) w$_{23}$, (c) w$_{31}$ (rotations in radians). The scale bars are 5 µm long and the step size is 0.25 µm per pixel.

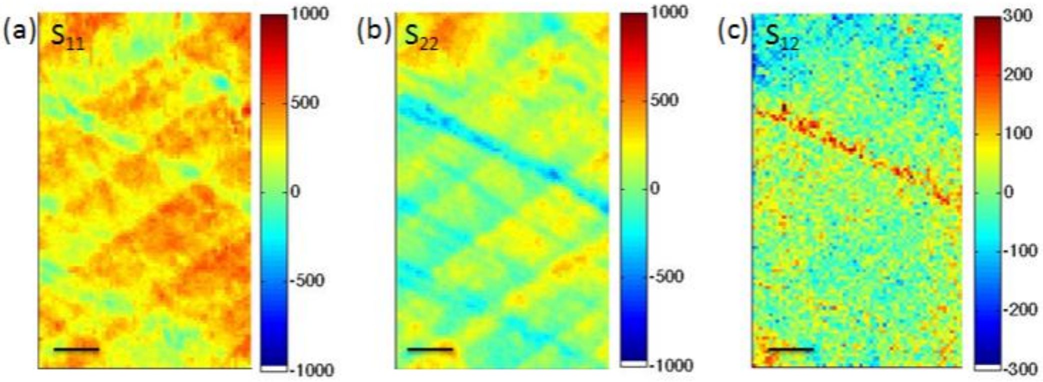

Figure 57. Residual stress distribution in a matrix region away any obvious carbide particles in the region mapped from Figure 54 of the bend beam with a local tensile strain of ~8%: (a) σ_{11}, (b) σ_{22}, (c) σ_{12} (stresses in MPa). These stresses have been corrected to mean stress level given by the finite element simulation. The scale bars are 5 µm long and the step size is 0.25 µm per pixel.

Figure 57 shows the three in-plane stresses for the matrix region on which the bending imposed a total tensile strain of ~8%. There are obvious and large changes in the two normal stress levels across two sets of linear features that correspond to slip steps seen on the deformed surface. The shear stress map shows much smaller variations.

5.2. GND measurement

As already discussed in §4.2.1 using the three lattice rotations components measured by high angular resolution EBSD, six of the nine rotation gradients required to form the Nye's dislocation tensor can be calculated. The remaining three concern variation of the lattice rotations with depth below the surface and are inaccessible. Using these six components it is possible to calculate a lower bound solution to the density of geometrically necessary dislocation densities (GNDs).

The elastic strain gradients can also contribute to the lattice curvatures and hence the Nye's dislocation tensor as discussed by Kroner [50]. The different symmetry of the strain tensor (symmetric) compared to the rotation tensor (antisymmetric) leads the gradients of different strain components along the depth direction to contribute to six of the nine terms in the dislocation tensor. The measured elastic strain gradients are generally small compared to the rotation gradients and so we base our solution for the GND densities on the six available rotation gradients. Where the relevant elastic strain gradients are available we use these to make small corrections to the rotation gradients.

We then use an L_1 optimization routine (within Matlab) to find a set of GND densities that generate the six (partially corrected) rotation gradients measured by EBSD and minimize the total GND line energy. We treat the matrix as an fcc metal with the standard 12 $\langle 110\rangle\{\bar{1}11\}$ slip systems which gives 18 GND types (6 screw, and 12 edge) as discussed in detail by Arsenlis and Parks [98].

Maps showing total GND densities after bending are shown in this section. The GND density within about 5 µm of the carbide edge is significantly raised. After mechanical deformation the size of the plastic zone and GND density within it are obviously increased as a result of the plastic strain gradient caused by the plastically rigid particle. Measurements at other carbides show that the GND content close to the particles increases as the magnitude of the plastic strain in the surrounding matrix is increased (in both tension and compression). In Figure 58, the total GND density around the carbide particles is shown after mechanical deformation from the three particles already shown in this chapter (two from single crystal sample ‘S4’ and third from polycrystal sample ‘P1’). Comparison with those measured prior to mechanical deformation (after thermal strain) are made soon after.

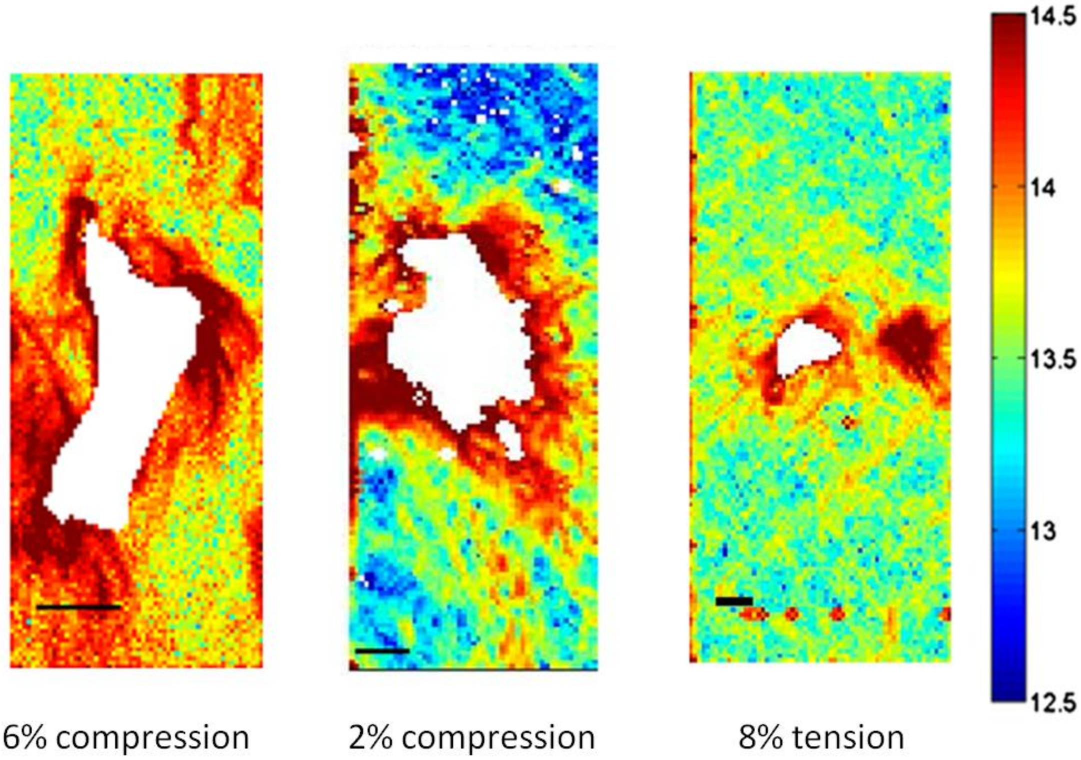

Figure 58. Total GND density distribution around carbides discussed in this chapter from samples S4, P1 and S4 respectively after mechanical deformation. The scale bars are 5 µm long and the step size is 0.25 µm per pixel.

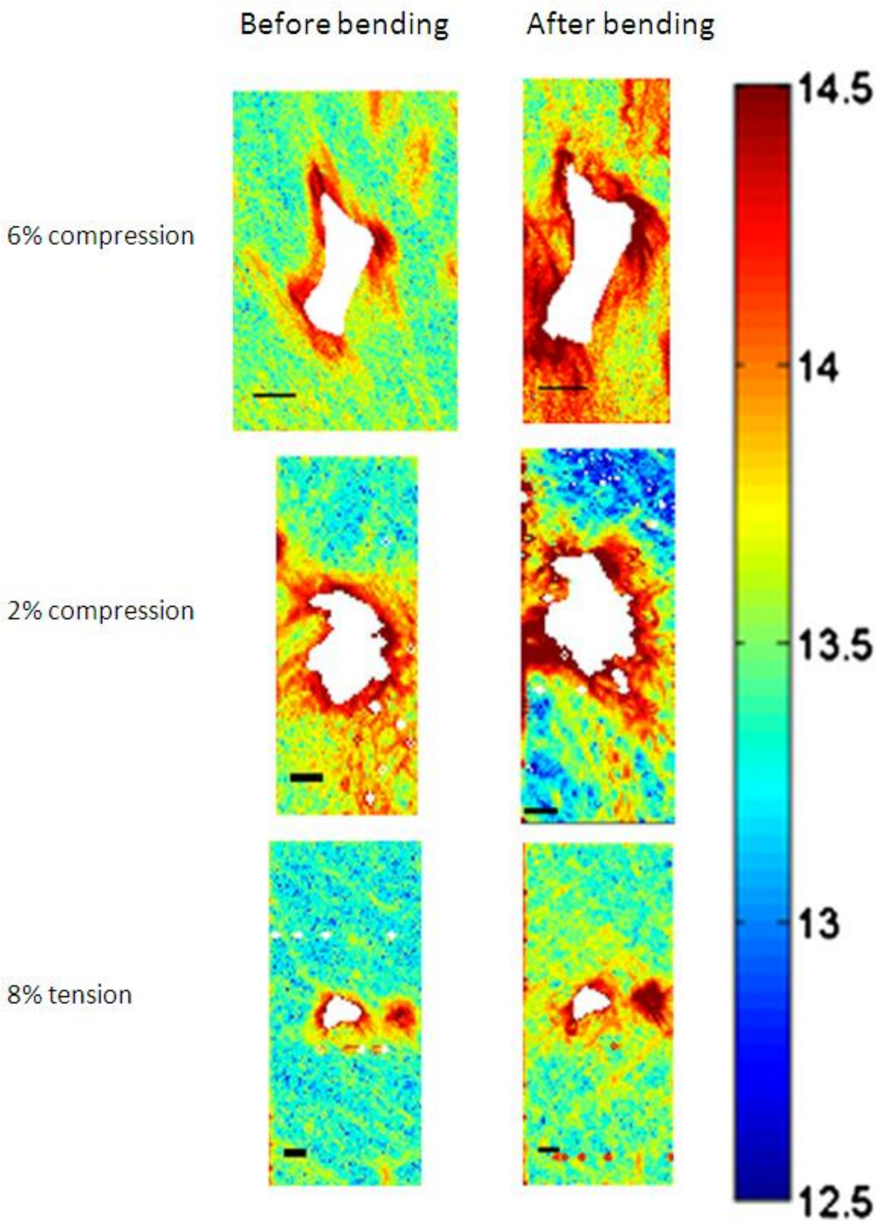

Figure 59. Comparison of GND densities before and after bending (left column and right column respectively) for those carbide regions referred to in Figure 58.

It is clear from the above Figure 59 that after mechanical deformation the size of the plastic zone and GND density within it are obviously increased. This is a result of the plastic strain gradient caused by the plastically rigid particle. Measurements at other carbides show that the GND content close to the particles increases as the magnitude of the plastic strain in the surrounding matrix is increased (in both tension and compression). This is discussed later in this chapter.

As already explained, the GND densities are generated from the six (partially corrected) rotation gradients measured by EBSD and minimized total GND line energy. We treat the matrix as an fcc metal with the standard 12 $\langle 110\rangle\{\bar{1}11\}$ slip systems which gives 18 GND types (6 screw, and 12 edge) as discussed in detail §3.4. The following figures illustrate plots (a total of 18) showing the deconstruction onto individual slip systems, used to construct the total GND density.

It should be emphasized that these figures present only one set of GNDs that support the measured lattice curvatures while minimizing the dislocation line energy and that there are many other combinations of GNDs that can generate the same lattice curvatures. This particle carbide (from sample P1) had been subjected to an imposed mechanical strain of 8% in tension. The maps in Figure 60 and Figure 61 show distinct dislocation pileup of specific types of GNDs around the carbide. Also clearly seen are sets of linear features that correspond to the alignment of planar slip steps seen on the sample surface.

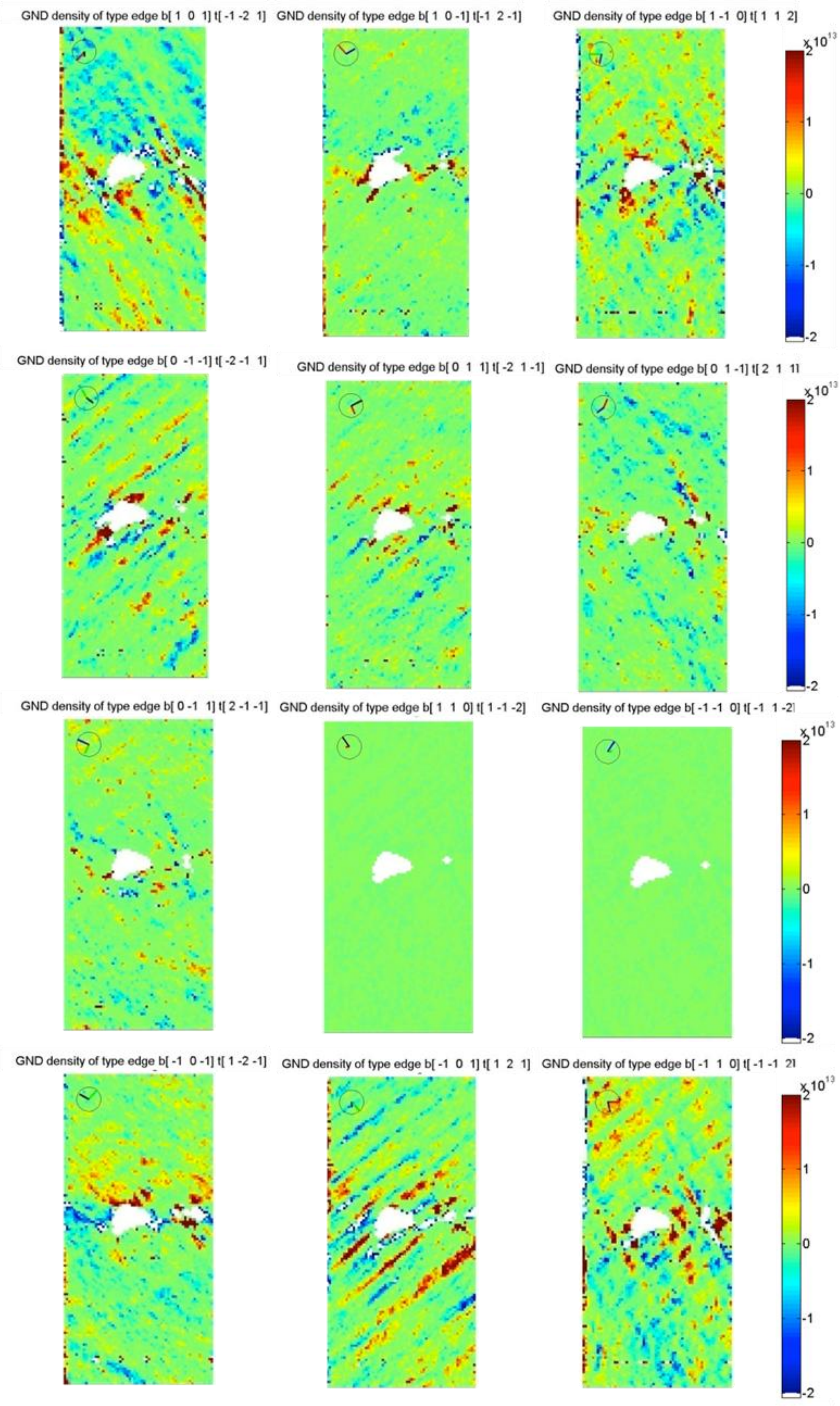

Figure 60. Set of 12 edge dislocations (deconstructed from total GND density) for the carbide from sample 'S4', depicted in Figure 52.

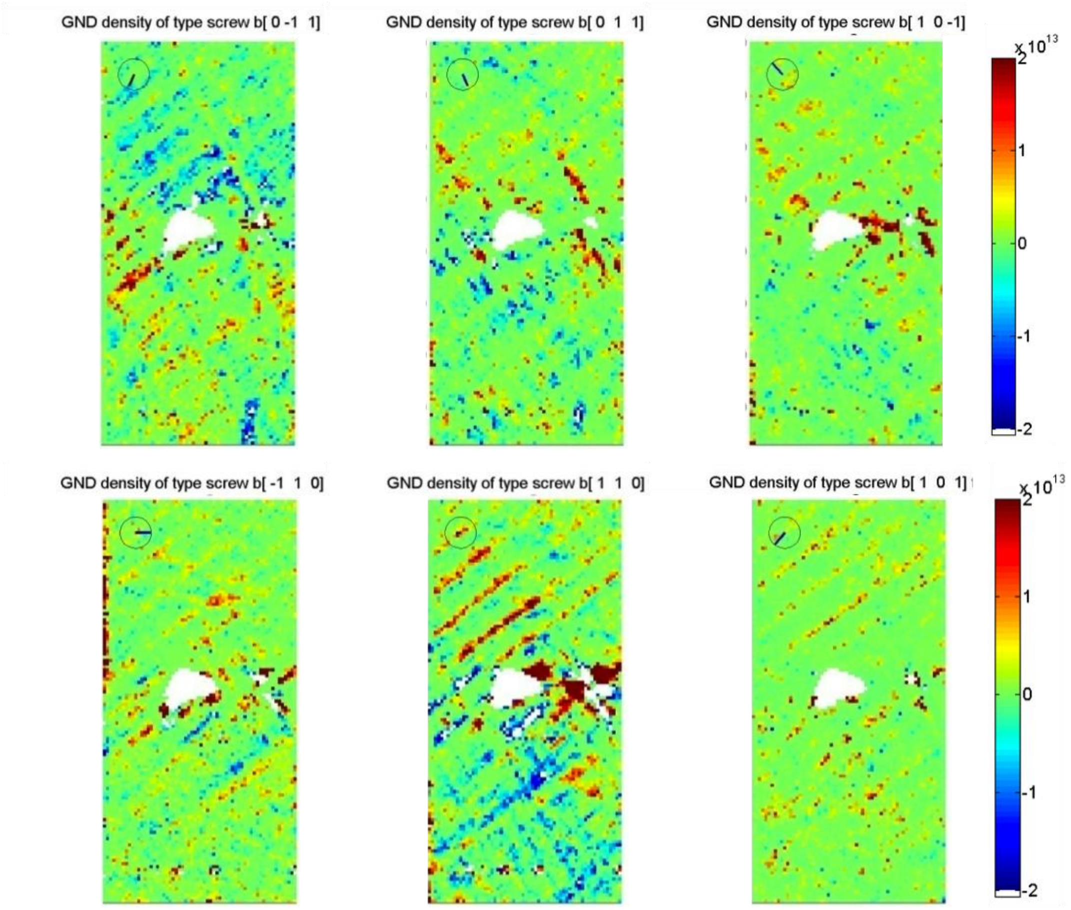

Figure 61. Set of 6 screw dislocations (deconstructed from total GND density) for the carbide from sample 'S4', depicted in Figure 52.

The 'clock face' in the top left hand corner for each plot indicates the projection of direction of the dislocation line and Burgers vectors. The Burgers vector is red if pointing into the page and green if pointing out of the page. The line direction is white if pointing into the page and black if pointing out of the page. The length of each line with respect to the unit circle indicates how closely aligned the vector is with the page, if it touches the circle then the vector lies in the plane of the page.

These plots in Figure 60 and Figure 61 showing the density of individual types of GNDs are given on a linear scale with negative densities, implying that the sense of the dislocation is reversed (i.e. negative Burger’s vector with sign of line direction preserved). In many of these figures, it is clear that some slip bands contain an excess of dislocations of one sense while others contain an excess with the opposite sense. Indeed the sign of the excess dislocation tends to alternate on moving across a sequence of parallel slip planes.

The storage of dislocations in this case (after mechanical deformation) is also heavily localized to within 5µm of the carbide edge, where the dislocation density is at least 10^{14} dislocations per m^2. The background dislocation density for all slip systems used, far from the particle, is about 10^{13} dislocations per m^2.

The following plot (Figure 62) shows the average GND density measured in the background (in regions away from the carbide particles) in the single crystal sample ‘S4’ across the 3mm height of the beam sample. Comparison is then made later with the average GND density measured in areas around carbide particles (Figure 63).

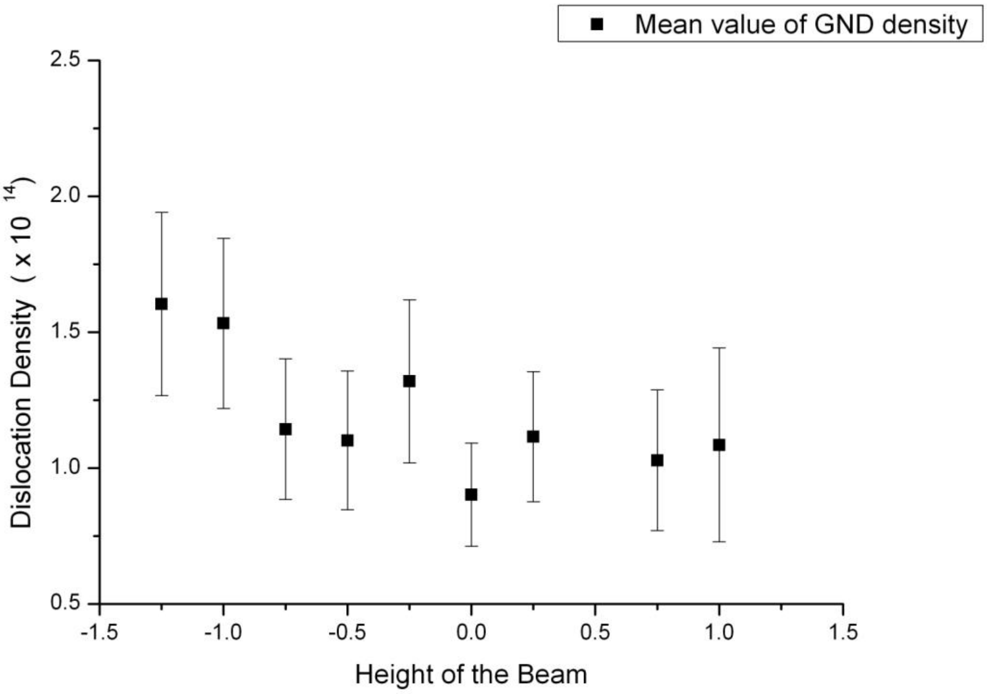

Figure 62. Average GND density distribution across the height of the beam sample 'S4', negative values of position indicating the compressive half above the bending axis.

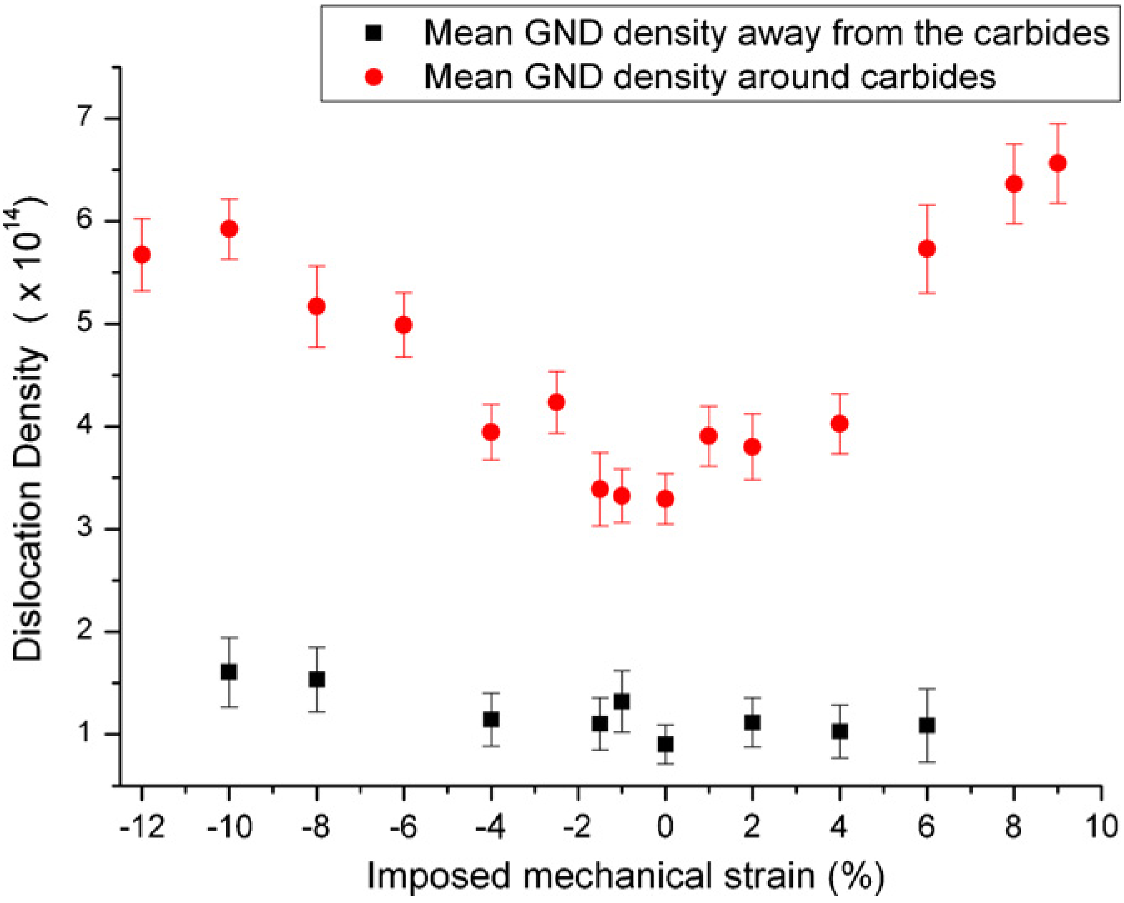

Figure 63. Average GND density distribution as a function of axial strain (due to imposed mechanical loading) across the height of the beam.

We have already defined a plastic zone size as the area around the carbide particle where the GND density increases suddenly to a pretty large value, in §4.2.1. The outer boundary of this plastic zone is distinguished by a sudden increase in the GND density from that in matrix surrounding the carbide particle and the inner boundary by the edge of the carbide particle (as can be seen in Figure 58). The average GND measurement around the carbides here has been made within this defined plastic zone (within about 2-4µm around the carbide particle).

Compared to regions close to carbides there is much less variation with macroscopic position across the height of the beam, though some slight increase with magnitude of the local strain is observed. The error bars shown correspond to the one standard deviation from the mean value of GND density. The plot shows elevated levels of GND densities around carbide particles when compared to areas away from the carbides.

The GND density measurement is linked to the strain gradients. The plot in Figure 63 looks at the average GND density vs. local strain, but does not include a length scale. The plot below (Figure 64) shows the average GND density development with respect to the carbide particle size.

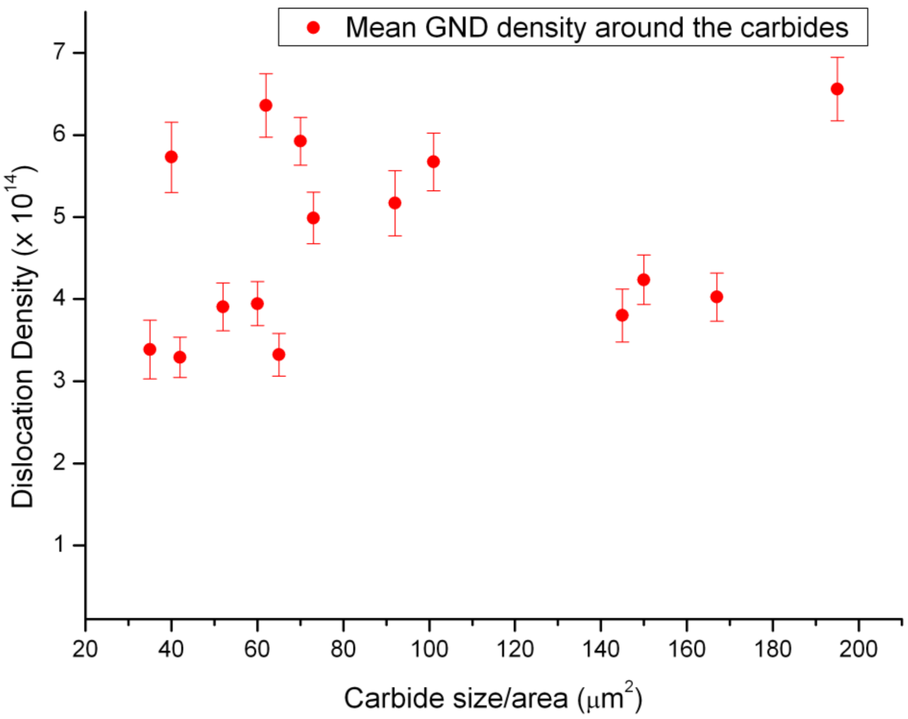

Figure 64. Average GND density around carbide particles in the sample as a function of the size of the carbides.

It should be noted that the amount of strain imposed (in bending) over each carbide is in no relation to the carbide particle size/area. Just as in the case of thermal loading, we can make an estimate of the plastic zone size around these carbide particles. A plot of the plastic zone size vs. carbide particle size (like in the case of thermal loading) may not be adequate to explain the details as the imposed strain on each carbide is very different across the height of the beam, but as a function of the imposed strain might be more significant. The following plot (Figure 65) shows the plastic zone size (defined already as the area around the carbide particle where the GND density increases suddenly to a pretty large value) as a function of the imposed mechanical strain in the region around that particular carbide particle.

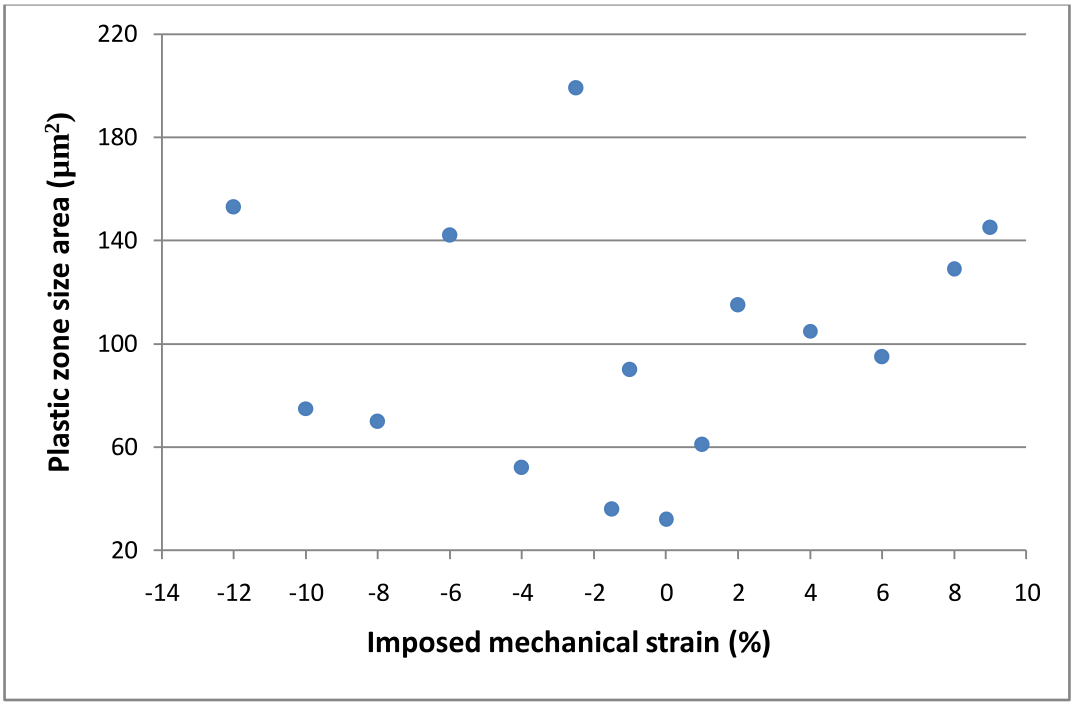

Figure 65. Plastic zone size area around carbide particles as a function of axial strain (due to imposed mechanical loading) across the height of the beam.

Although with a few exceptions, the general trend of the plot in Figure 65 is similar to that in Figure 63. The plastic zone size seems to grow around carbides subjected to higher mechanical strain.

From the results illustrated so far in this chapter, the room temperature bending leads to highly planar slip as is evident from slip traces present on the sample surface. The imposed strains for the regions shown in Figure 48 and Figure 51 are an order of magnitude larger than the thermally induced misfit strains (those from §4.2) which no longer contribute significantly to the strain and rotation fields. In these locations within the bent beam the residual elastic strains (and hence stresses) found in the FEA simulation are rather low. However, the local stress variations measured by the EBSD method are quite significant. For the maps shown in Figure 57, the root mean square deviation from the mean is 125 MPa, 145 MPa and 61MPa for σ_{11}, σ_{22} and σ_{12} respectively, which are significant given the matrix has a critical resolved shear stress of ~230MPa [17]. Stress changes across a glide plane containing an array of edge dislocations spaced a uniform distance of ~100 nm apart are of similar magnitude to the measured variations. This dislocation spacing implies a dislocation density of ~10^{14} m^{-2} so that the stress variations are consistent with the GND densities obtained from the lattice curvatures.

Such high GND densities away from the carbides appear at first instance to be much larger than what might be anticipated. The strains vary from ~12% tension to ~12% compression across the 3 mm height of the beam, giving an approximate average strain gradient of 80 m^{-1} to be supported, which only requires a GND density of ~3 x 10^{11} m^{-2}. One point to note is that the GND density depends crucially on the length scale (or patch size) of the assessment. The estimate above takes a rather macroscopic viewpoint in determining the dislocation content needed to affect the shape change of the whole bent beam, while the EBSD analysis uses a microscopic viewpoint using an array of points separated by 250 nm. At the smaller step size a greater fraction of the dislocations within the sample must be classed GNDs rather than SSDs and so a value above the macroscopic estimate is expected.

6. Cyclic Deformation

This chapter will present high-resolution EBSD maps around several areas in samples deformed by cyclic loading. As a result of heat treatment (described in §1) on these samples and cooling from such high temperatures combined with the difference in thermal expansion co-efficients between the matrix and the carbide results, there are already considerable thermal residual strains around the carbides.

Two samples, a polycrystal sample (P9) and a single crystal sample (S7) were deformed in four point bending, which has already been discussed in §3.2. On each of the samples, regions around some carbides were mapped prior to cyclic deformation. Cyclic loading has been performed with interruptions at stages to observe the deformation phenomena associated around carbides, matrix regions and a grain boundary.

6.1. Mechanical Loading under four-point bending

The size restrictions of the samples from the bar-stock make it difficult to build a tensile rig and thus bending was the best alternative. A four point bending rig has the advantage of fully reversed loading of the test specimen without any contact of the specimen within the region of maximum bending stress created between the two inner bending points. A carefully designed 4 point bending rig has been constructed to carry out cyclic loading of the beam samples. The design of this rig has already been presented in §3.2.

The cyclic loading was carried out on an Instron test frame, where the cross-head movement is via a screw driven mechanism. Thus, this frame has an upper speed limit on the movement and loading. The fastest oscillation on a mild steel specimen of similar dimensions was limited to about 0.25Hz. This ruled out the possibility of high cycle fatigue loading. Thus, the sample could only be loaded in the low cycle fatigue regime.

An FE simulation of the four point bending test (as in the case of monotonic 3 point bending) was performed to estimate the total strain imposed by controlling displacement of the central loaders. The plan was to load the sample in a similar strain regime as the 3 point bending (about 10% strain in tension and compression, across the height of the beam). From a finite element 4-point bending simulation, the central loader displacement of about 0.3mm resulted in a strain variation of a magnitude of 10% across the height of the beam, in the section between the 4 central loading rollers.

Figure 66 shows a finite element simulation (using the commercial FE code ABAQUS) of the four-point bend test. Only the four active rollers (for this cycle) are modeled here. The top rollers were moved downwards to impose a vertical displacement of 0.3 mm (to match with the experiment), and then moved upwards to leave the beam bent but fully unloaded. Figure 66(b) shows the distribution of plastic strain along the beam axes that results for the bending. The residual elastic strains are also available within the FEA simulation and Figure 66(a) shows the distribution of the elastic strain along the 'x_1' axis of the beam.

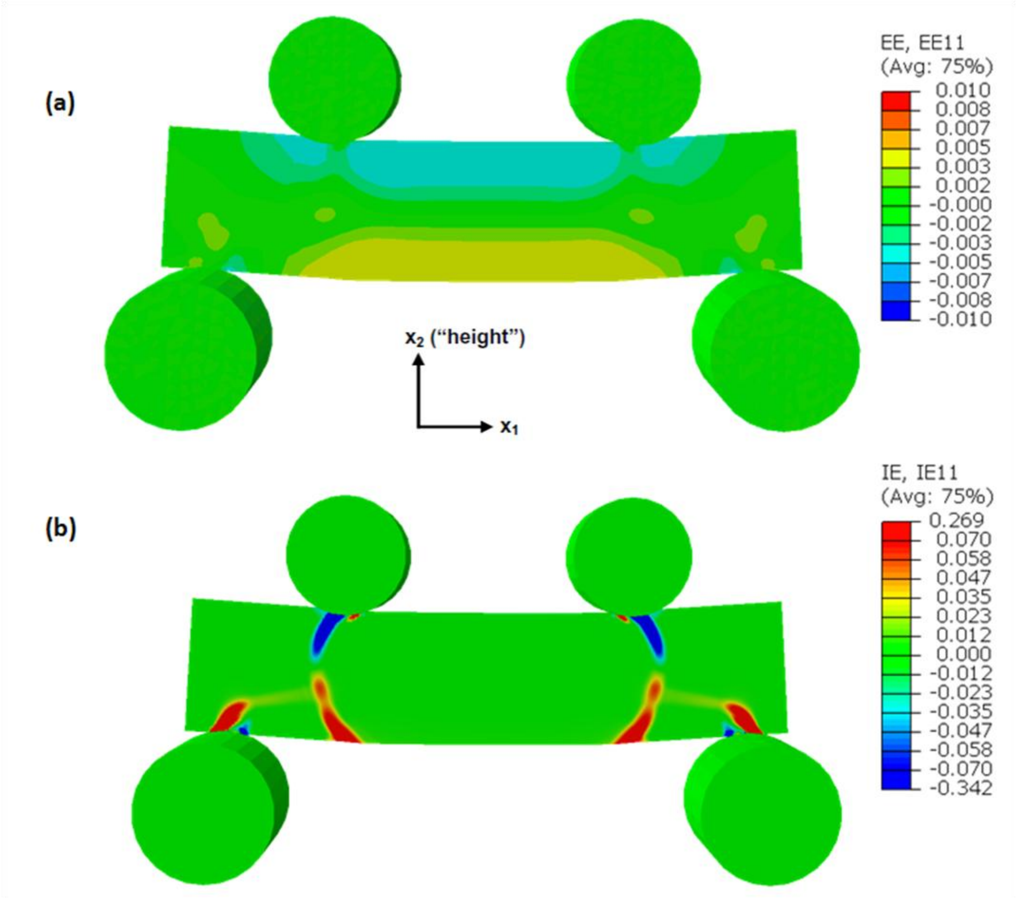

Figure 66. Finite element simulation of the four-point bend test (after unload) (a) showing elastic axial strain, and (b) showing inelastic axial strain.

This simulation was carried out just as in the case of the three-point bending simulation. A three-dimensional finite element mesh with about 8500 eight-node brick elements (incompatible modes) was used for the discretization of the beam. No constraints were applied to elements making up the beam other than through contact with the rollers, thus the surface of the beam is essentially in plane stress-like conditions. The four rollers were modelled to stay rigid throughout the simulation. The bottom rollers were fixed in all directions. Loading from the top roller was controlled to give a load–unload cycle, whose maximum displacement was 0.3 mm. The contact surfaces between the beam and the rollers were defined to have a friction coefficient of 0.5. The (isotropic) elastic constants used for the beam were as follows: Young’s modulus E of 207 GPa and Poisson’s ratio of 0.28, as supplied by Rolls-Royce plc. Conventional continuum plasticity was used to model the deformation in this case with the yield strength of 810 MPa and a plastic tangent modulus of 75 MPa. Just as was done with the three-point bending results, absolute strains have been obtained by combining the EBSD data with finite element analysis (FEA) simulations, giving the average residual elastic strains in the mapped region. Lattice curvatures and elastic strain gradients were determined and used to recover the GND density distribution independently of the FEA simulation.

An initial test sample (‘P7’) of the Nickel based superalloy Mar-M-002 was loaded in the test rig with a central loader displacement of 0.3mm from the mean resting position, with a cyclic frequency of 0.125Hz. Although the demand was set to 0.3mm, the loading regime was only ±0.27mm, as often happens with most of such test rigs.

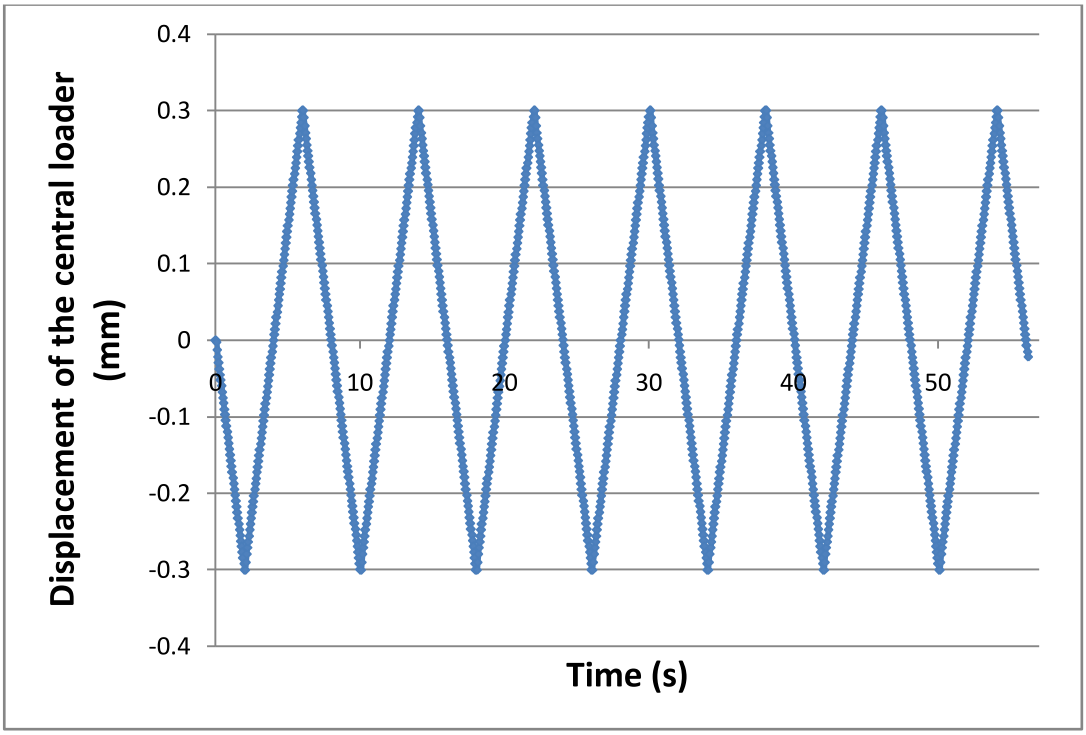

Figure 67. Displacement applied to centre of the Mar-M-002 test specimen 'P7' via central loaders of the 4pt reversible loading rig.

The following plot (Figure 68) shows the load vs. displacement graph for the test sample. It is evident from this graph that the effective displacement on the sample is only 0.27mm from the mean position although 0.3mm was applied to the loaders. This is probably resulting from the movement lost in clearance between the beam sample and the loaders while making contact in each cycle.

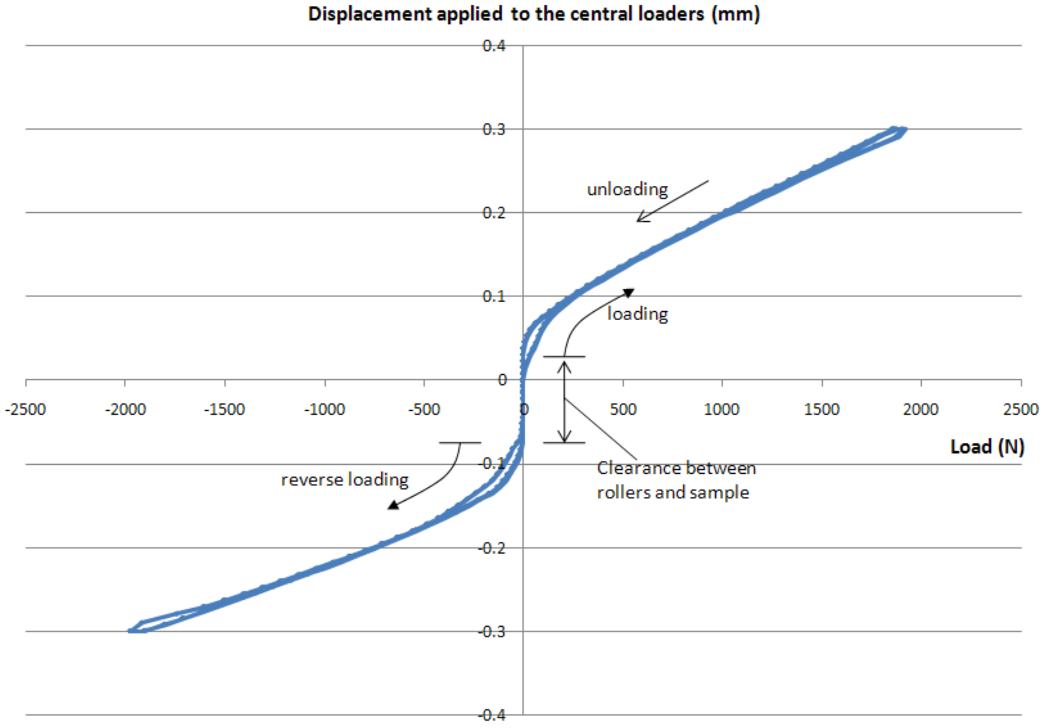

Figure 68. Load vs Displacement graph for the test sample (P7).

Dunne et. al [8] have loaded similar samples (of similar dimensions) to a strain of ±15% in 3-point loading and at a faster loading rate. These samples fractured in about 3000 cycles. The test sample 'P7' was loaded to a smaller strain level so as to increase the no. of cycles to failure. It was aimed to study a sample at interrupted loading and hence life cycle estimation was important. The test sample 'P7' fractured at ~16,000 cycles. It was then decided that further samples would be loaded in intervals of about 4000 cycles, then removed from the test rig for observation using optical microscope, SEM and EBSD before being returned to the fatigue rig.

6.2. Observations from cyclic loading

Prior to mechanical loading, 7 carbides (on the polycrystal sample ‘P9’) were mapped using high resolution EBSD, the superalloy bar sample was then subjected to cyclic loading in the four-point bend rig, interrupting at an interval of 4000 cycles. The initial few cycles of the load vs extension plot are shown below.

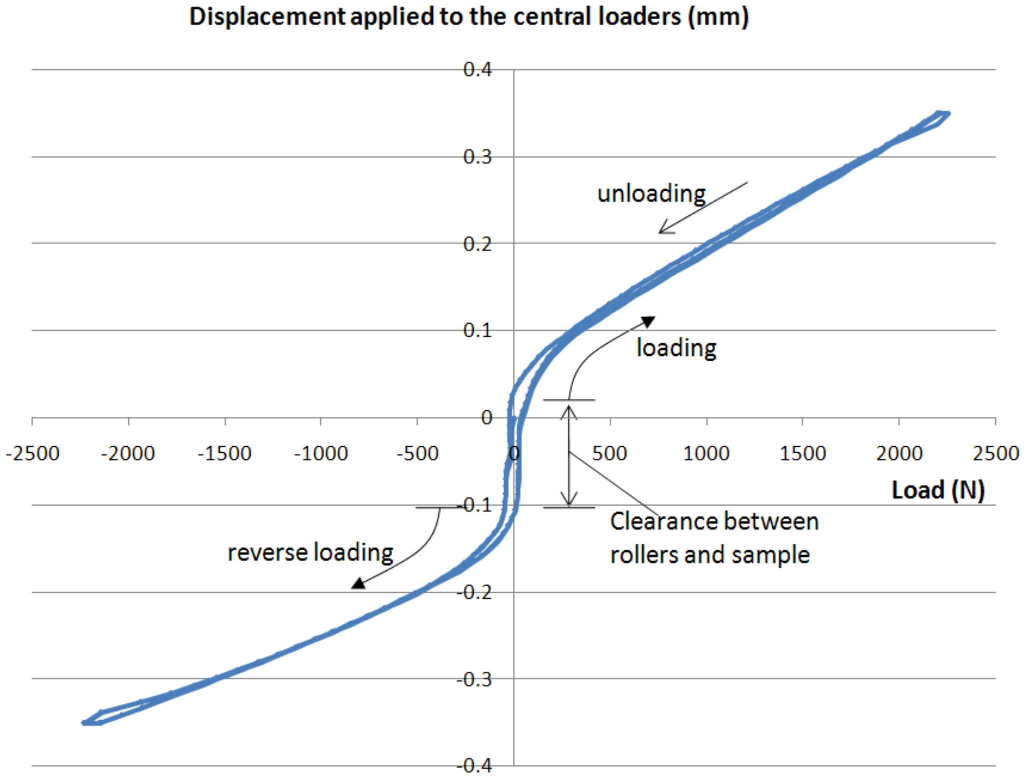

Figure 69. Load vs Displacement graph for the test sample (P9).

The demand on the central loader was set to 0.35mm. This resulted in an effective displacement on the sample of about 0.3mm, which was the original intention. This was attained by small trial increments to 0.3mm and was achieved in about 20 cycles. After

4000 cycles, the sample P9 was removed from the mechanical loading rig and placed under observation in the SEM.

6.2.1. Slip features

After 4000 load cycles, slip lines can clearly be seen upon the surface of specimen 'P9', in regions close to the roller contacts. This is clearly shown in Figure 70.

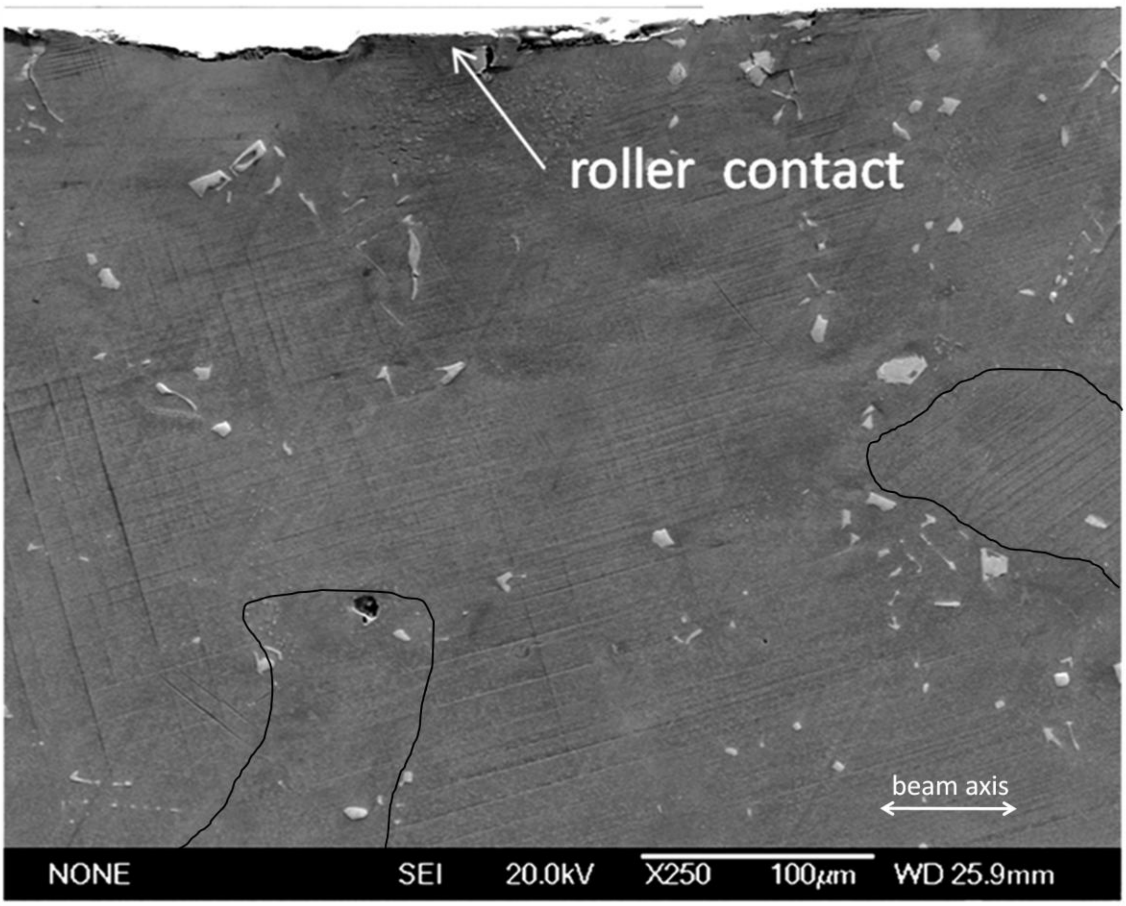

Figure 70. Slip lines visible near the roller contact surface on sample P9 after 4000 loading cycles.

From the finite element simulation in Figure 66, it can be seen that this area corresponds to an imposed strain of at least ±8% in each loading cycle. The slip line direction in this area can be clearly seen. Mostly, there is evidence of slip in two particular directions. On the right hand side of the image, the slip tends to change direction in the second grain. Figure 71 shows this tendency at a higher magnification for a region close to another roller contact.

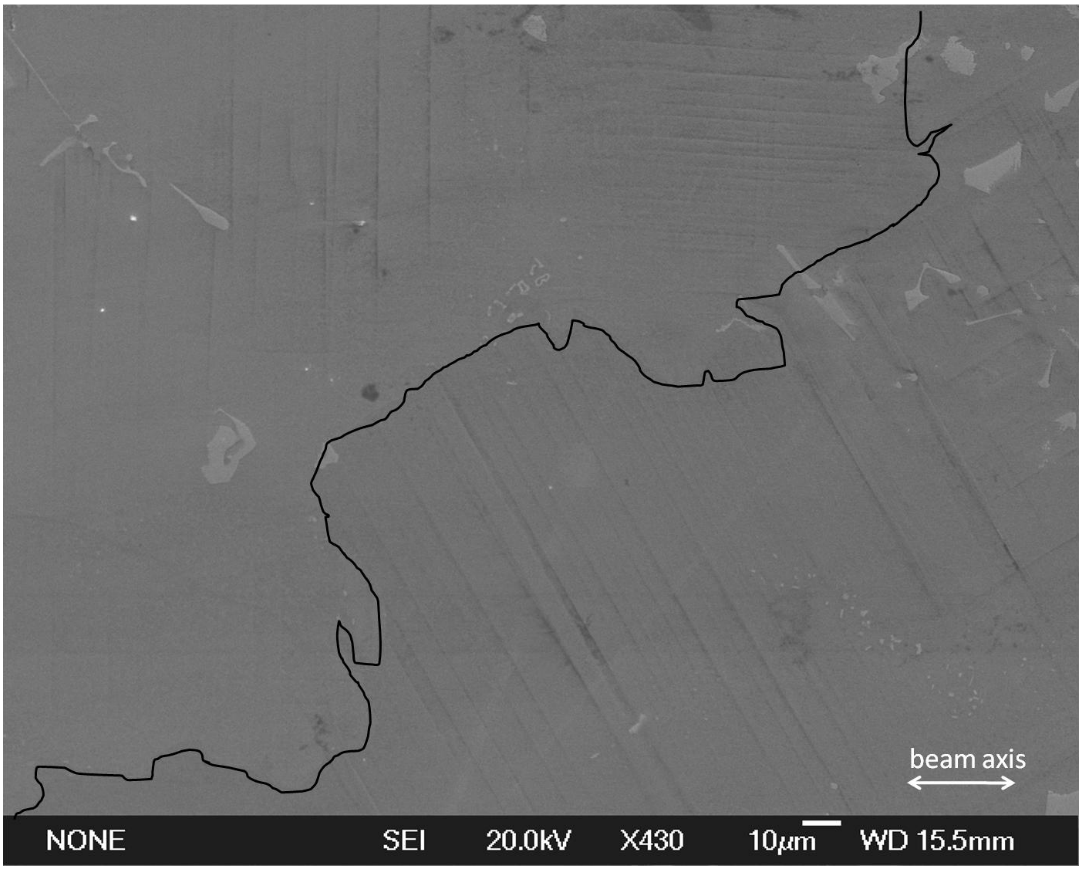

Figure 71. Slip lines clearly visible near roller contacts on sample P9 after 4000 cycles.

The sample was then mapped using high-resolution EBSD. Six areas were chosen, three around carbides and three from the matrix region. After cross-correlation analysis, the lattice strains, rotations and GND densities have been recorded. The sample was then placed back in the four point bend rig and subjected to another 4000 cycles of deformation.

6.2.2. Carbide cracking

After 8000 cycles of deformation, the most noticeable effect from the cyclic loading was the frequent occurrence of very small cracks initiating within the carbides. Two such instances are shown below in Figure 72. The local strain estimated from the finite element simulation in this region is about ±6% in each cycle.

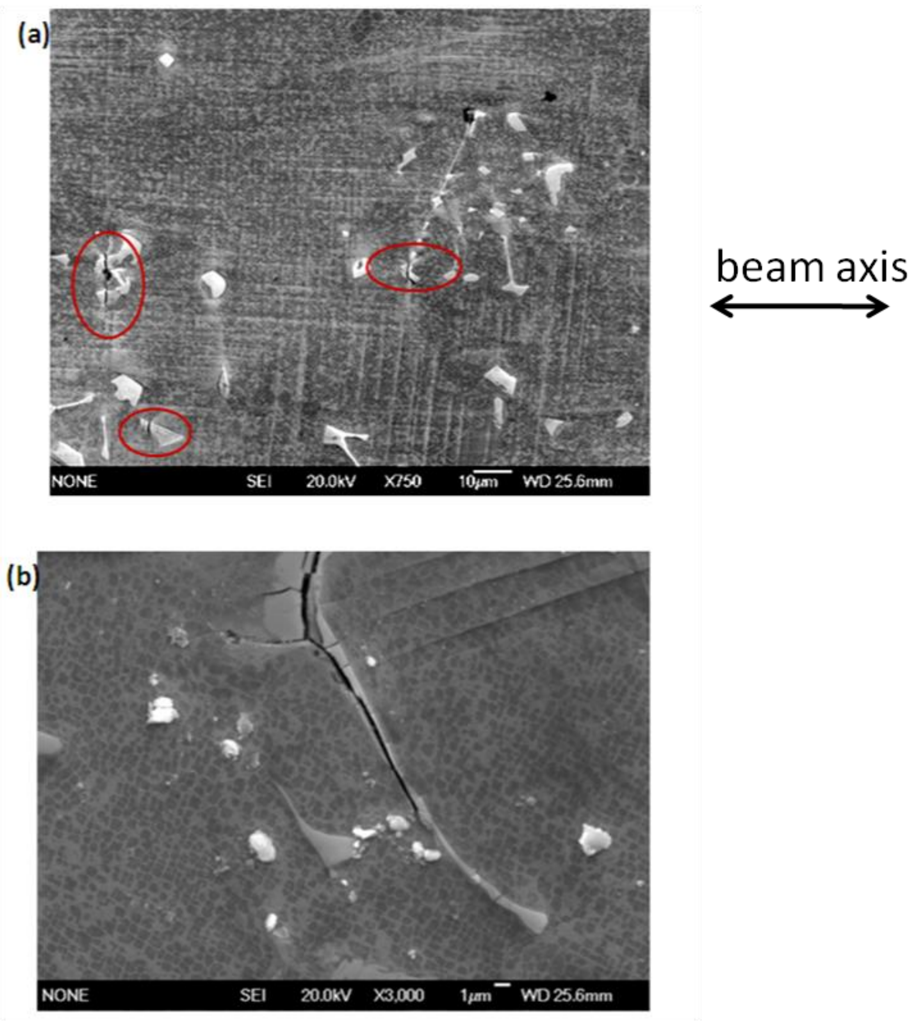

Figure 72. Carbide cracking in sample P9 observed after 8000 cycles of cyclic loading.

Three instances of carbide cracking have been shown (circled in red) in Figure 72(a). In Figure 72(b), the crack has started off and cut through the brittle carbide particle. Most of these small cracks have initiated and propagated either at the carbide/gamma matrix interface or just within the carbide particle. In most instances the carbide cracks have not extended into the metallic matrix.

Close to one of the sample edges, a small crack in the matrix has appeared after 8000 cycles. The local strain amplitude in this region from the finite element simulation is ±3%.

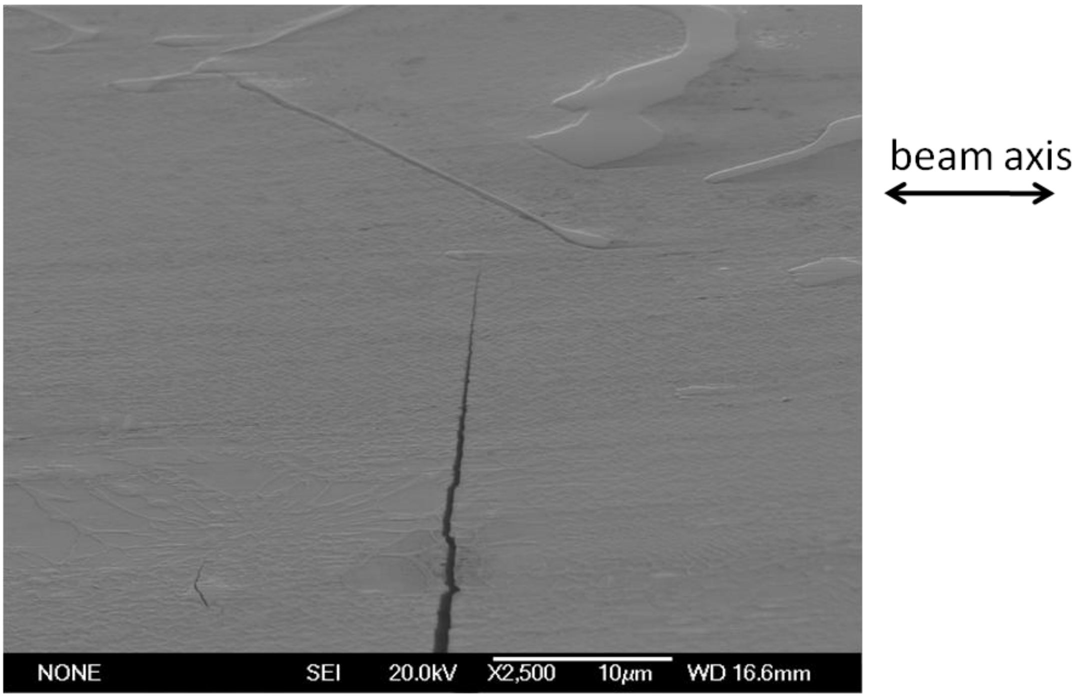

Figure 73. A very small crack that has started from one of the sample edges, after 8000 cycles.

The small crack looks more like a slip band when seen at normal incidence. This image in Figure 73, has been captured at an inclined angle of 70º, in a position originally intended for EBSD mapping. The path of this crack has been hindered by a small carbide particle, which appears to have either slowed or even arrested the crack propagation.

After EBSD mapping, the sample P9 was then placed back into the four-point bend rig and subjected to further deformation of 4000 cycles. After 12,000 cycles, several larger cracks were observed, mostly from the roller-sample interface. These large primary cracks were at least 50µm in length. Some smaller secondary cracks seemed to initiate from the larger cracks on both sides of the sample. The smaller cracks were only about 10-20 µm in length.

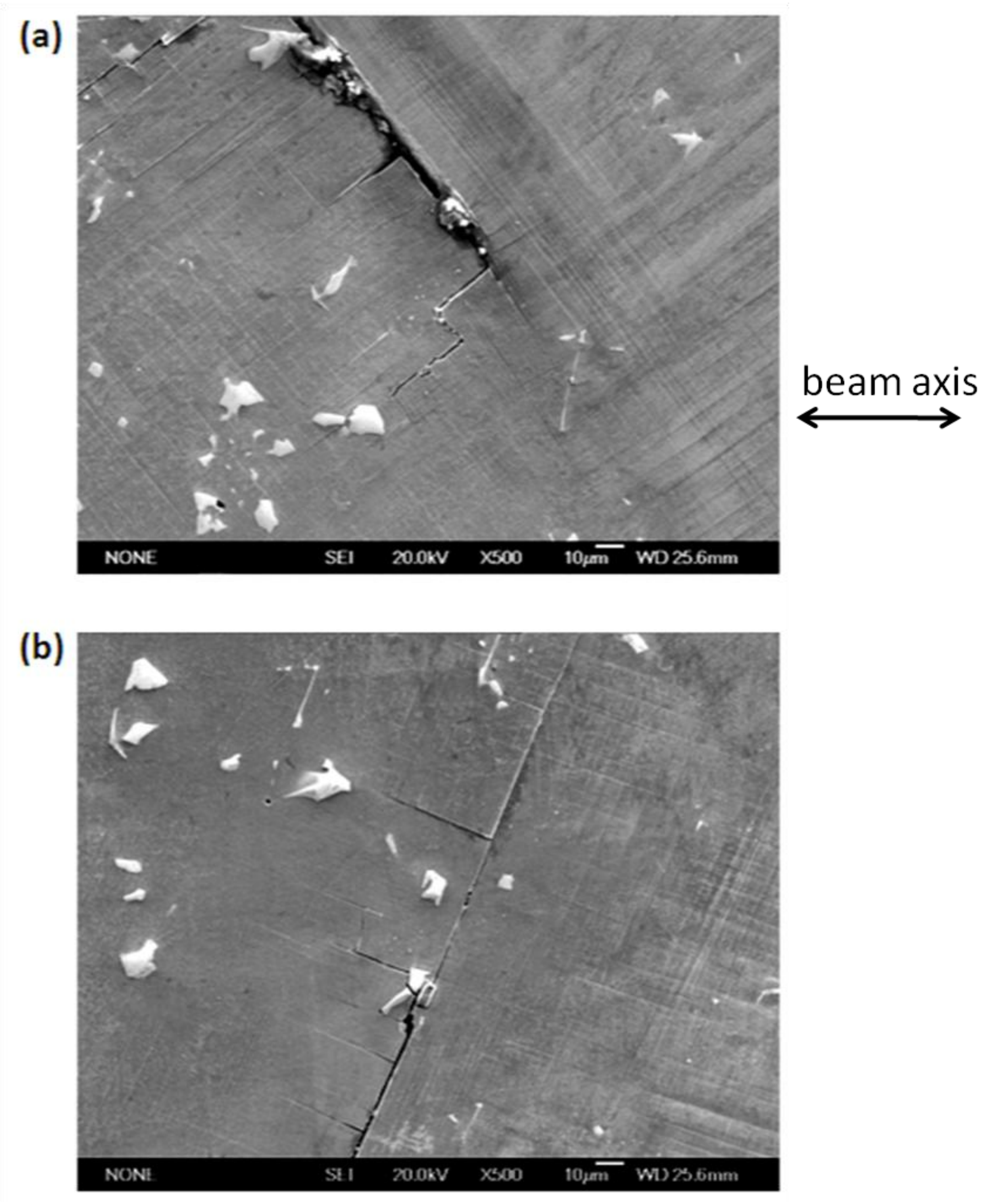

Figure 74. Larger cracks from roller-sample interface in sample P9 after 12000 cycles.

These large cracks proceeded to propagate along the dominant slip direction. However, there are many instances of smaller cracks running along secondary slip systems. The cracks in Figure 74(a) and (b) tended to turn after a while towards the densely populated carbide regions. This may have been due to the higher stresses that were present along those directions. Along the course of the crack, we can also see a zig-zag path, as the crack steps back along the dominant slip direction of that grain.

After another 4000 cycles, two cracks from the roller contacts had grown to large sizes compared to the others in the sample. At 12,000 cycles, these cracks were about 50µm in length and after 16,000 cycles, they have grown to over 200 µm in length and were the dominant cracks.

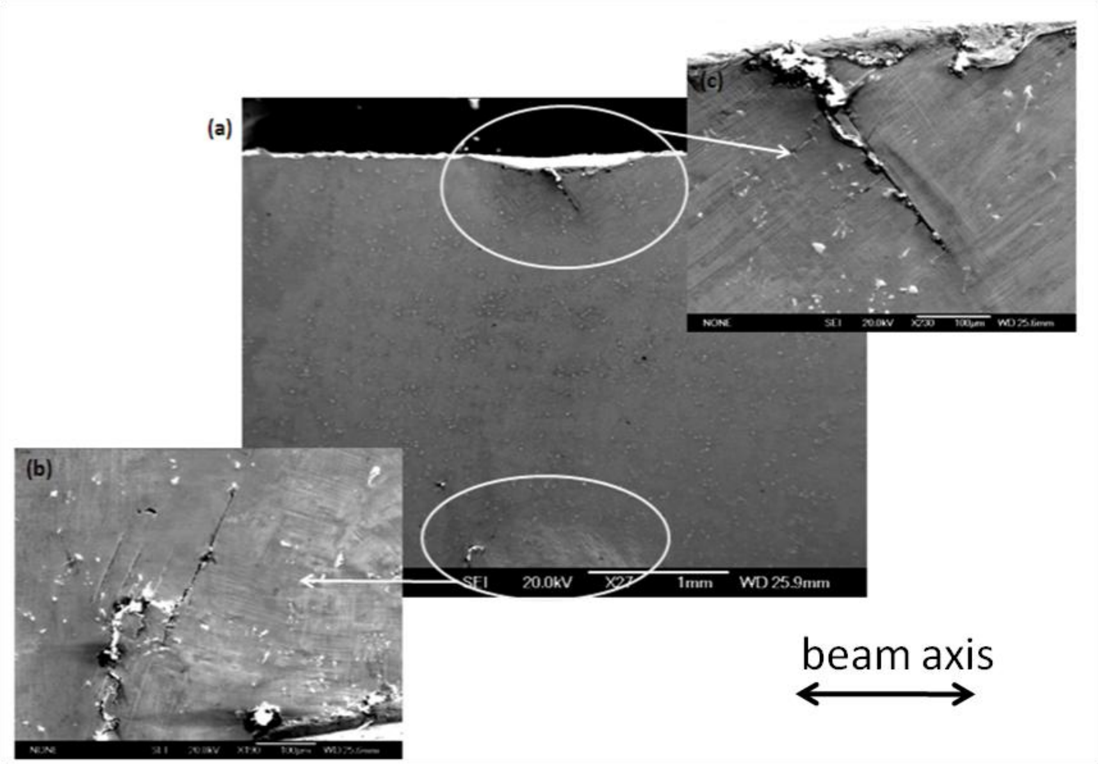

Figure 75. Large cracks from sample P9 after 16000 cycles.

Figure 75(a) shows an SE image of the entire height of the beam sample P9. The circles top and bottom show severe deformation as a result of roller contact. Across the entire size of the beam, there are only 2 clearly visible large cracks over 200µm in length. These cracks are easily visible because of the large crack opening displacement. The areas circled are shown at higher magnification in Figure 75(b) and (c). These cracks have continued to propagate at what is very close to the direction of maximum shear, which would occur at approximately 45° to the lower edge.

Now that the sample has almost reached the end of its fatigue life, it is not unexpected that the propagation of these 2 cracks will ultimately lead to failure of the sample. After the final stage of loading, the sample finally fractured at about 16,650 cycles. The following image shows the fractured surface clearly along the line of the propagating crack.

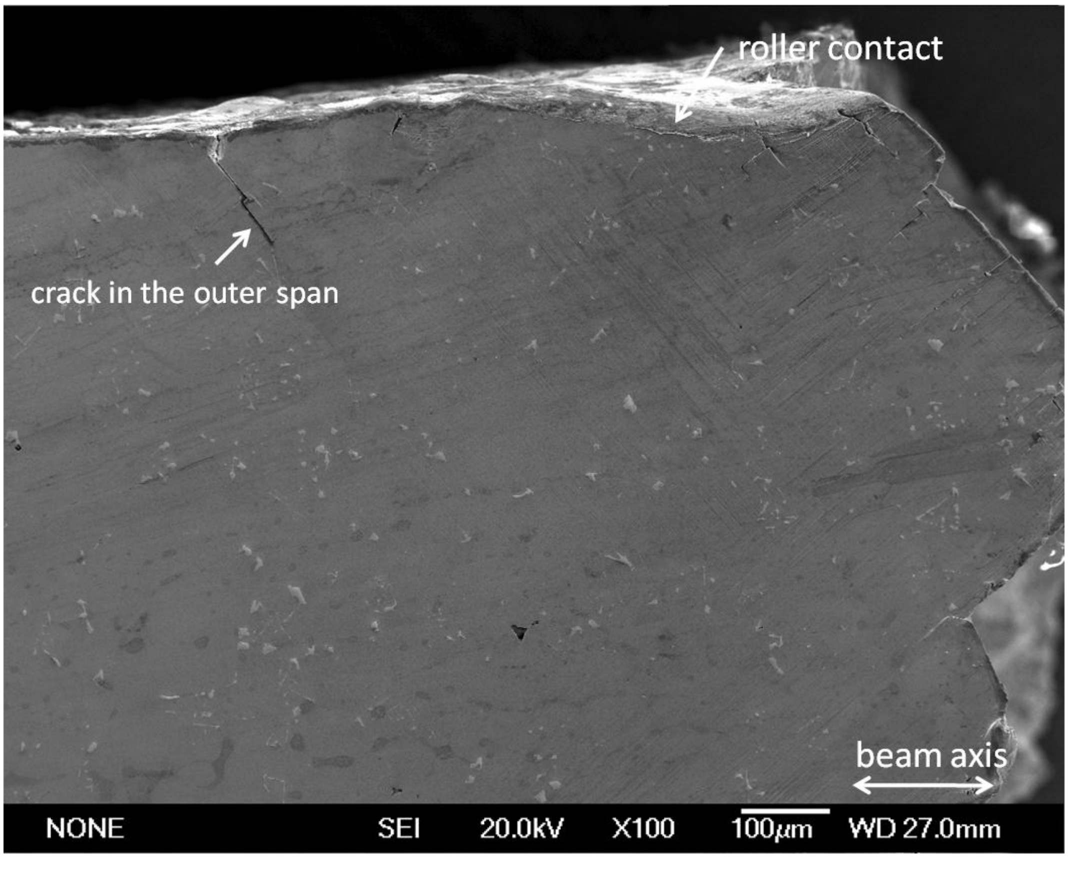

Figure 76. Fracture edges of the sample P9 after 16,650 cycles.

We can clearly see that the main crack continued to propagate alternating between the two clearly visible slip directions at the microscopic scale, whilst taking an average direction almost normal to the loading direction resulting from the 4pt bending at the macroscopic scale. Although some smaller secondary cracks can be seen to have initiated at the top edge, these cracks have not led to the ultimate failure of the sample despite also suffering high stress levels within the test specimen.

Under exactly similar loading conditions, a single crystal sample (S7) was also subjected to cyclic deformation. This sample fractured at 15,900 cycles. A similar trend of crack initiation sites, and crack propagation has been observed in this sample. In both these samples, the majority of crack initiation has occurred within carbides or other particles, but these cracks have been restricted from growing into larger ones. This is perhaps due to the high levels of stress arising in areas near the roller contacts. In case of lower stress level tests (for example high cycle fatigue, and where there are uniform stresses across the samples in tension – tension fatigue), these small cracked carbides may possibly lead to ultimate fracture.

6.3. High-resolution EBSD measurements

As already discussed six areas in the polycrystal sample (P9) were mapped at every interruption during the fatigue life. Three of these areas were mapped around carbide particles and three others away from them. Unfortunately, none of these areas selected have had cracks or cracked carbides included. Thus, the following maps only indicate a general trend of elastic strain, lattice rotation and GND density distribution within other areas of the sample that did not participate in the actual crack formation. The regions in which cracks did initiate have been described later in this chapter.

The following carbide is an example taken from the polycrystal sample P9. The other regions mapped showed a similar evolution with number of cycles. Figure 77 shows the comparison of the 2 normal strain components ε_{11}, ε_{22} and the shear strain component ε_{12} from region near a carbide particle during the fatigue life. This particular carbide has been subjected to a strain amplitude of about 6% in tension and compression, under each cycle of load.

As with all the other maps in previous chapters, the reference pattern was chosen to be at the top-left corner of each map. The reference pattern chosen is obviously not strain-free. As discussed in §5.1, from a simple FE simulation, the local elastic strain components can be found for each mapped region and a constant term added/subtracted to bring the mean values of each measured elastic strain components to the level found in the FEA simulation. This would have ideally preserved the high spatial resolution information from the EBSD measurements of the elastic strain variation. The simplicity of the FE model does not incorporate the cyclic loading conditions. Lack of knowledge concerning the matrix deformation processes involved during the fatigue life (eg. cyclic softening/hardening) have not permitted us from correcting the elastic strain components in this case of cyclic loading.

The strain components around the carbide particle behave nearly in the same manner under cyclic deformation as under monotonic loading. The normal strain ε_{11} along the horizontal x_1 axis is compressive to the left and right of the carbide and tensile above and below it, while the ε_{22} strain along the vertical axis shows strains with the opposite sign. The in-plane shear strain ε_{12} distribution shows maximum positive and negative values at ~+45° and ~-45° around the carbide. As the amount of deformation progresses, slip lines tend to become clearly visible in the elastic strain maps.

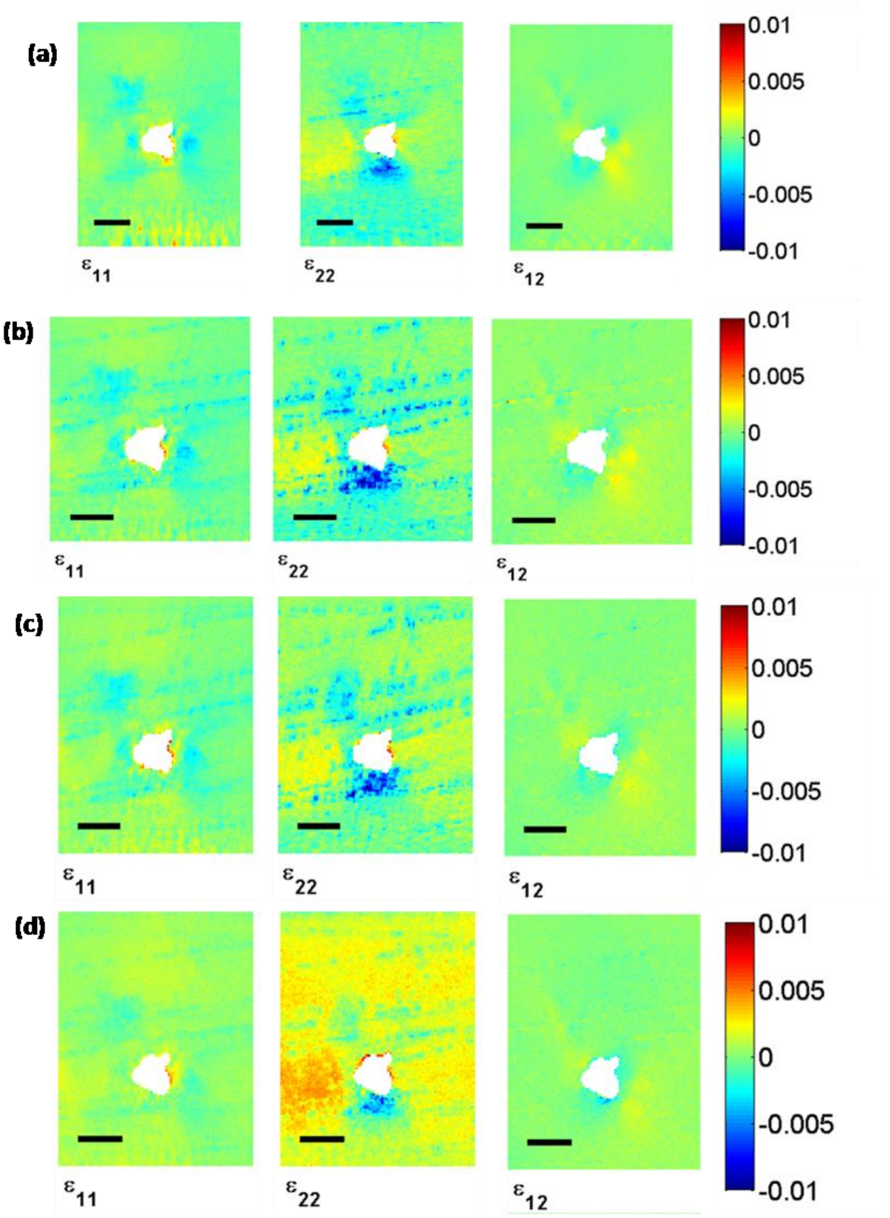

Figure 77. Elastic strain components ε_{11}, ε_{22} and ε_{12} near selected carbide after cyclic loading (a) after 4000 cycles, (b) after 8000 cycles, (c) after 12000 cycles, and (d) after 16000 cycles. The beam axis is along the horizontal x_1 axis.

The variation of the three lattice rotation components are shown below at interrupted stages of fatigue life. The ω_{12} lattice rotations about the x_3 are shown in Figure 78, where large magnitude but quite localised peaks are seen at the edge of the carbide. Rotations about the two in-plane axes also exhibit large magnitudes and extend over larger regions than for the in-plane rotation. The sign of the rotation changes from top to bottom for rotation about the horizontal axis.

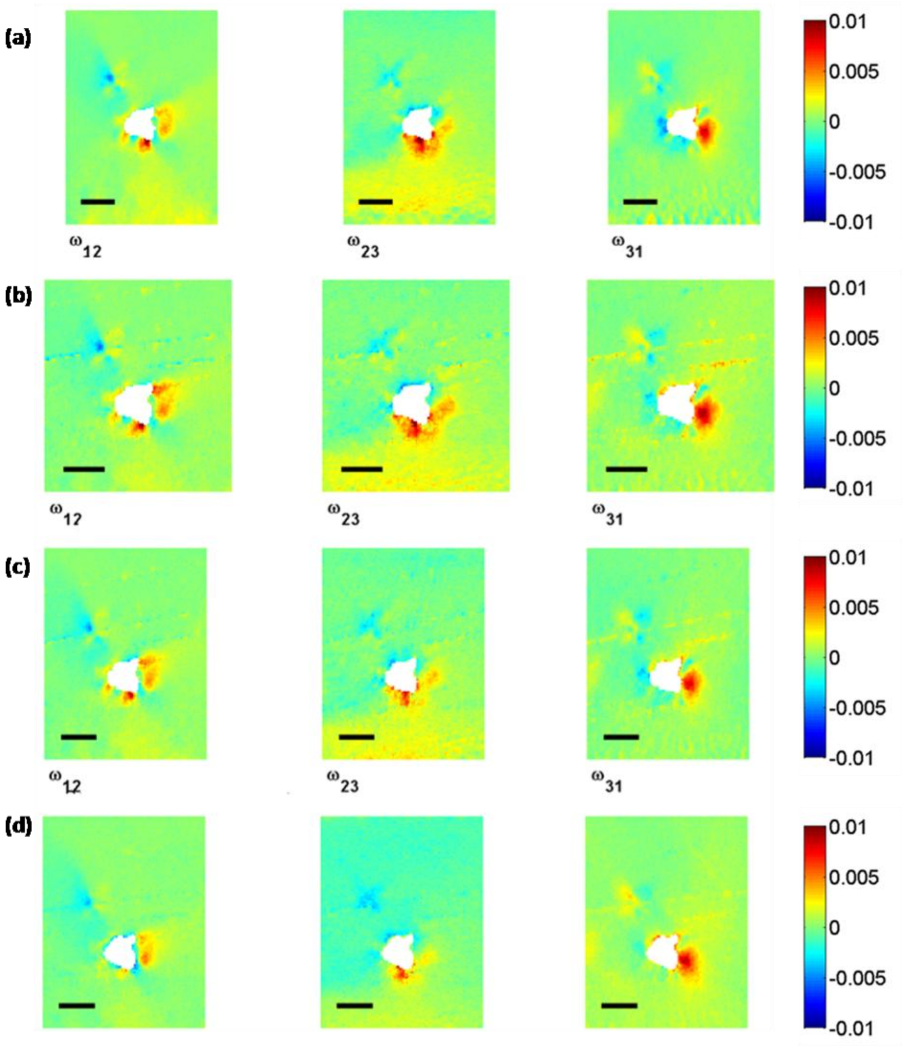

Figure 78. Lattice rotation components ω_{12}, ω_{23} and ω_{31} near selected carbide after cyclic loading (a) after 4000 cycles, (b) after 8000 cycles, (c) after 12000 cycles, and (d) after 16000 cycles. The beam axis is along the horizontal x_1 axis.

6.3.1. Slip features

As already discussed in §4.2.1 using the three lattice rotations components measured by high angular resolution EBSD, six of the nine rotation gradients required to form the Nye's dislocation tensor can be calculated. The remaining three concern variation of the lattice rotations with depth below the surface and are inaccessible. Using these six components it is possible to calculate a lower bound solution to the density of geometrically necessary dislocation densities (GNDs) (see §3.4 for details).

First, some GND maps around the carbide particle from Figure 77 and Figure 78 are presented and after this a statistical view of GNDs both around carbide particles and within the matrix region is given. Figure 79 shows the GND density development around a selected carbide region during the progressing fatigue life. The mapped area from Figure 79 is about 150µm from the final fracture path.

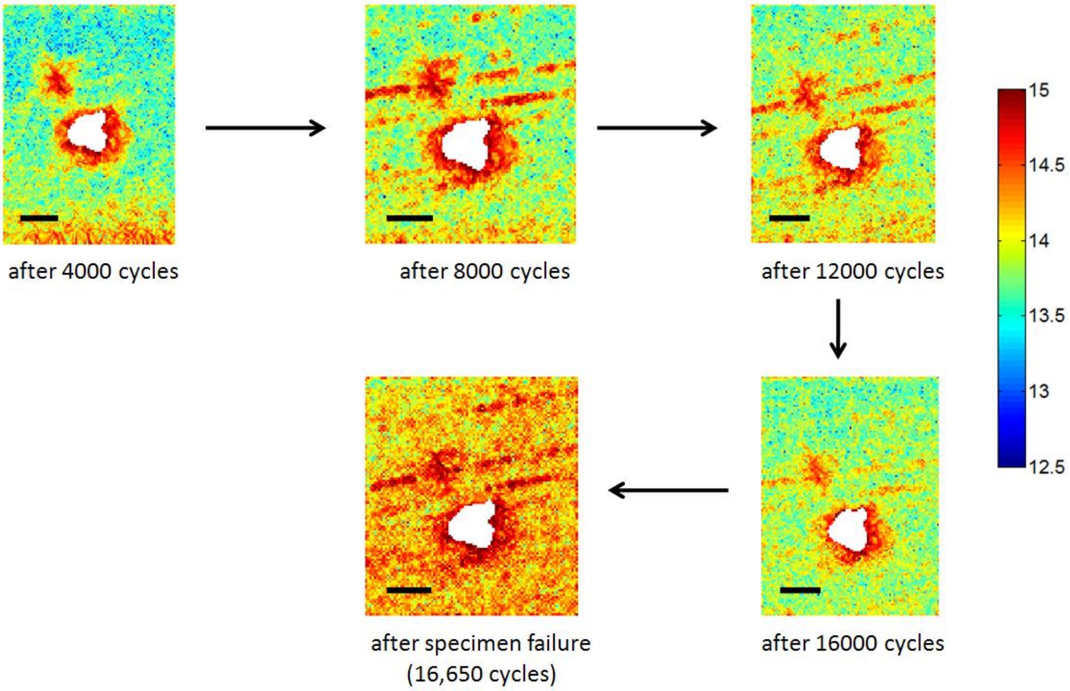

Figure 79. Total GND density distribution around the selected carbide particle in the course of the fatigue life. The scale bars are 5 µm long and the step size is 0.25 µm per pixel. The beam axis is along the horizontal x_1 axis.

It should be noted from Figure 79, that the total GND density distribution first tends to increase around the carbide particle during the first half of the fatigue life (upto about 8000 cycles) and slightly decreases during the next 8000 cycles of deformation. In the final stages of deformation, the GND density again increases around the particle.

From previous discussions, it should to be noted that the GND density does not always increase with applied strain levels. In the case of cyclic loading, there is a very good probability that quite a large number of dislocation sets annihilate together and thus no longer remain GNDs. This could be attributed to one of the causes of the initial increase and subsequent decrease of the GND density during the fatigue life. A similar effect has been observed during deformation of the single crystal sample S7 and also by other members within the research group. Jun Jiang has also observed a very similar trend in the GND density variations through the fatigue life of polycrystal Copper samples. Also, another point to note is that the GND density depends crucially on the length scale (or patch size) of the assessment. This EBSD analysis uses a microscopic viewpoint using an array of points separated by about 250 nm. Hence, there is also a possibility that quite a lot of dislocation sets might have been lost in count at this length scale of measurement.

The plot in Figure 80 shows the average GND density data values around (within about 2-3 µm of the carbide particle) the measured three carbide particle during the fatigue life. Carbides 1 and 3 have been subjected to a strain amplitude of about 6% in compression and tension during each fatigue cycle. Carbide 2 is present midway across the height of the beam, and so experiences a much reduced strain amplitude.

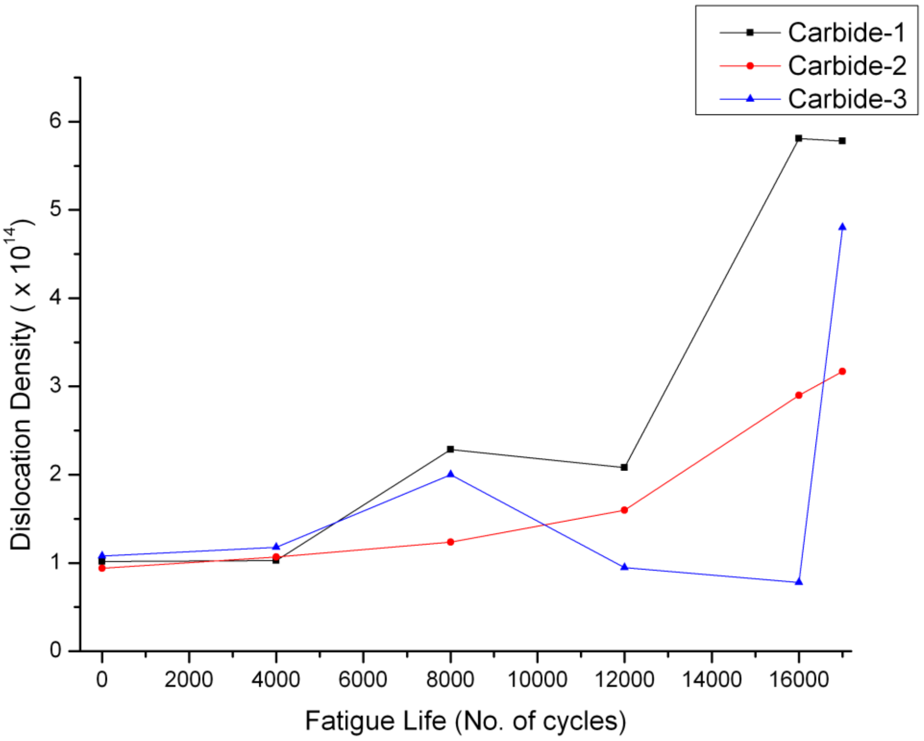

Figure 80. Average GND density distribution in the plastic zone areas around the three carbide particles from sample 'P9'.

Similar to the sample P9, six such areas have been mapped in the single crystal sample S7. Figure 81 shows the variation of GND density around one such carbide from the sample S7 and how it evolves during the fatigue test. The location of this selected carbide is in a region where a mechanical strain of about 5% is imposed in tension and compression in each cycle of load.

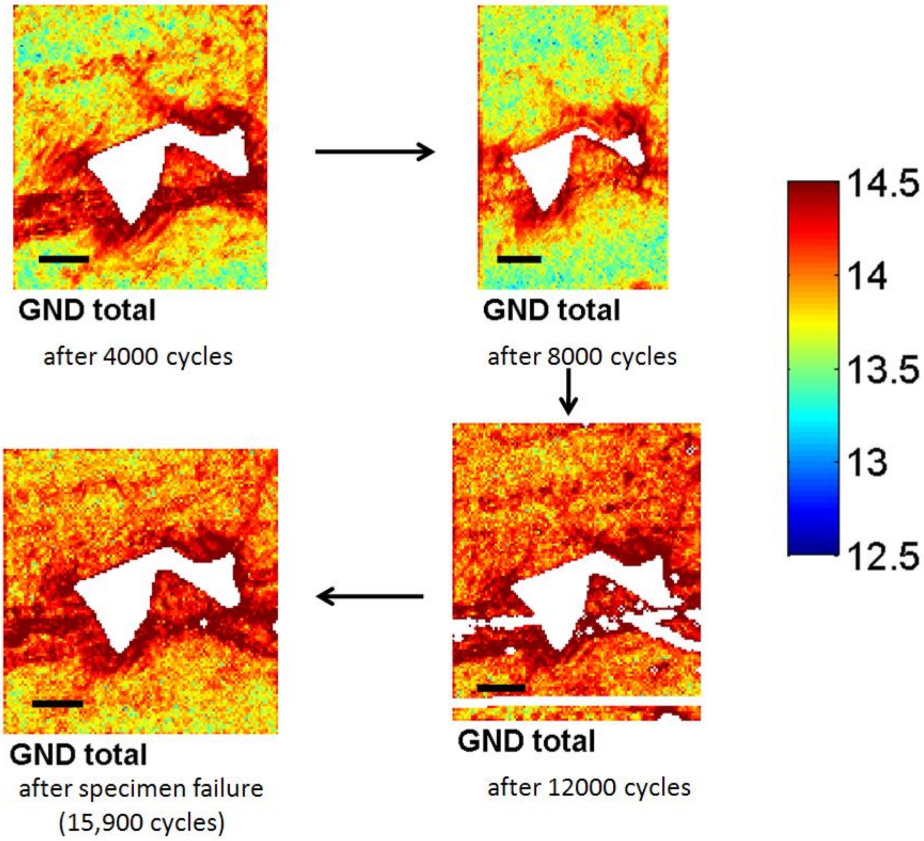

Figure 81. Total GND density distribution around the selected carbide particle from sample S7 in the course of the Fatigue life. The scale bars are 5 µm long and the step size is 0.25 µm per pixel. The beam axis is along the horizontal x_1 axis.

The average GND density measured after 4000 cycles and 8000 cycles is about 2 x 10^{14} m^{-2} around the carbide particle, after which the density tends to increase to about 4.5 x 10^{14} m^{-2} at specimen fracture.

Within the matrix, three areas were mapped in both the single and polycrystal samples in the course of the fatigue deformation. Figure 82 shows the variation of the average GND density with increasing number of cycles throughout the test to failure. Similar to what is observed in regions around carbide particles, the average GND density tends to increase in the initial half and then tends to decrease. In general, the average GND density tends to be lower that what is observed around carbide particles.

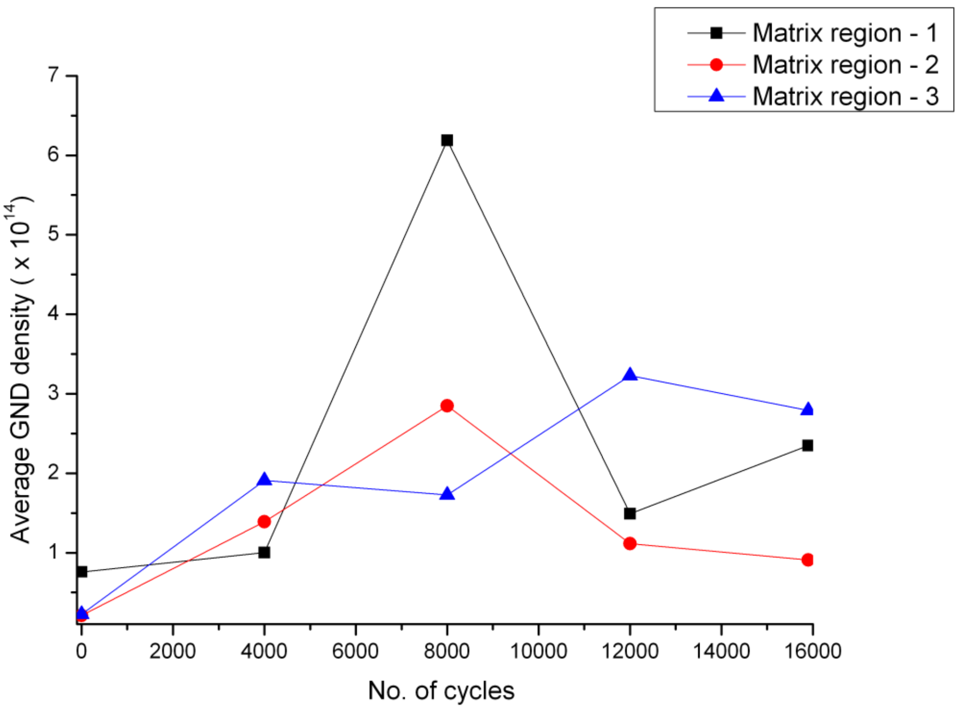

Figure 82. Average GND density distribution in areas away from the carbide particles from sample 'S7'.

The matrix regions 1 and 3 are those closer to the edges of the specimen, and were subjected to a strain amplitude of about 5% in tension/compression in each cycle. The region 2 is closer to the neutral axis of the beam, where the imposed strain amplitude is less than 1%. An interesting observation to note in GND data split into individual systems in that, unlike the monotonic deformation, there are no clear alternating patterns of dislocations accumulating along the slip lines. In almost of these maps, they are rather disordered, possibly owing to the nature of cyclic deformation. An example from the selected carbide from sample P9 is shown in Figure 83.

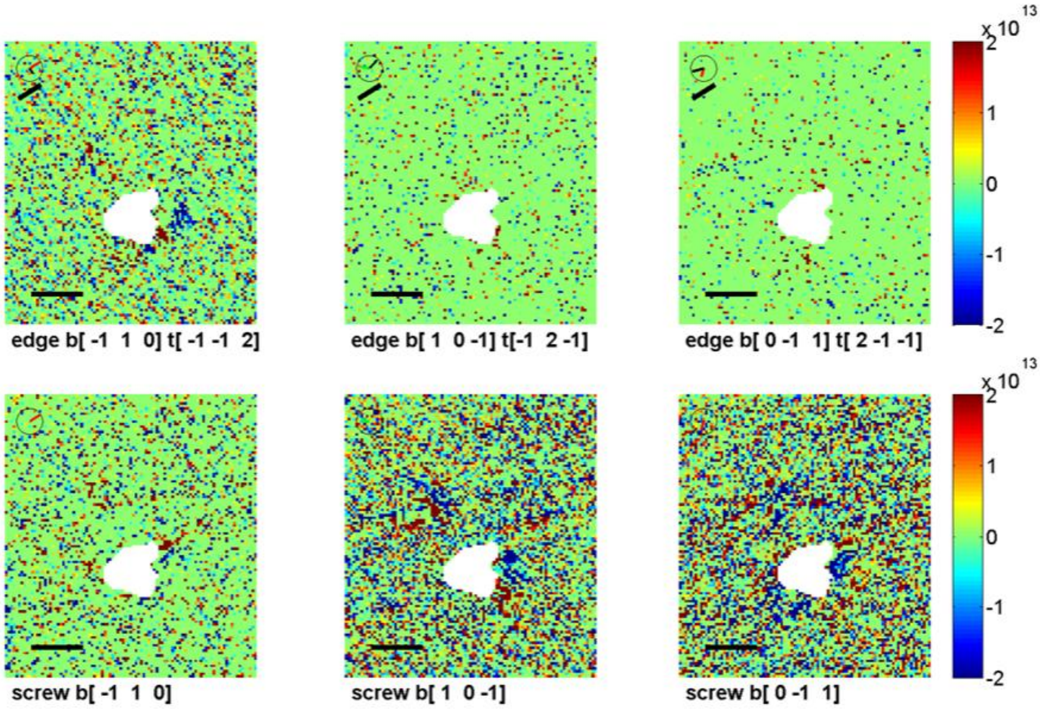

Figure 83. A set of 6 dislocations (deconstructed from total GND density) for the carbide from sample 'P9', depicted in Figure 79, after failure at 16,650 cycles. The beam axis is along the horizontal x_1 axis.

In all the areas mapped in these 2 samples P9 and S7, no cracks formed during fatigue testing. In order to estimate the strains and GND densities around a cracked region, another area from the sample S7 has been mapped. A few areas surrounding a couple of cracked carbides were mapped in the failed samples. One such area is shown below. In Figure 84 the cross-correlation peak height map and the mean angular error maps show an approximate impression of the carbide and the crack.

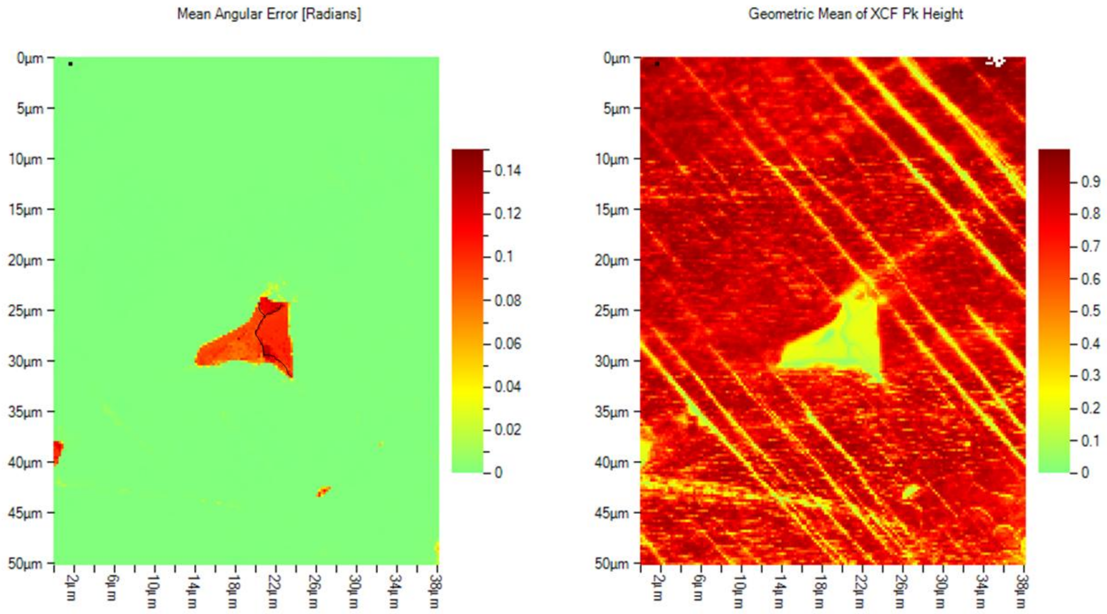

Figure 84. Cross-correlation peak height and mean angular error (rads) around a cracked carbide particle from sample S7 after failure at 15,900 cycles. The crack within the carbide has been falsely highlighted in the mean angular error map and can be faintly seen in the cross-correlation peak height map. The beam axis is along the horizontal x_1 axis.

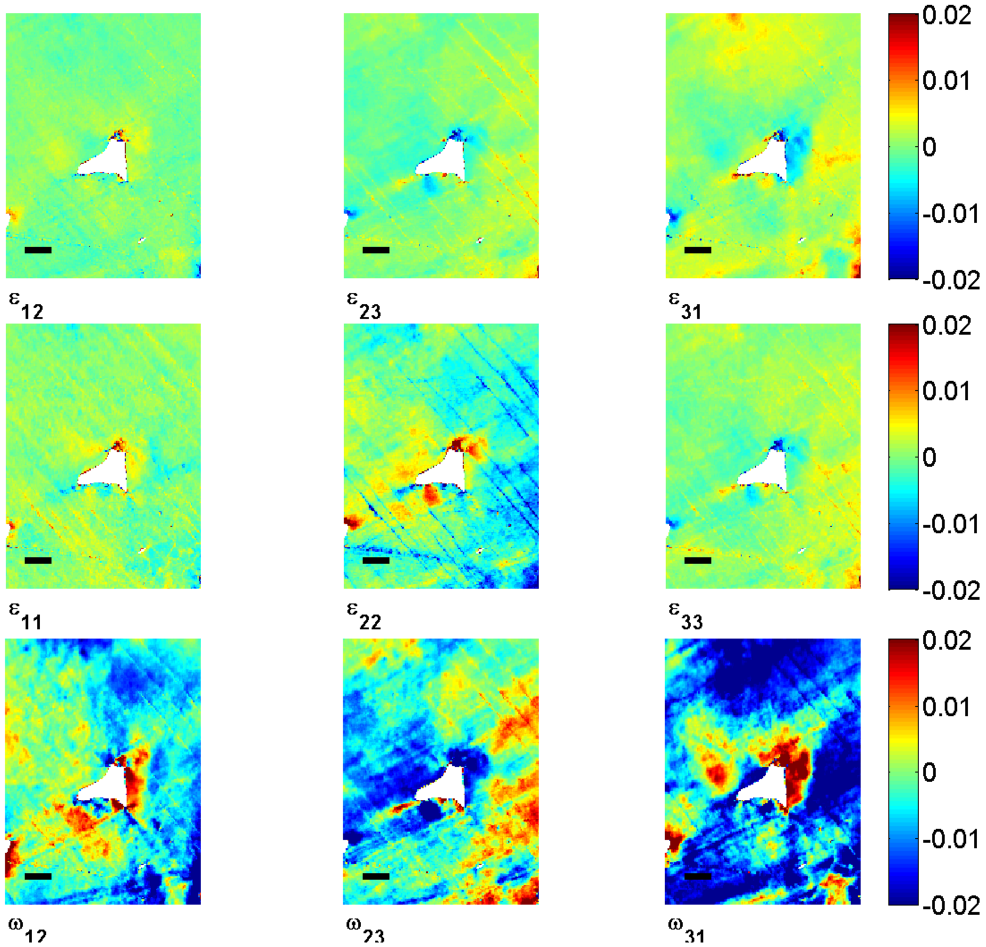

Figure 85. Elastic strain and rotation components around a cracked carbide from sample S7 after failure at 15,900 cycles. The beam axis is along the horizontal x_1 axis. The region experienced a strain amplitude of ~5% in each cycle of tension/compression.

Figure 85 shows the rotation and elastic strain variations near this carbide. Just like all the other sets of maps, the rotation maps are of a large magnitude but quite localised peaks are seen at the edge of the carbide. Rotations about the two in-plane axes also exhibit larger magnitudes than the in-plane rotation. It can also be seen that near the cracked edge of the carbide (towards the lower edge of the carbide), the in-plane rotation term in the matrix, tends to have an alternating orientation on either sides of the crack.

The GND density measured around the cracked carbide also tends to be very high, which in not unexpected. These cracks in the matrix are basically cleavage along slip planes and thus tend to have quite high lattice rotation components and hence such high GND densities. The average GND density in this area is close to ~8 x 10^{14} m^{-2}.

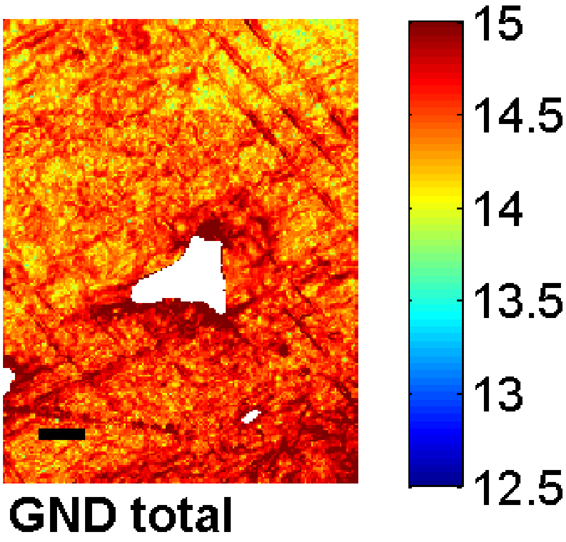

Figure 86. Total GND density distribution around the cracked carbide particle from sample S7 after failure at 15,900 cycles. The scale bar is 5 µm long and the step size is 0.25 µm per pixel.

As already discussed the individual GND density maps have a rather jumbled arrangement of positive and negative GNDs. Unlike the monotonic deformation, these do not follow an alternating pattern of arrangement. For the cracked carbide shown in

Figure 84, the slip bands/steps can be seen most clearly in the peak height map. These steps are also clearly evident in the subsequent elastic strain and rotation maps (Figure 85) and in the total GND density map (Figure 86). The individual GND density distribution for this carbide is shown below in Figure 87. The slip features seen on the sample surface are not as clearly seen in the individual GND density maps, while they had been clear in monotonic deformation.

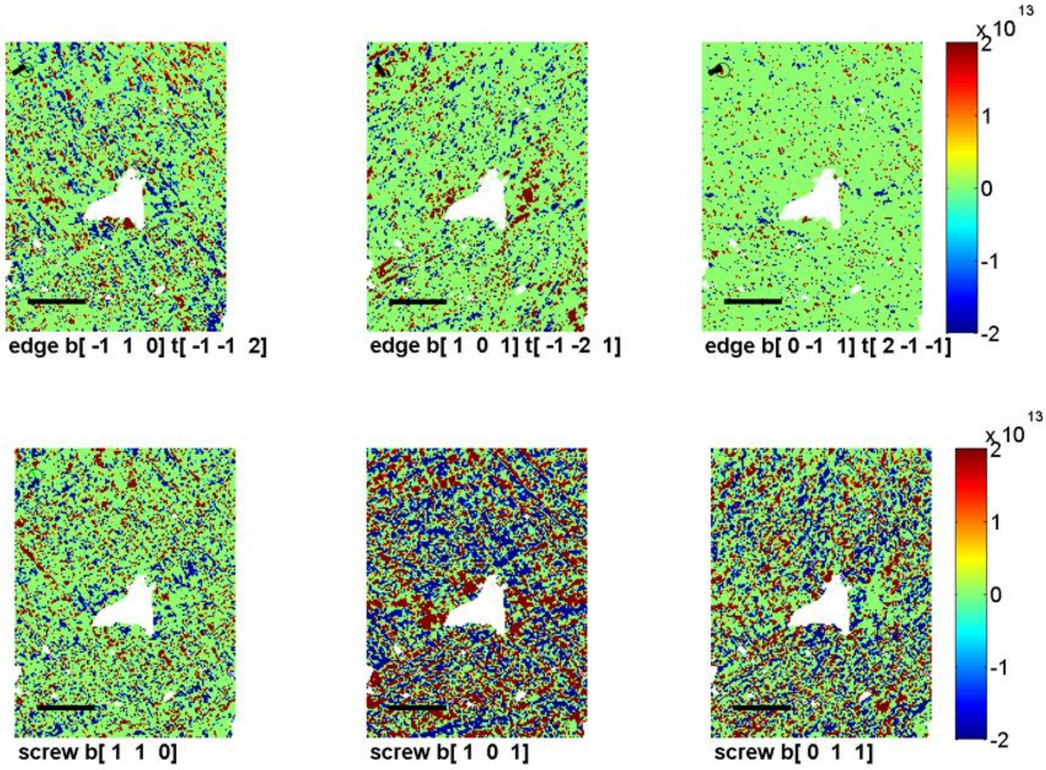

Figure 87. A set of 6 dislocations (deconstructed from the total GND density) for the carbide from sample 'S7', depicted in Figure 84, after failure at 15,900 cycles.

6.4. GND accumulation near grain boundaries

The very large grain size of the polycrystal samples posed problems in mapping full grains. As a result, only measurements were made at a couple of grain boundaries, within the polycrystal sample after failure. In the case of more than one reference grains, the cross-correlation software v3 computes the entire area for each reference and then combines the results together for the complete field. Figure 88 below shows the standard set of cross-correlation peak height and mean angular error maps. The elastic strain and lattice rotation maps follow later on.

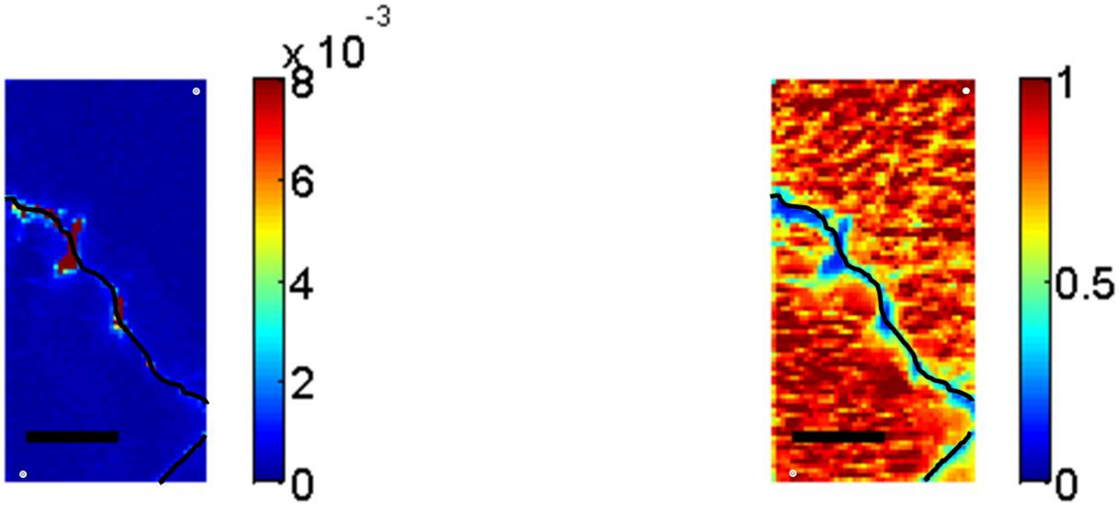

Figure 88. Mean angular error (rads) and cross-correlation peak height across a grain boundary from sample P9 after failure at 16,650 cycles. The local strain amplitude in this region is ~3% in each cycle of tension/compression. The scale bars are 5 µm long and the step size is 0.25 µm per pixel.

The locations from which the reference EBSD pattern in each grain were obtained are highlighted in white in Figure 88 at the top right and bottom left corners of the maps. As expected the mean angular error is high at points on grain boundary which are decorated with carbide particles and the peak-height is low as 0.4. Along the grain boundary, in regions where the patterns from the two grains overlap, the peak-height also tends to be as high. For this reason, the minimum peak-height tolerance was set to about 0.5. The data points (pixels), whose peak-height value falls below this tolerance have been removed from the subsequent elastic strain and lattice rotation maps, which are shown in the following figures.

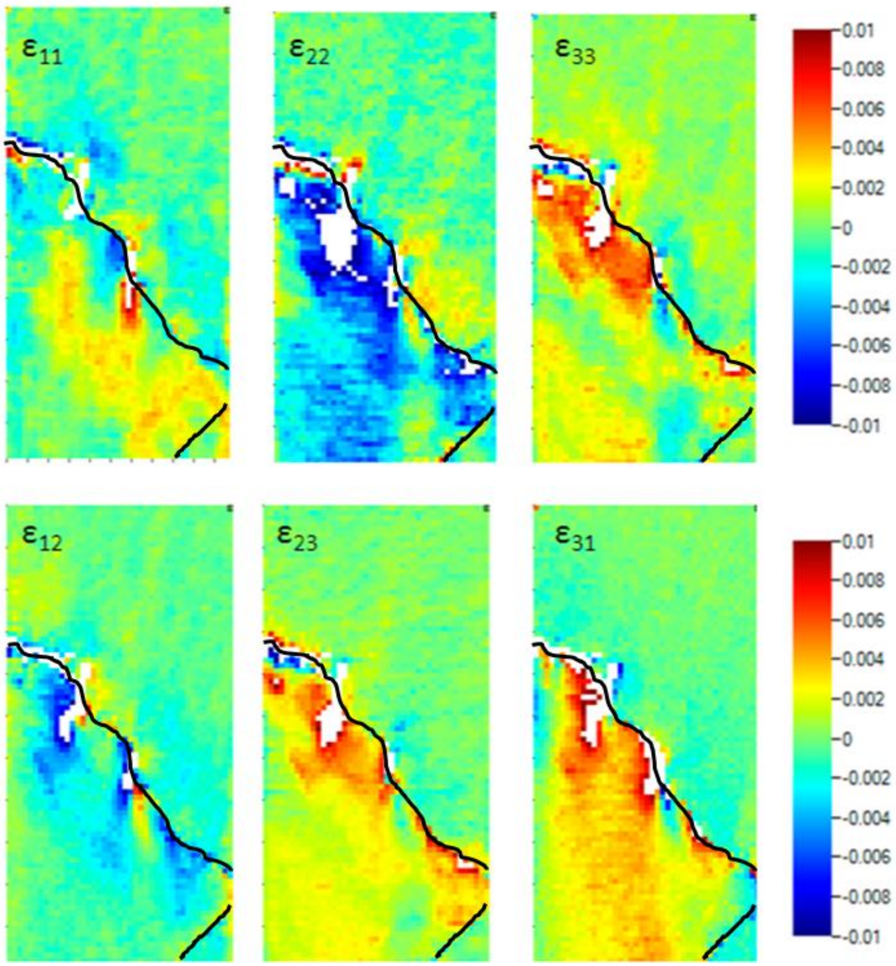

Figure 89. Elastic strain components along a grain boundary from sample P9 after failure at 16,500 cycles.

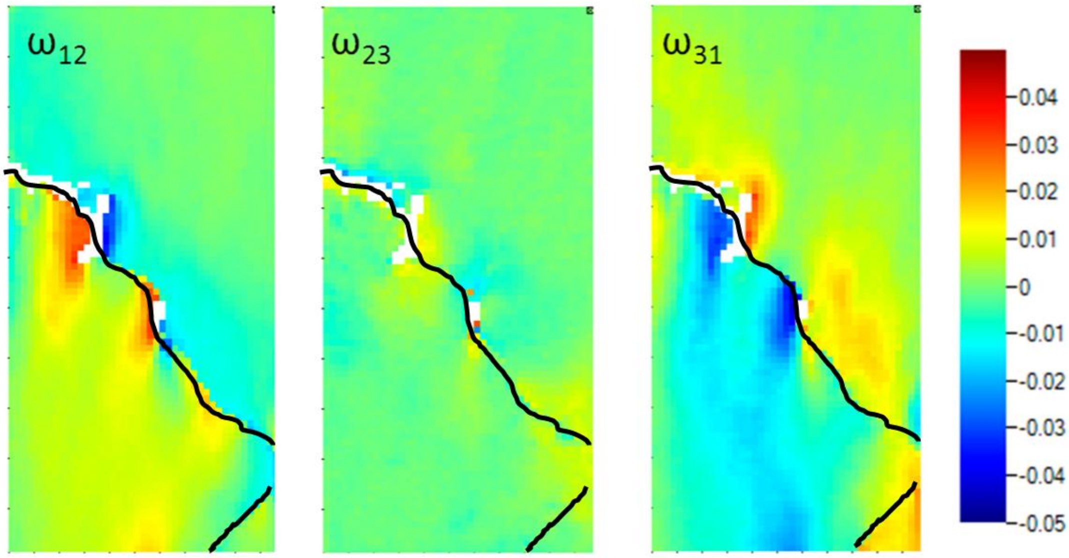

Figure 90. Lattice rotation components along a grain boundary from sample P9 after failure at 16,500 cycles.

Like in all the other deformation maps, the lattice rotation components are very high compared to the elastic strains. Although they extend well into the grains, there are quite localised peaks near the grain boundaries. The rotations appear to be most marked in regions of the grain boundary that are decorated by carbide particles.

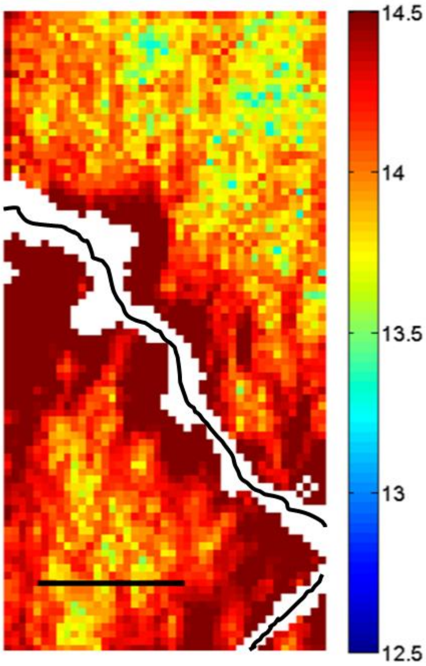

Figure 91. Total GND density distribution around the grain boundary from sample P9 after failure. The scale bar is 5 µm long and the step size is 0.25 µm per pixel.

Clearly there is GND accumulation along the grain boundary. The GND values near the grain boundary are as high as 5 x 10^{14} m^{-2}. Most of the grain boundary area is covered with smaller carbide particles that have settled along this boundary during the directional solidification of this material. The secondary electron images (Figure 92) of some areas in this sample P9 clearly show this settlement.

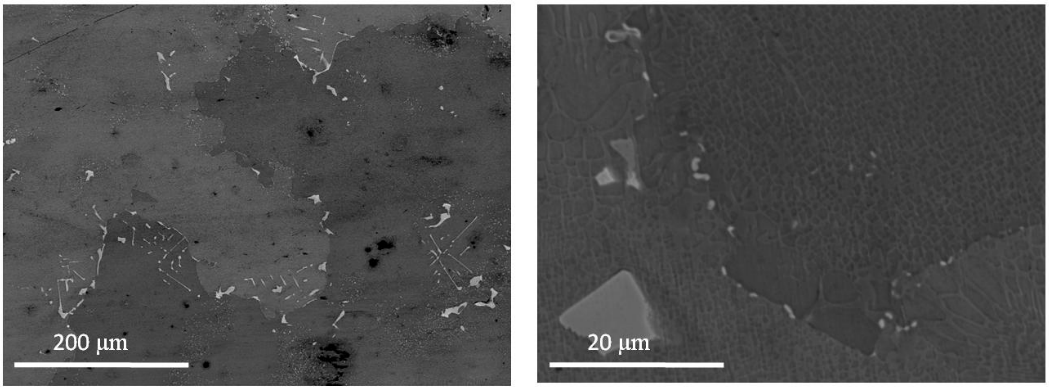

Figure 92. SEM images of grain boundaries in sample P9, showing smaller carbide accumulation along the boundaries.

The GND accumulation shown in Figure 91 is thus a result of accumulation along the grain boundary and also around smaller carbide particles that pin them.

None of the carbide particles selected in this sample for study through fatigue life were crack initiation sites. This problem, although very common for these types of studies could have been improved by a better sample design. From Figure 66, it is very clear that the test piece geometry in not very ideal for a simplistic study. Clearly, there are large plastic hinges in regions close to the rollers. The rollers imposed very severe and localised plastic loading in the sample. Ideally tensile loading would have been a better loading method, but the size of the samples prevented from building the required loading rig.

The simple FE model used to correct absolute elastic strains does not reflect the loading conditions well enough in this case of cyclic loading. The effects of cyclic hardening/softening have not been incorporated within this simple model. Thus, with the limited analysis of just the EBSD measurements, it is not possible to follow the absolute strain (and hence stress) evolution. However, the spatial variation in the measurements is still well preserved by these experimental measurements. Thus, the mean strains for EBSD cannot be set from the simple FE model that was employed in the case of monotonic loading.

The high-resolution EBSD technique is currently improving to resolve the need for a strain-free reference pattern. Several strain measurement techniques; viz. X-ray and neutron diffraction suffer from a similar problem with the need for stress free lattice parameters. New trials with the HR-EBSD technique involve the use of a simulated reference pattern (strain-free) to essentially remove the effect of the strains, so that the absolute elastic strains can be well measured.

From the observations made under cyclic loading, the GND densities near the carbide particles seem to increase near the end of fatigue life. This effect is not seen in regions away from the carbide. In fact, in most measurements, the GND density first increases and then tends to decrease during the course of fatigue life of a sample.

7. Conclusions

Conventional Hough-based EBSD analysis is well established as an indispensable method for the characterization of grain size, texture, grain boundary type distributions polycrystalline microstructures. The cross-correlation-based analysis of EBSD patterns provides a step change in the sensitivity of the technique and opens up important new possibilities in local deformation studies, but also raises new challenges. High resolution EBSD provides a useful bridge between x-ray and neutron techniques on the one hand and the very localised transmission electron microscope methods one the other.

The cross-correlation based high resolution electron backscattered diffraction (HR-EBSD) technique has been presented in §2.5. This technique has been successfully employed here to explore deformation. Most of the examples shown in this thesis here illustrate the considerable potential of the method for studying structural metallics. The main strengths of the technique are (i) that all components of the 3D strain and rotation tensors are obtained in parallel, (ii) the use of an electron beam allows very small volumes of material to be probed, and (iii) the equipment required is rather widely available. The detailed information on the 2D maps showing strains and lattice rotations can be acquired with 1-2 hours of SEM time.

After pattern acquisition, post processing can be performed on any daily usage PCs. At present, the most common comparison is between 20 256x256 pixel ROI on each pattern. On a single core computer, the comparison between ~10,000 patterns takes about 15 hours. Faster performance has been achieved using multiple cores and the time reduced to about an hour.

Measuring zone axis shifts, as performed with HR-EBSD, is insensitive to hydrostatic dilation of the crystal and as such the assumption that $\sigma_{33}=0$ is required to separate the normal strain components. In theory, this condition assumes that the surface of the specimen is flat and that the x_3 axis points directly perpendicular to the sample surface, which may not be true when there are significant out of plane displacement. However, the EBSD measurements come from only a small volume (typically less than about 50nm) from the sample surface and thus this assumption is pretty much valid in most cases. Using the deformation fields from HR-EBSD, a novel analysis to study the stored dislocation content using an L_1 based minimisation of the dislocation line energy has been developed.

The first example presented is a case of thermal deformation in a Nickel based superalloy. Significant thermal elastic strains (and stresses) are induced as the Ni–matrix contracts around the sizeable carbide particles present in this alloy, as a result of regular heat treatment processes. The magnitudes of these strains are $\sim 10^{-3}$ in accord with simple estimates and to first order the strains are consistent with contraction of the matrix around a rigid particle, though the irregular shape of the carbides generates considerable perturbation of the fields expected for a cylindrical particle. The misfit is sufficient to cause localized yielding in the matrix as demonstrated by raised GND densities close to the carbides.

A systematic study of the strain and lattice rotation components has been presented. Later, the GND density estimation in regions close to the carbide particles and in regions away from them has been presented. The experimental measurements have been used to compare with a novel crystal plasticity finite element model, currently being developed by Prof. Fionn Dunne's group in the Department of Engineering Science, Oxford University. The current stage of the simulations has been restricted to estimating strains, rotations and GND densities after a thermal loading case. Improvements are currently underway to develop the model to 3-dimensional problems involving mechanical deformation.

The second case involves study of residual deformation (in terms of elastic strain and storage of GNDs) using the HR-EBSD method in the sample set of samples after mechanical deformation in the form of three point bending. This mechanical deformation at room temperature has been accommodated by highly planar slip on multiple systems as expected for the superalloy. EBSD measurements showed local stress fluctuations of 100–200MPa, which occurred across two sets of parallel linear features corresponding to slip steps. GNDs were shown to be stored along the linear slip features at densities of more than 10^{14} m^{-2}, with the sign of the excess dislocation type frequently alternating across a sequence of parallel features. Strain gradients generated by the rigid carbide particles were accommodated by significantly increased GND content in the surrounding matrix.

Several particles were picked prior to mechanical deformation and then the GND densities compared with those areas after bending. As a result of bending there is a high level of imposed strain (and stress) across the height of the beam. The average GND densities have been recorded and has been demonstrated that it increases with magnitude of the local strain imposed.

Unfortunately, the measurement of absolute strain (as in the case of thermal loading) is not trivial in the most general case. For the thermal loading case a good reference pattern can be obtained by moving the electron probe to a significant distance from the carbide particle where the strain will have fallen to very low levels. The reference pattern used for comparison has to be essentially strain-free. In situations where the entire field or sample has an unknown strain state, such as after macroscopic plastic deformation, it is not possible to determine unambiguously the absolute strains. The reference pattern issue has many parallels with the need for stress free lattice parameters in x-ray and neutron diffraction studies (referred to as the d_0 problem).

A simple scheme to correct the reference strain problem has been shown here. By using a basic finite element model to estimate the local strain in the measurment area, this problem can be overcome to an extent. The measured strain components can be offset up or down to this average value provided from the finite element simulation. The use of a simulated pattern is a much sought after solution to such a problem. The factors affecting the accuracy of HR-EBSD when using simulated patterns and the difficulties have been discussed by Britton et. al. [100]. In order for the simulated patterns to be used, knowledge of the detector geometry has to be sufficiently accurate.

Errors in determining the geometry lead to systematic errors in the strain and rotation tensor that can be as large as 10^{-2} in some components. Several groups are actively pursuing methods for significantly improving the experimental calibration of the EBSD detector geometry.

The HR-EBSD based approach of estimating the geometrically necessary dislocation (GND) content considers the change in the lattice rotation field (lattice curvatures), which can be calculated directly from the pair wise comparison of diffraction patterns. Thus, the GND estimation used in this technique is not actually influenced by the unknown strain in the reference pattern.

After monotonic deformation, a different set of Nickel superalloy samples have been subjected to cyclic loading. Initially, microscopic examination of the formation of slip lines, carbide cracking and the final crack formation has been presented. Dislocation storage has been examined around carbide particles and also in regions away from any visible particles at intervals during the Fatigue life. The GND content around carbides and in the matrix regions tends to increase during the first half of the fatigue life and later tends to decrease.

This study so far has been practical to visibly quantify deformation processes occurring due to thermal loading, monotonic loading and cyclic loading. The measurements after thermal treatment have been made to illustrate the inherent elastic strain/dislocation content in the material even before the material is put into service.

The level of strains signifies that a small area around carbide particles is already in a plastically deformed state, even before its first practical employment.

Under monotonic deformation, the sample had been deformed to over 10% strain and so plastic deformation is extensive. This is reflected in the EBSD data by the fact that the rotations are much bigger than the elastic strain variations within the grains (around carbides and also away from them). This fact has been used to analyse the dislocation structure using the GND analysis of Nye. It has been observed that the GND density increases with imposed strain under monotonic deformation. Upon deconstruction into individual slip systems that are prominent in *fcc* Nickel, it can be seen that there are alternating patterns of positive and negative dislocations associated with monotonic bending. There are also some dislocation types that do not take part (or less actively take part) than the others.

In the cyclic loading case, the crack development has initially been studied along the course of the Fatigue life. Crack initiation sites and the crack paths have been clearly marked out by means of an interrupted study. The elastic strain and/or residual stress plots (in both monotonic and cyclic loading) are most useful to establish the most likely stress concentration areas and thus determine any changes/deviations in crack paths that might occur during service. Under cyclic loading, such deviating crack paths have been shown in this study and predicting the crack path in an in-service alloy would be most useful. Again, upon deconstruction into individual sets of GNDs in *fcc,* it can be seen that not all dislocation types are actively involved in the cyclic mode of deformation. Unlike the monotonic bending, the dislocations are rather disordered possibly owing to the nature of cyclic deformation. High GND density near the grain boundaries is expected as a result of dislocation glide across the grain interiors to form pile-ups and accumulation of density near the grain boundaries.

None of the carbides selected in this study have been sources of crack initiation. Although not accomplished in the current study, HR-EBSD can thus be used to estimate the amount of elastic strains and lattice rotations (and hence GND density) around cracked carbide regions and/or grain boundaries, so that an assessment can be made as to whether the points of interest may be sources for new cracks.

The presence of high GND density implies that the interaction volume contains either a large number of defects or severe elastic gradients, which generally reduce the overall contrast from the patterns. Apart from the quality of diffraction patterns affecting the analysis, the resolution of the rotation field in combination with the step size chosen is quite important. Care has to be taken to select an appropriate step size so as to spatially probe the beam on the interaction area with enough resolution to consider as many of the dislocations as GNDs.

Studying polycrystalline and indeed multiphase materials provides some additional challenges, such as pattern overlap near grain and phase boundaries and the need to use multiple reference points so as to analyse data on a grain by grain basis and then recombine for the total field.

Thus, the high resolution electron backscattered diffraction based technique has proved quite useful for the study of plasticity in materials for use in real engineering application. It provides a step change in the resolution of elastic strain and lattice rotation components, and probing the stored dislocation content at a length scale that bridges X-ray and TEM measurements. It has also been shown that the results from this technique provide a source of validation and help in the development of physically based models.

References

[1] C. T. Sims, N. S. Stoloff, and W. C. Hagel, *Superalloys II*. New York□; Chichester: Wiley, 1987, p. xx, 615 p.

[2] W. Betteridge and S. W. K. Shaw, "Development of superalloys," *Materials Science and Technology*, vol. 3, no. 9, p. 13, 1987.

[3] R. C. Reed, *The superalloys□: fundamentals and applications*. Cambridge: Cambridge University Press, 2006, p. xiv, 372 p.

[4] M. Durand-Charre, *The microstructure of super alloys*. Amsterdam: Gordon & Breach, 1997, p. 150 p.

[5] A. J. Wilkinson, G. Meaden, and D. J. Dingley, "High-resolution elastic strain measurement from electron backscatter diffraction patterns: New levels of sensitivity," *Ultramicroscopy*, vol. 106, no. 4-5, pp. 307-313, 2006.

[6] A. J. Wilkinson, G. Meaden, and D. J. Dingley, "High resolution mapping of strains and rotations using electron backscatter diffraction," *Materials Science and Technology*, vol. 22, no. 11, pp. 1271-1278, 2006.

[7] J. F. Nye, "Some geometrical relations in dislocated crystals," *Acta Metallurgica*, vol. 1, no. 2, pp. 153-162, 1953.

[8] F. P. E. Dunne, D. Rugg, and A. Walker, "Lengthscale-dependent, elastically anisotropic, physically-based hcp crystal plasticity: Application to cold-dwell fatigue in Ti alloys," *International Journal of Plasticity*, vol. 23, no. 6, pp. 1061-1083, 2007.

[9] S. Suresh, *Fatigue of materials*, 2nd ed. Cambridge: Cambridge University Press, 1998, p. xxi, 679 p.

[10] G. E. Dieter and D. J. Bacon, *Mechanical Metallurgy*, SI metric. London: McGraw-Hill, 1988, p. xxiii, 751 p.

[11] M. A. Meyers and K. K. Chawla, *Mechanical behavior of Materials*. Cambridge University Press, 2008, p. 880.

[12] O. H. Baskin, "The exponential law of endurance tests," *Am Soc Testing Mater*, vol. 10, pp. 625-630, 1910.

[13] J. J. Reed, N. L. Weiss, and V. (Ed] Burke, *Fatigue: an Interdisciplinary Approach (Proceedings of the Tenth Sagamore Army Materials Research Conference)*. Syracuse University Press, 1964.

[14] J. Goodman, *Mechanics applied to engineering*. Longmans, Green & co., 1919, p. 854.

[15] W. Z. Gerber, “Calculation of the allowable stresses in iron structures,” *Z. Bayer Archif Enginneering*, vol. 6, no. 6, pp. 101-110, 1874.

[16] C. R. Söderberg, “Factor of safety and working stress ,” *Trans ASME*, vol. 52, pp. 13-28, 1939.

[17] F. Dunne, A. Wilkinson, and R. Allen, “Experimental and computational studies of low cycle fatigue crack nucleation in a polycrystal,” *International Journal of Plasticity*, vol. 23, no. 2, pp. 273-295, Feb. 2007.

[18] M. Henderson and J. Martin, “Influence of precipitate morphology on the high temperature fatigue properties of SRR99,” *Acta Metallurgica et Materialia*, vol. 43, no. 11, pp. 4035-4043, Nov. 1995.

[19] M. Henderson, “The influence of crystal orientation on the high temperature fatigue crack growth of a Ni-based single crystal superalloy,” *Acta Materialia*, vol. 44, no. 1, pp. 111-126, Jan. 1996.

[20] M. Shenoy, “Modeling effects of nonmetallic inclusions on LCF in DS nickel-base superalloys,” *International Journal of Fatigue*, vol. 27, no. 2, pp. 113-127, Feb. 2005.

[21] M. Goto and D. M. Knowles, “Initiation and propagation behaviour of microcracks in Ni-base superalloy Udimet 720 Li,” *Engineering Fracture Mechanics*, vol. 60, no. 1, pp. 1-18, May. 1998.

[22] D. L. Davidson, R. G. Tryon, M. Oja, R. Matthews, and K. S. Ravi Chandran, “Fatigue Crack Initiation In WASPALOY at 20 °C,” *Metallurgical and Materials Transactions A*, vol. 38, no. 13, pp. 2214-2225, May. 2007.

[23] H. Pang and P. Reed, “Effects of microstructure on room temperature fatigue crack initiation and short crack propagation in Udimet 720Li Ni-base superalloy,” *International Journal of Fatigue*, vol. 30, no. 10-11, pp. 2009-2020, Oct. 2008.

[24] J. Miao, T. M. Pollock, and J. Wayne Jones, “Crystallographic fatigue crack initiation in nickel-based superalloy René 88DT at elevated temperature,” *Acta Materialia*, vol. 57, no. 20, pp. 5964-5974, Dec. 2009.

[25] G. Khatibi, A. Betzwar-Kotas, V. Groger, and B. Weiss, “A study of the mechanical and faftigue properties of metallic microwires,” *Fatigue and Fracture of Engineering Materials and Structures*, vol. 28, no. 8, pp. 723-733, Aug. 2005.

[26] K. Tanaka and T. Mura, “A theory of fatigue crack initiation at inclusions,” *Metallurgical Transactions A*, vol. 13, no. 1, pp. 117-123, Jan. 1982.

[27] P. S. Karamched and A. J. Wilkinson, “High resolution electron back-scatter diffraction analysis of thermally and mechanically induced strains near carbide

inclusions in a superalloy," *Acta Materialia*, vol. 59, no. 1, pp. 263-272, Jan. 2011.

[28] H. Kimura, Y. Akiniwa, K. Tanaka, Y. Tahara, and T. Ishikawa, "Fatigue Crack Initiation Behavior in Ultrafine-Grained Steel Observed by AFM and EBSP," *JSME International Journal Series A*, vol. 47, no. 3, pp. 331-340, 2004.

[29] Z. Mei, C. R. Krenn, and J. W. Morris, "Initiation and growth of small fatigue cracks in a Ni-base superalloy," *Metallurgical and Materials Transactions A*, vol. 26, no. 8, pp. 2063-2073, Aug. 1995.

[30] N. J. Petch, "The Cleavage Strength of Polycrystals," *Journal of the Iron and Steel Institute*, vol. 174, no. 1, pp. 25-28, 1953.

[31] E. O. Hall, "The Deformation and Ageing of Mild Steel: III Discussion of Results," *Proceedings of the Physical Society. Section B*, vol. 64, no. 9, pp. 747-753, Sep. 1951.

[32] N. A. Fleck, G. M. Muller, M. F. Ashby, and J. W. Hutchinson, "Strain Gradient Plasticity - Theory and Experiment," *Acta Metallurgica Et Materialia*, vol. 42, no. 2, pp. 475-487, 1994.

[33] J. Stölken and A. G. Evans, "A microbend test method for measuring the plasticity length scale," *Acta Materialia*, vol. 46, no. 14, pp. 5109-5115, Sep. 1998.

[34] G. I. Taylor, *Plastic strain in metals*, vol. 62. J. Inst. Metals, 1938.

[35] E. Schmid and W. Boas, *Plasticity of crystals with special reference to metals*. London: F.A. Hughes, 1950, p. xvi, 353 p.

[36] R. Hill, "Generalized Constitutive Relations for Incremental Deformation of Metal Crystals by Multislip," *Journal of the Mechanics and Physics of Solids*, vol. 14, no. 2, pp. 95-&, 1966.

[37] J. Rice, "Inelastic constitutive relations for solids: An internal-variable theory and its application to metal plasticity," *Journal of the Mechanics and Physics of Solids*, vol. 19, no. 6, pp. 433-455, Nov. 1971.

[38] E. H. Lee, "Elastic-Plastic Deformation at Finite Strains," *Journal of Applied Mechanics*, vol. 36, no. 1, pp. 1-&, 1969.

[39] R. Asaro and J. R. Rice, "Strain localization in ductile single crystals," *Journal of the Mechanics and Physics of Solids*, vol. 25, no. 5, pp. 309-338, Oct. 1977.

[40] D. Peirce, R. Asaro, and A. Needleman, "Ane analysis of nonuniform and localized deformation in ductile single crystals," *Acta Metallurgica*, vol. 30, no. 6, pp. 1087-1119, Jun. 1982.

[41] A. H. Cottrell, *Dislocations and plastic flow in crystals*. Oxford: Clarendon Press, 1953, p. ix, 223 p.

[42] N. A. Fleck and J. W. Hutchinson, "Strain gradient plasticity," *Advances in Applied Mechanics*, vol. 33, 1997.

[43] N. Fleck and J. Hutchinson, "A phenomenological theory for strain gradient effects in plasticity," *Journal of the Mechanics and Physics of Solids*, vol. 41, no. 12, pp. 1825-1857, Dec. 1993.

[44] H. Gao, Y. Huang, W. D. Nix, and J. W. Hutchinson, "Mechanism-based strain gradient plasticity - I. Theory," *Journal of the Mechanics and Physics of Solids*, vol. 47, no. 6, pp. 1239-1263, 1999.

[45] W. D. Nix and H. J. Gao, "Indentation size effects in crystalline materials: A law for strain gradient plasticity," *Journal of the Mechanics and Physics of Solids*, vol. 46, no. 3, pp. 411-425, 1998.

[46] B. Backes, Y.Y. Huang, M. Göken, and K. Durst, "The correlation between the internal material length scale and the microstructure in nanoindentation experiments and simulations using the conventional mechanism-based strain gradient plasticity theory ," *Journal of Materials Research*, vol. 24, no. 3, pp. 1197-1207 , 2009.

[47] Y. Huang, H. Gao, and K. C. Hwang, "Strain-gradient plasticity at the micron scale," in *ICM8: Eighth International Conference on the Mechanical Behaviour of Materials*, 1999, pp. 1051-1056.

[48] M. F. Ashby, "The deformation of plastically non-homogeneous materials," *Philosophical Magazine*, vol. 21, no. 170, pp. 399-424, Feb. 1970.

[49] H. Gao, "Geometrically necessary dislocation and size-dependent plasticity," *Scripta Materialia*, vol. 48, no. 2, pp. 113-118, Jan. 2003.

[50] E. Kroner, *Continuum Theory of Dislocations and Self Stresses*. Berlin: Springer, 1958.

[51] H. Liang, "Crystal plasticity modelling of lengthscale effects in deformation and nanoindentation," University of Oxford, 2008.

[52] S. Sun, B. L. Adams, C. Shet, S. Saigal, and W. King, "Mesoscale investigation of the deformation field of an aluminum bicrystal," *Scripta Materialia*, vol. 39, no. 4-5, pp. 501-508, 1998.

[53] S. Sun, B. L. Adams, and W. E. King, "Observations of lattice curvature near the interface of a deformed aluminium bicrystal," *Philosophical Magazine A-Physics of Condensed Matter Structure Defects and Mechanical Properties*, vol. 80, no. 1, pp. 9-25, 2000.

[54] T. B. Britton, H. Liang, F. P. E. Dunne, and A. J. Wilkinson, “The effect of crystal orientation on the indentation response of commercially pure titanium: experiments and simulations,” *Proceedings of the Royal Society A: Mathematical, Physical and Engineering Sciences*, vol. 466, no. 2115, pp. 695-719, Nov. 2009.

[55] A. J. Schwartz, *Electron backscatter diffraction in materials science*, 2nd ed. New York: Springer, 2009, p. xxii, 403 p.

[56] O. Engler and V. Randle, *Introduction to texture analysis□: macrotexture, microtexture, and orientation mapping*, 2nd ed. London: CRC□;Taylor & Francis, 2010, p. xiv, 456 p.

[57] M. N. Alam, M. Blackman, and D. W. Pashley, “High-Angle Kikuchi Patterns,” *Proceedings of the Royal Society of London Series A-Mathematical and Physical Sciences*, vol. 221, no. 1145, pp. 224-242, 1954.

[58] G. I. Finch and H. Wilman, *Ergebnisse der exakten naturwissenschaften*, vol. 16, no. 16. Berlin, Heidelberg: Springer Berlin Heidelberg, 1937, p. p. [353]-436.

[59] X. Tao and A. Eades, “Monte Carlo Simulation for Electron Backscattering Diffraction,” *Microscopy and Microanalysis*, vol. 10, no. 2, pp. 940-941, 2004.

[60] S. I. Wright and B. L. Adams, “Automatic-Analysis of Electron Backscatter Diffraction Patterns,” *Metallurgical Transactions A-Physical Metallurgy and Materials Science*, vol. 23, no. 3, pp. 759-767, 1992.

[61] “Orientation Imaging Microscopy User Manual 5.3,” TSL-EDAX, 2007.

[62] B. L. Adams, S. I. Wright, and K. Kunze, “Orientation imaging: The emergence of a new microscopy,” *Metallurgical Transactions A*, vol. 24, no. 4, pp. 819-831, Apr. 1993.

[63] D. P. Field, “Improving the Spatial Resolution of EBSD,” *Microscopy and Microanalysis*, vol. 11, 2005.

[64] A. Drake and S. H. Vale, “Development of an electron backscatter diffraction and microtexture measurement system.,” *Electron Microscopy and Analysis*, vol. 147, pp. 137-140, 1995.

[65] A. J. Wilkinson, “Measurement of elastic strains and small lattice rotations using electron back scatter diffraction,” *Ultramicroscopy*, vol. 62, no. 4, pp. 237-247, 1996.

[66] F. J. Humphreys and I. Brough, “High resolution electron backscatter diffraction with a field emission gun scanning electron microscope,” *Journal of Microscopy-Oxford*, vol. 195, pp. 6-9, 1999.

[67] A. J. Wilkinson, “High resolution measurements of strain and tilt distributions in SiGe mesas using electron backscatter diffraction,” *Applied Physics Letters*, vol. 89, no. 24, p. 241910, Dec. 2006.

[68] J. Q. Da Fonseca, P. M. Mummery, and P. J. Withers, “Full-field strain mapping by optical correlation of micrographs acquired during deformation,” *Journal of Microscopy-Oxford*, vol. 218, pp. 9-21, 2005.

[69] K. Z. Troost, P. Vandersluis, and D. J. Gravesteijn, “Microscale Elastic-Strain Determination by Backscatter Kikuchi Diffraction in the Scanning Electron-Microscope,” *Applied Physics Letters*, vol. 62, no. 10, pp. 1110-1112, 1993.

[70] W. Pantleon, W. He, T. P. Johansson, and C. Gundlach, “Orientation inhomogeneities within individual grains in cold-rolled aluminium resolved by electron backscatter diffraction,” *Materials Science and Engineering a-Structural Materials Properties Microstructure and Processing*, vol. 483, pp. 668-671, 2008.

[71] W. Pantleon, “Resolving the geometrically necessary dislocation content by conventional electron backscattering diffraction,” *Scripta Materialia*, vol. 58, no. 11, pp. 994-997, 2008.

[72] K. Pantleon, A. Gholinia, and M. A. J. Somers, “Quantitative microstructure characterization of self-annealed copper films with electron backscatter diffraction,” *Physica Status Solidi A-Applications and Materials Science*, vol. 205, no. 2, pp. 275-281, 2008.

[73] S. B. T. Ben Britton Michael Preuss and Angus J. Wilkinson, “Electron backscatter diffraction study of dislocation content of a macrozone in hot-rolled Ti–6Al–4V alloy,” *Scripta Materialia*, vol. 62, no. 9, pp. 639-642.

[74] A. J. Wilkinson, G. Meaden, and D. J. Dingley, “Mapping strains at the nanoscale using electron back scatter diffraction,” *Superlattices and Microstructures*, vol. 45, no. 4-5, pp. 285-294, 2009.

[75] S. Villert Maurice, C., Wyon, C., Fortunier, R., “Accuracy assessment of elastic strain measurement by EBSD,” *Journal of Microscopy*, vol. 233, no. 2, pp. 290-301, 2009.

[76] Y. B. G. M.D. Vaudin S.J. Stranick and R.F. Cook, “Nanoscale Measurements of Strain and Stress using Electron Back Scattered Diffraction and Confocal Raman Microscopy,” *Appl Phys Lett*, vol. 93, p. 3, 2008.

[77] A. J. Wilkinson Randman, D, “Determination of elastic strain fields and geometrically necessary dislocation distributions near nanoindents using electron back scatter diffraction,” *Philosophical Magazine*, vol. 90, no. 9, pp. 1159-1177, 2010.

[78] D. J. Stephenson, J. R. Nicholls, and P. Hancock, "Particle Surface Interactions during the Erosion of a Gas-Turbine Material (MarM002) by Pyrolytic Carbon Particles," *Wear*, vol. 111, no. 1, pp. 15-29, 1986.

[79] M. J. Starink, H. Cama, and R. C. Thomson, "MC carbides in the Hf containing Ni based superalloy MarM002," *Scripta Materialia*, vol. 38, no. 1, pp. 73-80, 1997.

[80] R. Sellamuthu and A. F. Giamei, "Measurement of Segregation and Distribution Coefficients in Mar-M200 and Hafnium-Modified Mar-M200 Superalloys," *Metallurgical Transactions A-Physical Metallurgy and Materials Science*, vol. 17, no. 3, pp. 419-428, 1986.

[81] P. Spilling and J. W. Martin, "Precipitation of HfC in MM-002," *Metallography*, vol. 15, no. 1, pp. 63-71, Feb. 1982.

[82] P. Viatour, D. Coutsouradis, and L. Habraken, "Casting conditions, microstructure and creep properties of Mar-M-002 blades," in *High Temperature Alloys for Gas Turbines*, 1978, pp. 875-891.

[83] H. M. Tawancy, N. M. Abbas, A. I. Al-Mana, and T. N. Rhys-Jones, "Thermal stability of advanced Ni-base superalloys," *Journal of Materials Science*, vol. 29, no. 9, pp. 2445-2458, Jan. 1994.

[84] M. F. Henry, Y. S. Yoo, D. Y. Yoon, and J. Choi, "The dendritic growth of γ' precipitates and grain," *Metallurgical Transactions A*, vol. 24, no. 8, pp. 1733-1743, Aug. 1993.

[85] A. Koul and F. Pickering, "Grain coarsening in Fe□ Ni□ Cr alloys and the influence of second phase particles," *Acta Metallurgica*, vol. 30, no. 7, pp. 1303-1308, Jul. 1982.

[86] J. M. Larson and S. Floreen, "Metallurgical factors affecting the crack growth resistance of a superalloy," *Metallurgical Transactions A*, vol. 8, no. 1, pp. 51-55, Jan. 1977.

[87] X. Yao, "The microstructural characteristics in a newly developed nickel-base cast superalloy," *Materials Characterization*, vol. 38, no. 2, pp. 97-102, Feb. 1997.

[88] M. J. Donachie and S. J. Donachie, *Superalloys: a technical guide*. ASM International, 2002, p. 439.

[89] BLG Productions, "CrossCourt 3." BLG Productions, Bristol, UK, 2010.

[90] H.-R. Wenk, *Preferred orientation in deformed metals and rocks□: an introduction to modern texture analysis*. Orlando: Academic Press, 1985.

[91] H. Kuhn and H. Sockel, “Elastic properties of textured and directionally solidified nickel-based superalloys between 25 and 1200°C,” *Materials Science and Engineering: A*, vol. 112, pp. 117-126, Jun. 1989.

[92] B. S. El-Dasher, B. L. Adams, and A. D. Rollett, “Viewpoint: experimental recovery of geometrically necessary dislocation density in polycrystals,” *Scripta Materialia*, vol. 48, no. 2, pp. 141-145, 2003.

[93] D. P. Field, P. B. Trivedi, S. I. Wright, and M. Kumar, “Analysis of local orientation gradients in deformed single crystals,” *Ultramicroscopy*, vol. 103, no. 1, pp. 33-39, 2005.

[94] E. Demir, D. Raabe, N. Zaafarani, and S. Zaefferer, “Investigation of the indentation size effect through the measurement of the geometrically necessary dislocations beneath small indents of different depths using EBSD tomography,” *Acta Materialia*, vol. 57, no. 2, pp. 559-569, 2009.

[95] G. Miyamoto, A. Shibata, T. Maki, and T. Furuhara, “Precise measurement of strain accommodation in austenite matrix surrounding martensite in ferrous alloys by electron backscatter diffraction analysis,” *Acta Materialia*, vol. 57, no. 4, pp. 1120-1131, 2009.

[96] F. J. Humphreys, *Review Grain and subgrain characterisation by electron backscatter diffraction*, vol. 36, no. 16. Springer Netherlands, 2001, pp. 3833-3854-3854.

[97] A. J. Wilkinson, “A new method for determining small misorientations from electron back scatter diffraction patterns,” *Scripta Materialia*, vol. 44, no. 10, pp. 2379-2385, 2001.

[98] A. Arsenlis and D. M. Parks, “Crystallographic aspects of geometrically-necessary and statistically-stored dislocation density,” *Acta Materialia*, vol. 47, no. 5, pp. 1597-1611, 1999.

[99] D. S. SIMULIA, “ABAQUS.” SIMULIA, Dassault Systèmes, Vélizy-Villacoublay, France.

[100] T. B. Britton et al., “Factors affecting the accuracy of high resolution electron backscatter diffraction when using simulated patterns.,” *Ultramicroscopy*, vol. 110, no. 12, pp. 1443-53, Nov. 2010.